AUGUST 1991

ECN-R--91-006

STRESS MEASUREMENTS BY MEANS OF NEUTRON DIFFRACTION

P.C. BRAND

The Netherlands Energy Research Foundation ECN is the leading institute in the Netherlands for energy research. ECN carries out pure and applied research in the fields of nuclear energy, fossil fuels, renewable energy sources, environmental aspects of energy supply, informatics and the development and application of new materials. Energy studies are also a part of the research programme.

ECN employs more than 900 staff. Contracts are obtained from the government and from national and foreign organizations and industries.

ECN's research results are published in a number of report series, each series serving a different public from contractors to the international scientific world.

The R-series is for research reports that make the results of (pure) ECN research available to the international technical and scientific world.

Netherlands Energy Research Foundation ECN
Service Unit General Services
P.O. Box 1
NL-1755 ZG Petten
The Netherlands
Telephone: +31 2246 43 23
Fax : +31 2246 34 83

This report is available on remittance of Dfl. 20 to:
ECN, SU General Services, Petten,
The Netherlands.
Giro account (postal account) No. 3977703.
Please quote the report number.

The contents of this report was presented as a PhD-thesis at the University of Twente. The work described was carried out in co-operation with the Foundation for Advanced Metals Science (SGM) at Enschede.

Contents

List of Symbols

α:	divergence of a neutron beam
α_1:	divergence of the primary neutron beam
α_2:	divergence of the diffracted neutron beam
Γ:	instrumental resolution width
Δ:	independent variable during convolution
$\Delta 2\theta$:	standard deviation of a diffraction peak position determination; shift of a diffraction peak position
$\Delta\boldsymbol{\varepsilon}$:	error in the strain solution vector
$\Delta\boldsymbol{\sigma}$:	error in the stress solution vector
Δd:	error in the lattice spacing
Δl:	misplacement in the beam direction of the double knife edge
δ_{ij}:	Kronecker symbol, $\delta_{ij} = 1$ for $i = j$; $\delta_{ij} = 0$ for $i \neq j$
ε_ψ:	strain in the direction of ψ
ε_i, $\boldsymbol{\varepsilon}$:	strain tensor in Voigt notation
ε_i^D:	principal strain tensor
ε_{ij}:	strain tensor
$\boldsymbol{\varepsilon}_0$:	strain constraints vector
θ_m:	diffraction angle for the monochromator
2θ:	diffraction peak position (double Bragg angle)
$2\theta_\psi$:	double Bragg angle beloging to d_ψ
$2\theta_0$:	double Bragg angle belonging to the stress free lattice parameter d_0
κ:	numerical constant
λ:	wavelength of x-ray or neutron radiation
μ:	effective coefficient of attenuation
ν:	Poisson's ratio
σ:	numerical value of a uniaxial stress
σ_θ:	stress in circumferential direction
σ_{FWHM}:	full width at half maximum of a Gaussian profile

σ_i, $\boldsymbol{\sigma}$: stress tensor in Voigt notation
σ_i^D: principal stress tensor
σ_{ij}: stress tensor
σ_l: longitudinal stress
σ_r: radial stress
σ_t: transverse stress
σ_z: axial stress
$\boldsymbol{\sigma}_0$: stress constraints matrix
σ_0: stress at the surface of a bar ($x = 0$)
2φ: diffractometer counter angle
$2\varphi_0$: direct beam counter position
$2\varphi_{min}$: lowest value of the counter position where intensity is obtained due to the umbrella effect
φ, χ: orientations of a texture sample
χ^2: reduced residue of a least squares result
ψ: angle between the specimen surface normal and the diffraction vector $\boldsymbol{q}$
ω: sample rotation axis
ω_0: relative direction of the beam centre line
$\boldsymbol{A}$: strain constraints matrix
$\boldsymbol{A}^T$: transposed matrix $\boldsymbol{A}$
a_{ij}: elements of matrix $\boldsymbol{A}$
$\boldsymbol{B}$: stress constraints matrix
B: breadth of a bar
$\boldsymbol{C}$: stiffness tensor in matrix notation
c_{ij}: cosine matrix; elements of matrix $\boldsymbol{C}$
C_{ij}: stiffness tensor in Voigt notation
C_{ijkl}: stiffness tensor
d: geometrical distance
d, d_{hkl}: lattice spacing
$\boldsymbol{d}$: vector of measured d-values
D: beam path length through a material; thickness of a bar
$D(2\varphi,2\theta)$: function describing a diffraction profile
$d(k_i l_i m_i)$: lattice spacing in the direction $(k_i l_i m_i)$
$\langle d(k_i l_i m_i)\rangle$: average lattice spacing
d_ψ: lattice spacing in the direction of ψ
d_0: strain free lattice parameter
E: Young's modulus
$\boldsymbol{e}$: strain solution vector
$e(k_i l_i m_i)$: strain in the direction of $(k_i l_i m_i)$
g_{ii}: elements of a weight matrix
$\boldsymbol{G}$: weight matrix
h: co-ordinate in the sample volume
H: half height of a neutron beam
hkl: Laue indices, Miller indices
I: measured intensity
I_0: intensity count at the top of a Gaussian profile; constant of proportionality in functions describing intensities
I_b: background intensity
I_d: diffracted beam weight function
I_p: primary beam weight function
$(k_i l_i m_i)$: direction cosines in the specimen axis system
$\boldsymbol{K}$: orientations matrix
l: distance between the knives of the double knife edge
l_1: distance from the diffractometer axis and the primary beam aperture
l_2: distance from the diffractometer axis and the diffracted beam aperture
L: distance between the diffractometer axis and the vertical beam limit in the counter aperture
n: integer number
O: origin of co-ordinate system
p: primary beam aperture position
p_0: length of half the rhombus diagonal parallel to $\boldsymbol{q}$
p_{90}: length of half the rhombus diagonal perpendicular to $\boldsymbol{q}$
p_{ij}, p: hydrostatic pressure
$\boldsymbol{q}$: diffraction vector
r: radius
r^2: quantity to be minimized during a least squares process
R: radius of curvature of the monochromator
$R(\Delta,2\theta)$: instrumental resolution function
s: diffracted beam aperture position
s_1: distance from the reactor vessel to the monochromator

s_2: distance from the monochromator to the diffractometer centre
S: compliance tensor in matrix notation
S: half height of a sample
S_1, $S_2/2$: diffraction elastic constants
S_{ij}: compliance tensor in Voigt notation
S_{ijkl}: compliance tensor
V: covariance matrix
w: horizontal opening of aperture
w_1: horizontal opening of the primary beam aperture
w_2: horizontal opening of the diffracted beam aperture
$W(2\varphi,2\theta)$: weight function
x: translation co-ordinate in a specimen
x_0: relative position of the beam centre line; relative position of the sample volume at $\psi = 0°$
x_{90}: relative position of the sample volume at $\psi = 90°$
X: lever length during bending
y: translation co-ordinate in a specimen
$y(2\varphi)$: convolution product
y_p: centre of gravity of the sample volume
z: translation co-ordinate in a specimen

1
General Introduction

1.1 MATERIALS SCIENCE, STRESSES AND NEUTRONS

The history of materials science is characterized by a constant search for better materials and by an improving understanding of why a specific material should be used in a specific application.

Scientists of various background study the enormous variety of materials available nowadays. For example, an engineer studies materials on the basis of their behaviour in constructions or during manufacturing. He ranks materials, according to properties such as strength, formability and corrosion resistance, without necessarily wondering why a material possesses those properties. Contrarily, the solid state physicist, who operates at the other side of the materials science spectrum, would see a material as a specific mixture of chemical elements which was put into some physical shape. As such he studies the properties of the mixture without wondering what they mean for potential products or production processes.

The materials scientist, moving back and forth between engineering and solid state physics, links characteristic features such as composition and structure to the demands of engineers.

In order to describe a material from the materials scientist point of view, besides composition and structure, a third characteristic feature of materials should be taken into account: the residual stress state. Just like composition and structure, the residual stress state influences the behaviour of a material. An example is stress corrosion behaviour, which depends strongly on both the sign and the magnitude of the surface stress state of a material. Other examples involve the dimensional stability of

a piece of work that possesses a region under tension that is removed during machining and the dimensional stability during and after welding.

For the determination of the characteristic features, the materials scientist uses specific tools. For structure determination various types of microscopes are available, while chemical analysis can be performed in a variety of ways, ranging from wet chemical analysis to advanced instrumental analysis (*e.g.* energy dispersive analysis of x-rays emitted by the sample in the vacuum chamber of an electron microscope).

The third characteristic feature – the residual stress state – can be determined in various ways, either destructive or non-destructive. Non-destructive analysis can be performed by measuring one of the direct results of stress: the reversible rearrangement of atoms in the material according to the laws of elasticity, which we normally call strain. A strain present in a material changes a number of physical properties of the material. As an example we mention the change of the velocity for the propagation of ultrasound, which is a second order effect that can be quantified by measurement.

The most direct assessment of the altered distances between atoms is the determination of the crystallographic lattice spacing. A convenient method is by diffraction of either electromagnetic- or particle waves. The characteristic wavelength of these waves should be of the same order of magnitude as the lattice spacing to be measured.

The conventional way for the determination of lattice parameters is x-ray diffraction. In this method, a monochromatic x-ray beam is used in a diffractometer experiment and by measuring the diffraction angle, a value for the lattice spacing is found. The penetration depth for x-rays in metals is in the order of 5 to 100 μm, so non-destructive x-ray lattice spacing measurements are limited to the surface of materials.

In order to perform measurements in the bulk of materials, neutron diffraction can be used. Contrary to x-rays, neutrons penetrate several millimetres to several centimetres into most solid materials. Typically, the flight path length at which the 50% level of the primary neutron beam intensity has been reached ranges from 5 to 70 mm. Because the wavelength of neutrons can be chosen to be more or less equal to that of x-rays, the same diffraction laws apply and as such neutrons can be used to determine lattice spacings in the bulk of materials. When the strain free lattice parameter is known, the strain can be calculated from the measured lattice distance. When an appropriate set of strain measurements is performed – each belonging to a different orientation of the specimen – the three dimensional stress state is calculated according to the laws of elasticity.

The advantage of neutrons over x-rays is thus made clear. Unfortunately the technique has a number of disadvantages.

1. In order to perform neutron stress measurements, one needs a neutron source in the form of a nuclear reactor or a spallation source. Both source types are scarce and both are non-transportable. So in order to perform this type of measurements one has to bring specimens to the source instead of bringing the source to the specimen, which is nowadays readily done with x-ray equipment. This imposes strong limits on the size of the items to be investigated.
2. The relatively low brightness of neutron sources compared to x-ray sources, poses limits to the maximum achievable spatial resolution of the technique that can be achieved in a reasonable measurement time.

Despite these complications, numerous existing materials science problems can potentially be solved. In this thesis the experimental difficulties related to the technique as well as a few examples of application will be presented.

1.2 HISTORICAL PERSPECTIVE

Stress measurements using x-ray diffraction techniques have been reported from 1925 onward [1.1]. The theoretical understanding of the measurement method has been completed in 1936 [1.2]. The first attempts have been made using film techniques. With the development of better detection hardware, the diffractometer became the most abundantly used instrument for the determination of stresses in crystalline materials [1.3].

Also in 1936, the phenomenon of neutron diffraction was discovered [1.4][1.5]. It was not until 1981, however, that the first publications appeared, mentioning neutron diffraction as a tool for stress determination [1.6][1.7][1.8][1.9].

The first attempts to determine stresses by means of neutron diffraction were mainly focused on the proof of the principle, just like neutron diffraction itself in the old days. A variety of validation experiments have been reported by Pintschovius *et.al.* [1.6] and Krawitz *et.al.* [1.7]. Al these experiments have been performed using specimens containing a predetermined stress state. The specimens range from an elastically bent bar to a thermally shrunk fitted joint.

Most experimentalists use cadmium masks between the source and the specimen as well as between the specimen and the neutron detector. The minimum sample size obtained in this way is reported by Pintschovius who performed measurements employing a sample size of no more than 10 mm^3.

When studying the early literature on neutron diffraction stress measurements, one thing becomes very clear: in order to do these experiments one should have a high flux reactor and still a lot of patience. To give an indication: the time consumption for the registration of a diffraction peak using x-ray diffraction is in the order of several minutes, while for neutron diffraction 5 to 24 hours for one diffraction peak is no exception. Knowing that for the determination of one stress value in a one dimensional stress field one needs at least 3 diffraction peaks, one can conclude that neutron diffraction will never become a service operation. It will be limited to fundamental work and to pilot experiments on high capital products. The argument why it makes sense to do these measurements at all is, however, very simple: there is no other way to achieve stress information about the bulk of materials non-destructively.

The experiments described by the pioneers in this field all lead to the same conclusion: it is possible to measure stresses by means of neutron diffraction. In a second round of publications the same authors start to give their experiences on real life specimens possessing simple residual stress patterns which are predicted by means of finite element calculations or simply qualitative analysis. A few examples from that period are

1. Quenched cylinders [1.10].
2. Autofrettaged steel tubes [1.11][1.12].
3. Steel sheet [1.13].
4. Stress due to fatigue in a test specimen [1.14].

5. Stress in materials consisting of more than one phase [1.15][1.16] [1.17][1.18].
6. Welding stresses [1.19][1.20][1.21].
7. Stress measurements in uranium which is a difficult material for x-ray stress measurements [1.22].

An important publication in this period is the one from Allen *et.al.* [1.14] which gives a very good theoretical background for the determination of the stress tensor from measured strain data. It was this article that stood as a model for the chapter on stress determination that is given later in this thesis as well as for the development of a data reduction computer program which is closely related to that chapter.

The x-ray spectrum generated in a tube is a superposition of very intense monochromatic lines which are characteristic for the tube's anode material, on a continuous spectrum that depends on the tube voltage. For single line diffraction measurements like stress measurements, usually one of the characteristic wavelengths is chosen. Contrary to x-rays, the wavelength spectrum of a neutron beam is merely a continuous one with no particular peaks, so in a neutron beam – before monochromatization – all wavelengths are present. This phenomenon is used by Pintschovius in a variable wavelength set-up were the lattice distance is not determined in a scan of the scattering angle but during a scan of the wavelength. The advantage is clear: the scattering geometry does not change during the registration of the lattice distance and geometry dependent phenomena such as attenuation, no longer affect the data reduction. A second advantage is that the scattering angle can always be set to 90°, the ideal angle in terms of spatial resolution.

Most experimentalists use some sort of scanning technique (wavelength or scattering angle). The group of Krawitz *et.al.*, besides scanning techniques, have shown a different approach: use of a position sensitive detector [1.23]. This type of detector is advantageous, because a complete diffraction peak is 'seen' at the same time. As such, a more economic use is made of the available neutrons. However, the drawback is that the positioning of a sampling volume in the specimen becomes cumbersome, as the regions in the position sensitive detector corresponding to a specific scattering angle are no longer direction sensitive and the neutrons arriving there could be coming from anywhere in the

specimen. The solution for this, as applied by Krawitz *et.al.* is a radial Soller slit placed in front of the detector.

Besides the basic thoughts about how to build a measurement set-up and how to subsequently perform measurements with it, the authors of the cited papers all pay some attention to the problem of alignment. As neutron diffractometers are usually not built for very small samples, the alignment of such a sample in the scattering geometry is usually not very critical. For stress measurements, however, the alignment is very critical as the sampling volume in the specimen is very small indeed. During a change of the orientation of a specimen, in order to measure the lattice spacing in another direction in the sample, the experimentalist must be very sure that the sample volume he is studying is located at the same position as before. Also the exact location of the sample volume with respect to the specimen geometry must be well known in order to allocate the stress value to be found eventually, to a specific specimen co-ordinate.

A more fundamental experimental problem is the determination of the stress free lattice parameter d_0, which is needed for the calculation of the stress state whenever that is more complicated than bi-axial. For this purpose several options are available, however, none of them is generally applicable. One of the options is the measurement of d_0 using a stress free specimen of the same composition as the real specimen. Another is the application of the force balance law that states that the stress integrated over a section through a piece of material should be zero. Which solution should be applied in which case has been one of the major topics that have been discussed recently in a NATO workshop, march 1991 [1.24].

After having gone through the available literature it can be concluded that stress measurements by means of neutron diffraction ask for a creative solution depending on the problem to be solved, as well as on the equipment and the time available.

1.3 IMPLEMENTATION IN PETTEN

The work described in this thesis has been performed at the High Flux Reactor situated at Petten, The Netherlands. The reactor is the property of the Joint Research Centre of the European Communities. Its main

purpose is to serve as a tool for investigating the behaviour of materials that have been exposed to in-core neutron irradiation. The thermal neutron flux that is present in the cooling water of the reactor can be extracted in the form of neutron beams. These beams are used in various beam experiments by the Netherlands Energy Research Foundation (ECN).

The idea for the measurement of residual stresses at the Petten establishment stems from 1986. It is a logical extension of the work going on at the laboratories of the Foundation for Advanced Metals Science at Enschede (SGM) in the field of residual stress measurements by means of x-ray diffraction on the one hand and the objective of the Solid State Physics group of ECN to aim their neutron beam research knowledge more towards applied work on the other hand. The first step was to check whether the available intensity is sufficient for stress measurements. When this has been confirmed, a PhD project was started of which this work is the result. The first objective of the project was to develop a preliminary set-up. After a successful development this set-up was planned to be used for the solution of a number of specific materials science problems. The first steps undertaken within the framework of the PhD project were

1. Building the set-up.
2. Solving the alignment problems.
3. Development of data reduction processes.

In the first part of this thesis, these aspects will be presented.

The development stage, took much more time than anticipated. Therefore the application of the technique had to be restricted, as far as the PhD project is concerned. The measurements that have been performed, can be classified in two categories

1. A 'proof of the principle' experiment in order to show that the instrument really works. We have chosen for the determination of diffraction elastic constants using an iron bar subjected to pure bending.
2. Measurements on a few 'engineering cases' in which residual stresses play a role. A selection was made out of the numerous experiments possible. Measurements were to be performed on

quenched iron and steel cylinders and on a bar of cold rolled steel.

All neutron measurement results have been compared with the results of x-ray measurements and with theoretical calculations based on finite element- and other calculations. In the second part of this thesis the results of this work are presented.

REFERENCES

1.1 H.H. Lester and R.H. Aborn, *Army Ordnance*, **6**, pp 120,200,283 and 364, (1925-1926).

1.2 F. Gisen; R. Glocker; and E. Osswald, *Z. Tech. Physik*, **17**, 145 (1936).

1.3 M.E. Hilley; J.A. Larson; C.F. Jatczak; and R.E. Ricklefs, editors, *Residual Stress Measurements by X-ray Diffraction*, SAE Information Report J 784a (1971).

1.4 H. Halban and P. Preiswerk, *C. r. hebd. Séanc. Acad. Sci. Paris.*, **203**, 73 (1936).

1.5 D.P. Mitchell and P.N. Powers, *Phys. Rev.*, **50**. 486 (1936).

1.6 L. Pintschovius; V. Jung; E. Macherauch; R. Schäfer and O. Vöhringer, *Proceeding of the 28th Sagamore Army Materials Research Conference*, Lake Placid, N.Y., July 13-17, 467 (1981).

1.7 A.D. Krawitz; J.E. Brune and M.J. Schmank, *Proceeding of the 28th Sagamore Army Materials Research Conference*, Lake Placid, N.Y., July 13-17, 139 (1981).

1.8 A.J. Allen; M.T. Hutchings; C.G. Windsor and C Andreani, *NDT Int.*, **14**, 249 (1981).

1.9 A.D. Krawitz and M.J. Schmank, *Metall. Trans. A*, **13A**, 1069 (1982).

1.10 L. Pintschovius; B. Scholtes and R. Schröder, *Proceedings of the 5th Risø International Symposium on Metallurgy and Materials Science*, Risø Natl. Lab., Roskilde, Denmark, 419 (1984).

1.11 L. Pintschovius; E. Macherauch and B. Scholtes, *Mater. Sci. Eng.*, **84**, 163 (1986).

1.12 A. Stacey and G.A. Webster., *Int. J. Pressure Vessels Piping*, **31**, 205 (1988).

1.13 P. Lambrineas; T.R. Finlayson; J.R. Griffiths; C.J Howard and T.F Smith, *NDT int.*, **20**, 285 (1987).

1.14 A.J. Allen; M.T. Hutchings and C.G. Windsor, *Adv. Phys.*, **34**, 445 (1985).

1.15 A.D. Krawitz; R. Roberts and J. Faber, *Adv. X-Ray Anal.*, **27**, 239 (1984).

1.16 C.M. Sayers, *Mater. Sci. Eng.*, **91**, 195 (1987).

1.17 A.J. Allen; M. Bourke; M.T. Hutchings; A.D. Krawitz and C.G. Windsor, *Residual Stresses in Science and Technology*, Vol.1, Garmisch-Patenkirchen, 151 (1987)

1.18 A.D. Krawitz; R. Roberts and J. Faber, *Adv. X-Ray Anal.*, **27**, 239 (1984).

1.19 A.J. Allen; C. Andreani; M.T. Hutchings; C.M. Sayers and C.G. Windsor, *Proceedings of the 5th Risø International Symposium on Metallurgy and Materials Science*, Risø Natl. Lab., Roskilde, Denmark, 169 (1984).

1.20 A.J. Allen; M.T. Hutchings and C.G. Windsor, *The effects of fabrication related stresses on product manufacture and performance*, Cambridge, Welding Institute, 183 (1987).

1.21 A.J. Allen; M.T. Hutchings and V.S. Rainey, *Proceedings on the 4th European conference on Non-destructive testing*, Oxford, 1808 (1988)

1.22 H.J. Prask and C.S. Choi, *J. Nucl. Mater.*, **126**, 124, (1984).

1.23 A.D. Krawitz; P.J. Rudnik; B.D. Butler and J.B. Cohen, Northwestern University, Department of Materials Science, Evanston, Ill., Technical Report No. 20, ADA158 882, August 1985.

1.24 *Proceedings of the NATO Advanced Research Workshop on the Measurement of Residual and Applied Stress using Neutron Diffraction*, Oxford 18th-22nd march 1991, edited by M.T. Hutchings and A.D. Krawitz, to be published in the NATO-ASI-E series by Kluwer Holland.

2
Applied Diffraction Theory

2.1 INTRODUCTION

The principle of stress measurements by means of diffraction techniques is a very clear one. Neutron or x-ray diffraction is used as a means to determine the lattice spacing of a specific stack of crystallographic planes, as a function of the orientation of such planes in the specimen axis system. From an experimental point of view, the measurement of a stress state in a specimen reduces to the quantitative determination of the angular position of a number of diffraction peaks. These positions are translated into lattice distances. Subsequent mathematical analysis of the lattice distances as a function of their orientations will eventually lead to the determination of the stress state.

In this chapter we will limit ourselves to the first step of the process described above: the determination of the position of a diffraction peak. In this stage two sources of error can appear

1. A statistical error which is related to the shape of the diffraction peak and to the way the diffraction experiment is arranged in terms of counting time, step size *etc*. In section 2.2 it will be shown that its magnitude can be estimated from a peak fit procedure, when both shape and intensity of the peak are known.
2. A systematic error that does not change when a diffraction peak measurement is repeated in exactly the same circumstances. This systematic error is a function of the specimen orientation in the diffractometer geometry as well as of the sample geometry itself. A stress measurement consists of a number of such peak

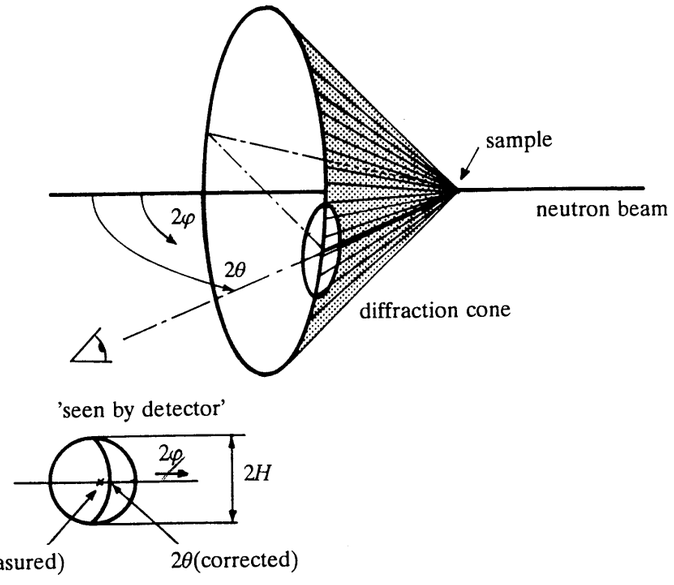

Fig. 2.1 Illustration of the 'umbrella effect'. Because a finite part of the cone is sensed by the detector, an apparent shift to the hollow side of the cone is caused.

position determinations. For each peak the geometrical circumstances are different and as a consequence, the systematic error will be different for each of them.

At this point it is interesting to note that a systematic error that is equal for all diffraction peaks that enter a stress determination problem, does not harm the determination of the stress state at all. This follows from the fact that for stress measurements relative peak shifts are important and absolute peak position determinations are not necessary.

In order to eliminate the geometry dependent part of the systematic error (*i.e.* the part that is not equal for all peaks), the influence of the geometry on the position and shape of the diffraction peak should be established. The two main sources of geometry dependent systematic error are

1. The neutron detector 'sees' a finite height of the diffraction cone. When this cone has an apex unequal to 180° *i.e.* when the

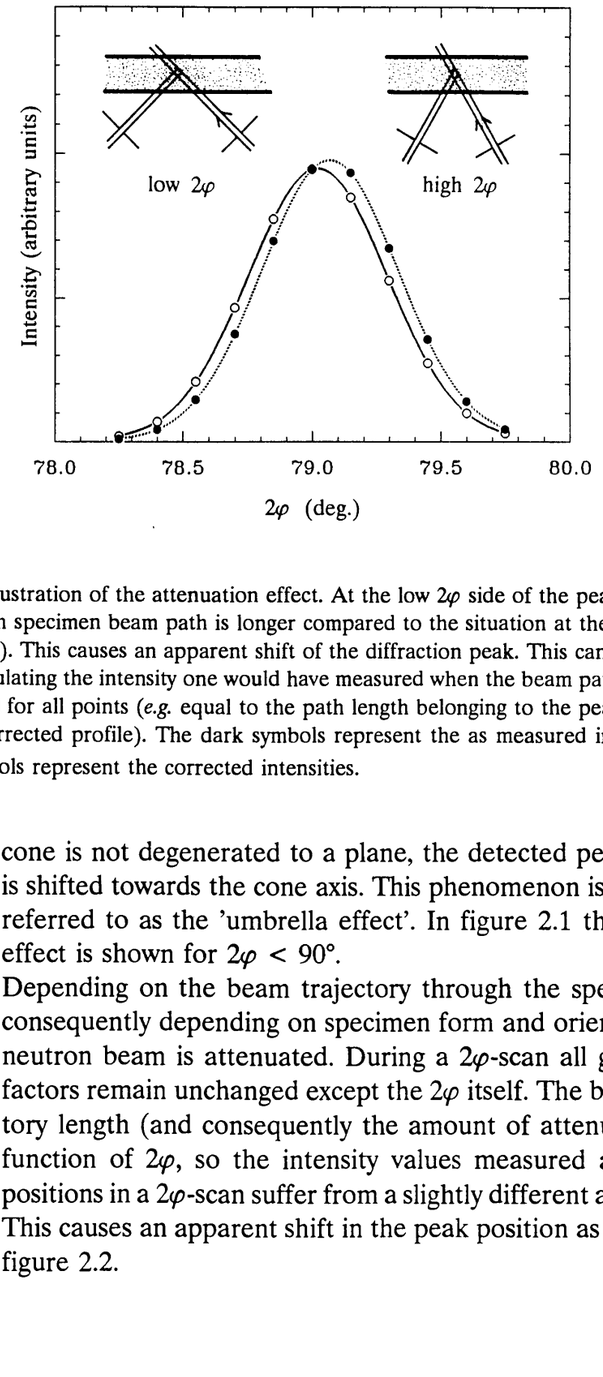

Fig. 2.2 Illustration of the attenuation effect. At the low 2φ side of the peak (left inset), the through specimen beam path is longer compared to the situation at the high 2φ side (right inset). This causes an apparent shift of the diffraction peak. This can be corrected for by calculating the intensity one would have measured when the beam path would have been equal for all points (*e.g.* equal to the path length belonging to the peak position of the not corrected profile). The dark symbols represent the as measured intensities, the open symbols represent the corrected intensities.

cone is not degenerated to a plane, the detected peak position is shifted towards the cone axis. This phenomenon is commonly referred to as the 'umbrella effect'. In figure 2.1 the umbrella effect is shown for $2\varphi < 90°$.

2. Depending on the beam trajectory through the specimen and consequently depending on specimen form and orientation, the neutron beam is attenuated. During a 2φ-scan all geometrical factors remain unchanged except the 2φ itself. The beam trajectory length (and consequently the amount of attenuation) is a function of 2φ, so the intensity values measured at different positions in a 2φ-scan suffer from a slightly different attenuation. This causes an apparent shift in the peak position as is shown in figure 2.2.

In sections 2.3 and 2.4 of this chapter these two sources of systematic error as well as the ways to account for them will be discussed.

2.2 THE STATISTICAL ERROR IN THE PEAK POSITION

In this section, the influence of the diffraction peak shape and the measurement procedure on the peak position will be analyzed. The main interest is not the peak position itself, but the estimated statistical error in the calculated peak position.

A diffraction peak obtained in a neutron diffraction experiment consists of a number of intensity values, each value corresponding to a distinct counter (2φ) position,. The peak is thus defined as a set of positions (2φ) and a corresponding set of intensities. Characteristics of the first set are the number of counter positions and the interval length between two adjacent positions. Both are chosen by the experimentalist. The second set is characterized by the peak position, the peak height and the shape of the profile. These characteristics will only be known after the measurement as only nature knows them. Nevertheless, the experimentalist has some influence on the peak height, because he is free to choose the counting time per scan point.

The aim of the present study is to establish the influence of the measurement method and the peak shape on the error in the peak position. This information can be generated in a simulation process and does not necessarily have to be generated by a diffraction experiment. Provided that the general shape of a neutron diffraction peak is known beforehand, peaks of any length and shape can be numerically simulated [2.1]. Numerical simulation leaves the 'experimentalist' completely free to generate peaks according to his wishes. As such, the influence of any measurement parameter can be studied over a broad range in small steps, which would hardly be feasible in actual experiments.

The simulated peaks are used as input for a peak fitting procedure that gives the estimated statistical error in the parameter 'peak position'. The influence of the peak parameters on the statistical error of the peak position can thus be studied.

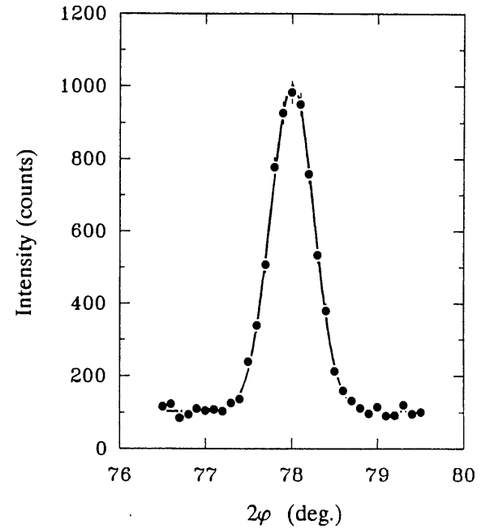

Fig. 2.3 Example of a Gaussian curve with $2\theta = 78°$, $\sigma_{FWHM} = 0.6°$, $I_0 = 900$ counts and $I_b = 100$ counts. The solid curve represents the exact mathematical curve; the data points represent the Poison deviates based on the mathematical curve. The error bars have a length equal to the square root of the intensity (only visible at the data points of high intensity).

2.2.1 Diffraction peak simulation

Unlike in x-ray diffraction, the diffraction peak obtained in a neutron diffraction experiment can be approximated very closely to a Gaussian profile [2.2]

$$I = I_0 \, e^{-4\ln 2 \frac{(2\varphi - 2\theta)^2}{\sigma^2_{FWHM}}} + I_b \qquad (2.1)$$

where

I:	measured count;
2θ:	peak position;
σ_{FWHM}:	full width at half maximum;
I_0:	intensity count at the peak position;
I_b:	background count.

Equation 2.1 is represented in figure 2.3. A diffraction peak measurement could be simulated by simply calculating an array of intensities according

to equation 2.1. However, Such a profile would not contain any influence of the counting statistics present in a real experiment. The calculated intensities should be scrambled just like in a real experiment that suffers from counting statistics. Counting statistics are known to show a Poison behaviour. This behaviour can be implemented in the following way, the obtained intensity values I are one by one used as input for a numerical routine that returns a random draw from a Poison distribution with a mean value I. This closely resembles the reality in a measurement. The variance of a counted number that we have now simulated, is always equal to the measured value itself [2.3]. Hence for an estimate of the standard deviation of the simulated intensities, their square roots should be taken. This is needed to estimate the error in the peak position during the subsequent fitting procedure. In figure 2.3 the result of this Monte Carlo simulation process is shown.

2.2.2 Influence of measurement parameters.

The parameters that determine the arrays containing a measured diffraction peak fall in two classes: measurement parameters and physical parameters. In a real experiment these parameters are chosen by the experimentalist. The measurement parameters are

1. measurement time;
2. step size between the points;
3. total scan length.

Physical parameters are not influenced by the way the experiment is arranged. The physical parameters are

1. peak position;
2. full width at half maximum (FWHM);
3. peak to background ratio.

In figure 2.4 to 2.8 the influence of these parameters on the precision of the peak position determination is given. The influence of the physical parameter 'peak position' is not studied as it has no influence on the error. The data points in these figures are obtained by fitting a Gaussian profile (equation 2.1) to the results of the simulation process described

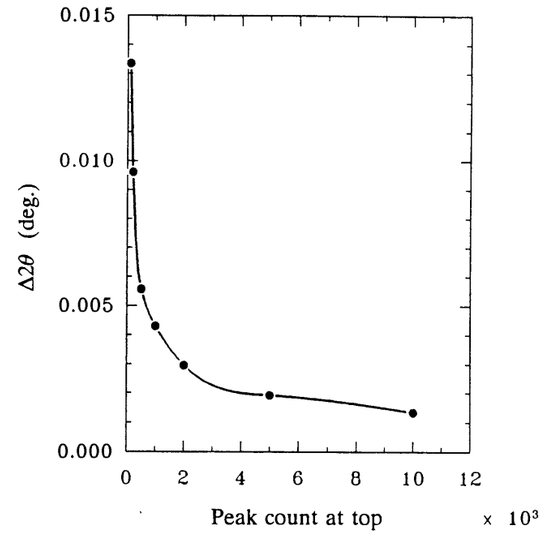

Fig. 2.4 Influence of the count number at the top of Gaussian shaped peak profiles on the standard deviation $\Delta 2\theta$ of the peak position 2θ. The data points have been obtained from Gaussian fits to simulated peaks. The solid curve serves as a guide to the eye.

in 2.2.1. For the present investigations, Table 2.1 shows the values at which the peak parameters are kept fixed when their influence is not studied. The employed fitting method is the algorithm of Levenberg-Marquardt [2.4] which was implemented on a personal computer.

Measurement time

In figure 2.4, the precision of the peak position is given as a function of a quantity that is proportional to the measurement time: the number of counts at the top of the profile. The coefficient of proportionality is unknown. It can be obtained from a trial experiment on a specimen in the experimental configuration one likes to study. The figure shows a quadratic relationship, meaning that when the amount of peak counts is multiplied by 2, the error is reduced by a factor $\sqrt{2}$. The peaks are simulated for a FWHM value of 0.6°, which is approximately equal to the instrumental resolution of our instrument, as will be described in the following chapters. From figure 2.4 it is seen that a counting time

corresponding to a peak count of 1000 counts, the precision is about 0.004°. This is usually sufficient for stress measurements.

Simulations clearly do not give general results. When, for example, the FWHM or the peak to background ratio differ from the values given in Table 2.1, the amount of peak counts needed for an acceptable error level will also be different. Separate simulations should be performed for each case in order to conclude which amount of peak counts results in an acceptable error level. Unfortunately, the decisive factor for the measurement time is more likely to be the time available for a peak scan, than the (low) error level one likes to achieve. In that case the simulations may help to conclude beforehand whether performing the measurement is realistic.

Step size.

The influence of the step size on the peak position error is given in figure 2.5. The figure shows that taking half the step size (all other parameters remaining constant) reduces the uncertainty in the peak position by a factor of $\sqrt{2}$. On the other hand, taking half the step size doubles the total time needed for the experiment. So we arrive at an interesting conclusion that it does not matter whether the total measurement time is consumed in terms of counting time per scan point or in terms of the step size. Eventually a general square root relationship describes both influences

Table 2.1

Fixed values for the peak parameters that are in effect when their influence is not subject to study in the simulation experiments.

parameter	value
peak position*	78°
full width at half maximum	0.6°
peak to background ratio	900/100
nr. of counts at peak position	1000
step size	0.1°
scan length (× FWHM)	2

* Influence of parameter is not studied.

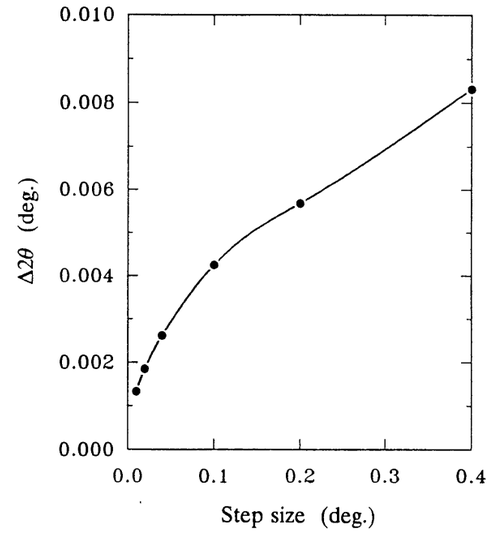

Fig. 2.5 Influence of the step size employed during the registration of a diffraction peak profile, on the standard deviation $\Delta 2\theta$ of the peak position 2θ. The data points result from Gaussian fits to simulated profiles. The solid curve serves as a guide to the eye.

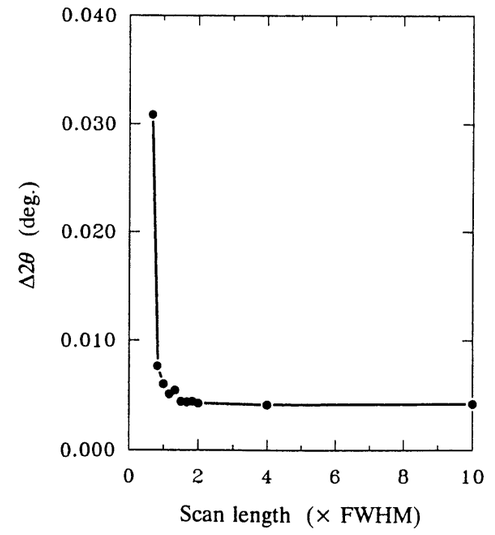

Fig. 2.6 Influence of the scan length in units of full width at half maximum on the standard deviation $\Delta 2\theta$ of the peak position 2θ. The data points result from Gaussian fits to simulated peak profiles. The solid curve serves as a guide to the eye.

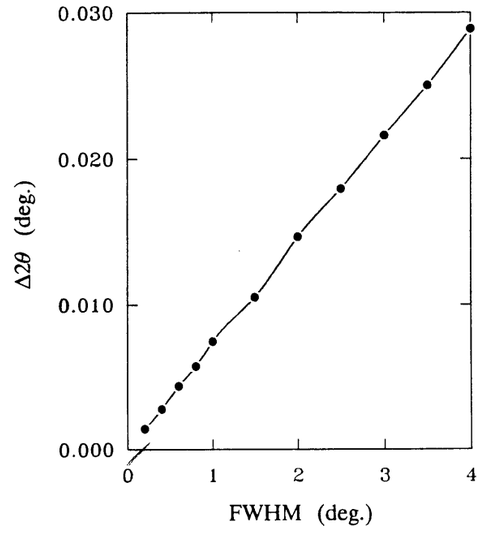

Fig. 2.7 Influence of the full width at half maximum on the standard deviation $\Delta 2\theta$ of the peak position 2θ. The data points result from Gaussian fits to simulated profiles. The solid curve serves as a guide to the eye.

$$\Delta 2\theta = \text{const.} \sqrt{\frac{\text{stepsize}}{\text{counting time per scan point}}} \qquad (2.2)$$

Scan length

In figure 2.6, the influence of the scan length is given. The scan length is expressed in (dimensionless) units of FWHM in order to make the results more generally applicable. As far as the precision of the peak position determination is concerned, it is unnecessary to apply scan lengths longer than twice the FWHM value. Simulation results from longer scans show no improvement in precision. This is a very important conclusion as this is in fact the best possible way of using the available beam time as efficiently as possible. Performing scans over a scan range longer than twice the full width at half maximum is a waste of time when the main interest is in a precise determination of the peak position. It should be noted, that this conclusion is not valid for the fit parameters I_b and σ_{FWHM}

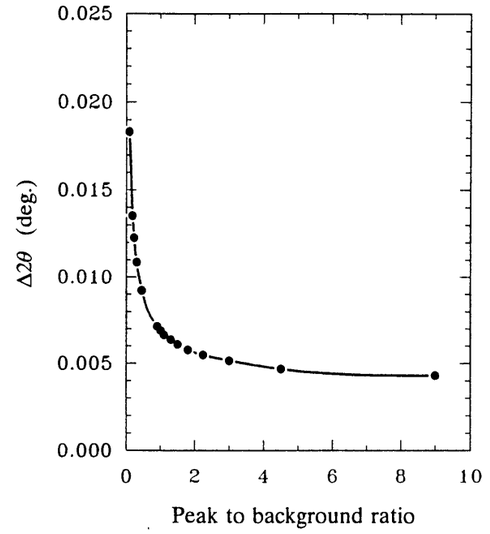

Fig. 2.8 Influence of the peak to background ratio on the standard deviation $\Delta 2\theta$ of the peak position 2θ (the value of the peak counts above the background is considered to be constant in these results, so that the p/b ratio is changed by varying the background value only). The data points result from Gaussian fits to simulated profiles. The solid curve serves as a guide to the eye.

of equation 2.1. Fortunately, the precision demands on these parameters are not as high as those on the peak position.

FWHM

In figure 2.7 the uncertainty in the peak position as a function of the physical parameter FWHM is given. The relationship is linear. As a result of its physical nature, the FWHM cannot be changed by the experimentalist, for a given diffractometer and specimen. In view of the foregoing, the results are dramatic. Assume that the FWHM increases by a factor of 2. As a consequence, the error in the peak position will also increase by a factor of 2. According to equation 2.2, the counting time per scan point has to be multiplied by $2^2 = 4$, in order to accommodate for this. The number of scan points is multiplied by 2 in order to maintain the same scan length in terms of FWHM, so the total measuring time for the peak determination will be 8 times longer (in the simulations we have used a constant step size, whereas the scan length is kept constant

relative to the FWHM which has now changed, see Table 2.1). So when the scattered intensity remains unchanged the peak determination takes 8 times as long. However, when two materials, possessing the same chemical composition, show peaks for which the FWHM values differ by a factor of 2, the peak intensity inevitably drops by the same factor. An extra factor of 2 in counting time per scan point is needed to accommodate this. So ultimately, the measurement time is multiplied by 16 in order to maintain the same precision. An example of this is a martensitic steel, which in the hardened state has exactly the same composition as in annealed state. However, the difference in diffraction line width can be as high as a factor of 4, resulting in an overall increase in the measurement time which can be as high as 256 times.

Peak to background ratio

In figure 2.8, the effect of the peak to background ratio on the uncertainty in the peak position is given. The simulated peaks are chosen to be always 900 counts over background level. It is clear from the figure that trying to improve the peak to background ratio beyond 2 is not helpful. If the peak to background ratio becomes smaller than 2, however, the uncertainty rapidly increases. Unfortunately, the requirements for small sample volumes, which is characteristic for stress measurements by means of neutron diffraction, often results in very small value for the peak to background ratio. It is therefore important to reduce the background level around the diffractometer set-up to the lowest possible value by employing adequate radiation shielding wherever possible.

2.2.3 The use of diffraction profile simulations

In the previous section, the influence of a number of experimental parameters on the precision of diffraction peak determination is discussed. For this purpose we used simulated diffraction data. In measurement practice, this type of simulations helps the investigator to predict the measurement precision after having performed a trial experiment for every peak that is needed for the stress measurement. The trial experiments deliver values for the peak to background ratios, the full widths at half maximum and the peak positions as well as for the counting rates. The trial experiment thus helps to find realistic values for the parameters, that we have arbitrarily set to the values of Table 2.1, for

the present simulations. The discussed simulation technique may help to establish the measurement parameters step size, scan length and counting time which must be employed in order to achieve an adequate measurement precision in the shortest measuring time possible. The trial experiments take only a fraction of the total time needed for a complete stress measurement. As stress measurements by means of neutron diffraction are very time consuming, the combination of trial experiments and this type of simulations help the experimentalist to plan the measurements such that no neutron beam time is wasted. The only thing the experimentalist has to know beforehand is the precision he requires in peak position. This is also governed by the beam time available.

2.3 THE UMBRELLA EFFECT

In the foregoing, the diffraction peak obtained in a neutron diffraction experiment, is assumed to be of Gaussian shape. The top of this Gaussian corresponds to the diffraction peak position. It has been mentioned in the introduction that the shape and position of a real diffraction peak will be slightly different from this situation. The peak shape is neither exactly Gaussian nor is the peak position equal to the maximum intensity position of the curve. This was stated to be due to several effects. One of these effects, the so called 'umbrella effect' will be the subject of discussion in the following sections. It will be shown that the umbrella effect strongly depends on the geometry and location of the neutron beam limiting apertures which are characteristic for the neutron stress measurements described in this work.

2.3.1 Theoretical profile

In a powder diffraction experiment on a point sample in a horizontally placed diffractometer, a cone of diffracted radiation is spread out by the sample. As can be seen from figure 2.1, the direction of the intersection line of the cone and the horizontal plane that includes the sample is the peak position we want to determine. In order to exclusively detect diffracting neutrons that are moving along this intersection line, the vertical opening in the detector should be very small. In order to obtain a reasonable neutron count rate, however, the sample can not be a point

sample, nor can the detector height be very small. Increasing the detector height causes diffracting neutrons that are not moving along the line that defines the peak position, to contribute to the detected intensity. During a diffraction peak scan, this causes an apparent peak shift towards the axis of the diffraction cone. The finite height of the sample adds to the complexity of this problem.

Van Laar and Yelon [2.5] derived a function that gives the diffraction profile for what they call an ideal instrument and an ideally scattering sample. By 'ideal' they mean that the instrument under consideration has a perfectly parallel beam and the scattering of this beam by means of diffraction of every point in the sample takes place according to a delta function. When in this ideal situation, the finite dimensions of the sample and the detector are taken into account, a theoretical peak can be calculated. This peak shows a one sided broadening. Van Laar and Yelon state in their article that this one side broadening effect can be neglected in neutron powder diffraction measurements above a scattering angle 2φ of about 45°. In powder diffraction practice this statement has proven to be true. However, in the practice of stress measurements by means of neutron diffraction the geometrical situation might be quite different from the powder situation, as the instrumental parameters used by van Laar and Yelon are different than those needed in a stress measurement set-up. This is mainly due to the use of beam apertures in the incident and diffracted beams. Because of the importance of the umbrella effect in our measurements, we shall briefly review the theory given by van Laar and Yelon.

Consider a diffraction experiment at a nominal diffraction angle 2θ using a counter of height $2H$ rotating at a radius L around a sample of height $2S$. For $H \geq S$ the theoretical diffraction profile is given by [2.5]

$$D(2\varphi,2\theta) = \frac{L}{2HS\ h\ \cos 2\varphi} W(2\varphi,2\theta) \tag{2.3}$$

where

$$h = L\sqrt{\left(\frac{\cos 2\varphi}{\cos 2\theta}\right)^2 - 1} \tag{2.4}$$

The weight function $W(2\varphi,2\theta)$ is a geometry dependent function for which three regions are distinguished

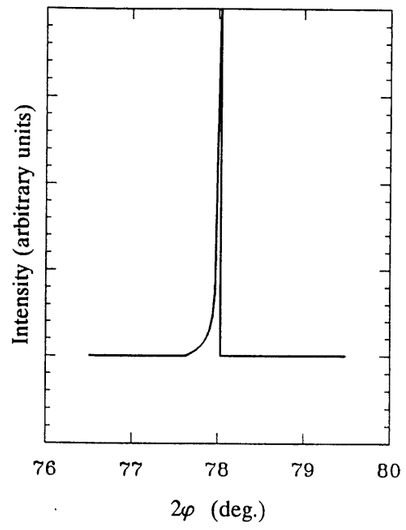

Fig. 2.9 Theoretical diffraction profile due to the umbrella effect. $2H = 20$ mm, $2S = 20$ mm, $2\theta = 78°$ and $L = 110$ mm. This profile is a one side broadened delta function, so that at $2\varphi = 2\theta$ the intensity actually reaches infinity.

$$\begin{aligned} W(2\varphi,2\theta) &= 0 && ;\ h \geq H + S \\ W(2\varphi,2\theta) &= H + S - h && ;\ H + S > h \geq H - S \\ W(2\varphi,2\theta) &= 2S && ;\ H - S > h \geq 0 \end{aligned} \tag{2.5}$$

In figure 2.9 an example of this theoretical diffraction profile is given for a geometrical situation, that is frequently encountered in neutron stress measurement practice.

Van Laar and Yelon have derived these equations for an ordinary powder diffractometer in which the parameters S, H and L are very well defined. Moreover, these parameters are constant throughout the measurement of a powder diagram. For our application of this theory, L the distance from the sample to the counter needs some special attention. The value that should be used as the detector distance L is the distance where the vertical window, that determines the part of the diffraction cone that is eventually 'seen' by the detector is situated. In the stress measurement configuration, this vertical restriction window is found in

the secondary slit assembly. (See the treatment of this set-up in Chapter 4). It is the mask possessing the smallest height and at the same time is situated closest to the counter. This height is then called as $2H$.

2.3.2 The total profile

Unfortunately, the theoretical peak that was derived in the previous section can never be measured. The peak that will be measured in a real diffraction experiment is a combination of the theoretical peak, the instrumental resolution function and the sample response function. Mathematically this combination can be interpreted as a convolution [2.6]. The resolution function, convoluted with the sample response function, $R(\Delta,2\theta)$, can be closely approximated by a Gaussian as

$$R(\Delta,2\theta) = \frac{1}{A\sqrt{\pi}}\, e^{-(\Delta/A)^2} \tag{2.6}$$

where

$$A = \frac{\Gamma}{2\sqrt{\ln 2}} \tag{2.7}$$

For Γ in equation 2.7, van Laar and Yelon take the instrumental resolution only. In our analysis, besides instrumental resolution, we let all sample influences to contribute to Γ. Examples of these influences are the microstrain and the coherent domain size. We assume that the sample influence on the sample/resolution function does not alter its Gaussian nature.

Mathematically it is an advantage with neutron diffraction that the resolution/sample function can be represented by such a simple function as a Gaussian. This is in contrast with x-ray diffraction where the resolution function is neither symmetrical nor Gaussian due to $K\alpha_2$.

The convolution of the theoretical profile and the resolution/sample function has the following form

$$y(2\varphi) = \int_{-\infty}^{\infty} D(\Delta,\, 2\theta)R(2\varphi - \Delta,\, 2\theta)\mathrm{d}\Delta \tag{2.8}$$

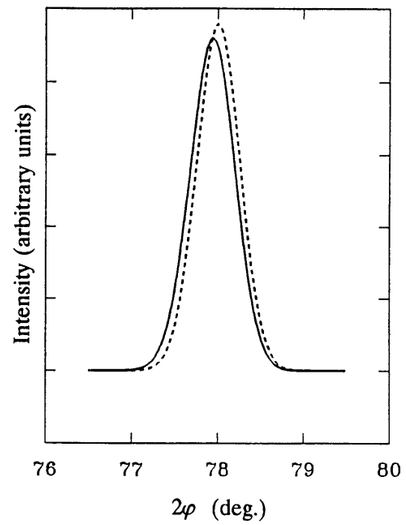

Fig. 2.10 Two calculated diffraction curves. For the solid curve, the umbrella effect is taken into account. The dashed curve is calculated without taking the umbrella effect into account. The solid curve is the result of a convolution of the dashed curve with the theoretical profile that was given in figure 2.9.

Unfortunately, the convolution of equation 2.8 cannot be calculated analytically. It can, however, be carried out numerically. The integration algorithm used is a Gauss-Legendre quadrature [2.7]. The limits of integration, which in the numerical case can not be infinite, follow from an analysis of equation 2.5. Using equation 2.4 the condition $h \geq H + S$ can be rewritten as

$$2\varphi \leq 2\varphi_{\min} \tag{2.9}$$

where

$$2\varphi_{\min} = \arccos\left[\cos 2\theta \sqrt{\{(H + S)/L\}^2 + 1}\,\right] \tag{2.10}$$

Using 2.9 and 2.10, equation 2.8 is rewritten as

$$y(2\varphi) = \int_{2\varphi_{\min}}^{2\theta} D(\Delta,\, 2\theta)R(2\varphi - \Delta,\, 2\theta)\mathrm{d}\Delta \tag{2.11}$$

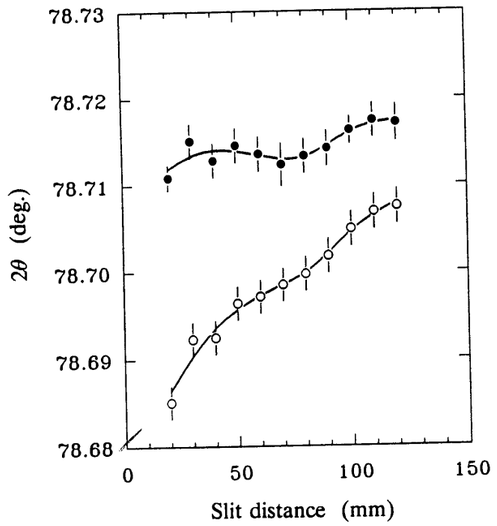

Fig. 2.11 Results of a Gaussian fit (open symbols) and a fit based on the convolution function that is described in the text (dark symbols) on diffraction profiles that have been obtained from a powder specimen. The results are given as a function of the distance of the secondary beam aperture to the sample.

Equation 2.11 can be used as the model function in a Levenberg-Marquardt fitting procedure [2.4]. The result for the parameter 2θ is then the position of the top of the diffraction peak corrected for the umbrella effect, while Γ, another free parameter in this fitting process, characterizes the sample/resolution function.

In Figure 2.10 two calculated diffraction profiles are given. Both having the same 2θ but one is calculated according to a Gaussian curve, while the other is calculated according to the convolution function described by equation 2.11. From the figure it is clearly visible that the influence of the umbrella effect on the peak position is fairly large, while the influence on the form of the peak can be neglected.

In a stress measurement, a number of peaks are measured. Normally, these different peaks are measured in completely different geometrical circumstances (*i.e.* different values for $2H$, $2S$ and L). In figure 2.11 an example of the influence of the umbrella effect for a number of diffraction peaks, taken from the same sample with different values for the aperture distance L is given. In the figure, the results of a simple

Gaussian peak fit and a peak fit using equation 2.11 are compared. As the measurements all stem from the same (powder) sample, every peak should yield the same peak position 2θ. The Gaussian fit function does not give this result, while the convolution function that has been described in this section does.

The conclusions that can be drawn from figure 2.11 are that the umbrella effect influences this type of measurements and that the convolution function presented here, should be employed for the peak fitting procedure whenever the umbrella effect is different for the various diffraction peaks that have to be measured in order to determine a stress state.

2.4 ATTENUATION OF THE NEUTRON BEAM

A neutron beam of intensity I_0, that enters a piece of material loses intensity as it proceeds through the material. The intensity is diminished because of two processes: diffraction and absorption. The sum of both these effects is defined as: *beam attenuation*. The beam attenuation strongly depends on the composition and the texture of the material. For x-rays the situation is vastly different, because the attenuation is more related to absorption and the texture of the material does not influence this. The attenuation is described by a simple formula of the Lambert-Beer type:

$$I = I_0 e^{-\mu D} \tag{2.12}$$

In equation 2.12, μ is the coefficient of attenuation, D is the flight path of neutrons through the material. D depends on the form of the specimen and its orientation in the neutron beam geometry as well as on the neutron beam geometry itself.

As was already pointed out in the introduction to this chapter (see figure 2.2), one of the parameters that determine the beam geometry is the counter angle 2φ. So, during a scan with this variable, which is performed in order to determine the position of a diffraction peak, the beam geometry changes. According to equation 2.12, this influences the intensity that is measured at the different scan positions. Suppose for instance we take the beam path D to be longer at the low 2φ-side of the scan than at the high 2φ-side of the scan which is the case for $\psi < \varphi$ (*cf.*

figure 2.2). As a consequence, the measured intensity is lower at the low 2φ-side, while at the high 2φ-side it is higher. Hence the top of the measured peak will shift to a higher 2θ value. This process results in a systematic error. The magnitude of this error depends on other geometrical parameters such as the depth below the surface of the sampling volume and the orientation and shape of the specimen. It is easy to imagine that in a situation where the beam hits the specimen under a grazing angle, the attenuation effect will be larger than at angles of incidence that are more or less perpendicular to the specimen.

It is possible to express D in the relevant geometrical parameters. Knowing this expression, and knowing μ, the intensity scattered from a specific region of the specimen – the sampling volume – can be calculated by integration over this volume. When this calculation is repeated for the 2φ values that together form a scan, a series of correction factors that are all slightly different from each other can be made. When the measured intensities that belong to the series of 2φ values are multiplied with the series of correction factors, the diffracted intensity, suffering no neutron attenuation at all, can be reconstructed. In practice one can take $I_0(2\varphi)$ from equation 2.12 as the corrected intensity. When the array of corrected intensities is used as input for a peak fitting algorithm, the peak position for the case of no attenuation is obtained and so, the systematic error due to attenuation effects is eliminated.

The problem of how to deal with the attenuation effect is now reduced to the solution of a volume integral. In this problem, the determination of the integration boundaries is the most complicated part. We have attacked the problem in two phases:

1. The incident and diffracted neutron beam flight paths will be regarded as lines. Subsequently, the sampling volume reduces to a point. The function that gives the flight path as a function of the geometrical parameters is now easily derived on the bases of a geometrical treatment. When correction factors would be calculated from this approach, the changes in sample volume during a 2φ-scan are neglected.
2. The neutron beam will be regarded as a parallel set of incident and diffracted beams, each pair corresponds to a geometry described above. This set is extended such that the points in the specimen belonging to each pair together form the sampling volume. The boundaries of this continuum will be expressed in the parameters that determine the sampling volume so that the integration can be carried out numerically. The beam aperture and the beam divergence enter the derivations here.

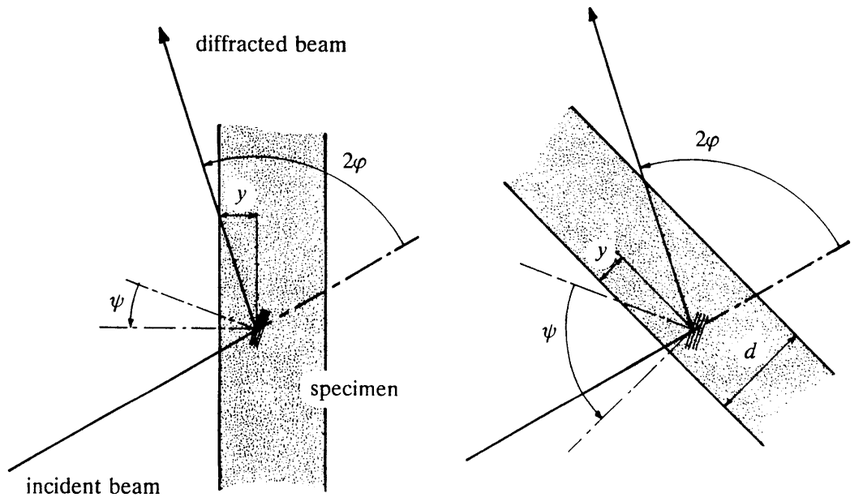

Fig. 2.12 A bar shaped specimen in the neutron beam geometry. The total flight path through the material can be calculated from the geometrical parameters y, φ, ψ and d.

2.4.1 The flight path as a function of the scattering angle

In the discussions of this section, the specimen is assumed to be bar-shaped (other specimen forms, which are not included in this chapter lead to analogous considerations). In figure 2.12, the contours of the bar-shaped specimen are drawn in a simplified neutron beam geometry. The orientation of the specimen in the neutron beam geometry is given by the offset angle ψ, the angle of the surface normal with the bisector of the angle between primary and diffracted neutron beams. The flight path is separated into two parts. The total flight path of primary and diffracted beams within the material, which depends on the depth below the surface y can now be calculated.

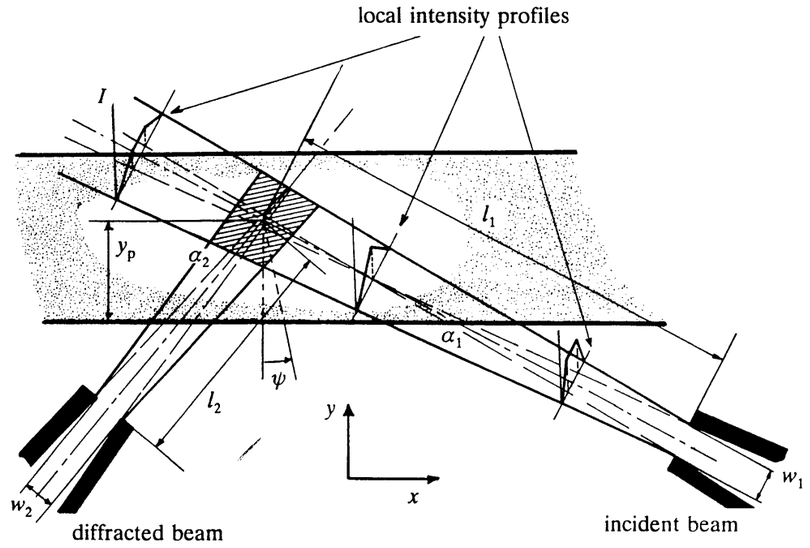

Fig. 2.13 Geometry of the primary and secondary neutron beams, showing the effects of the divergence of the beams (α_1,α_2) and the widths of the apertures (w_1, w_2) as well as the aperture to specimen distances (l_1,l_2).

For $0 \leq \psi < \varphi$

$$D = \frac{y}{\sin(\varphi - \psi)} + \frac{y}{\sin(\varphi + \psi)} \tag{2.13}$$

and for $\varphi \leq \psi \leq 90°$

$$D = \frac{y}{\sin(\psi + \varphi)} + \frac{d - y}{\sin(\psi - \varphi)} \tag{2.14}$$

These equations are sufficient for calculating the series of correction factors belonging to the measurement points of a narrow diffraction peak when the diagonal length of the sample volume is small compared to the flight path through the specimen using

$$f(2\varphi) = \frac{e^{\mu D(2\varphi)}}{e^{\mu D(2\theta)}} \tag{2.15}$$

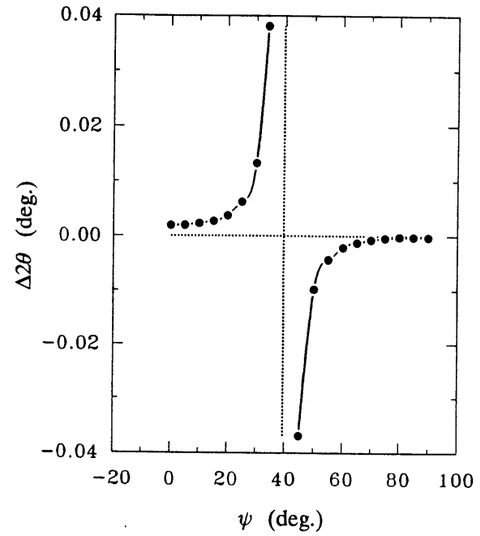

Fig. 2.14 The effect of the orientation angle ψ on the measured position of a diffraction peak according to the integration model derived in the text. Here $w_1 = w_2 = 1$ mm, $\alpha_1 = \alpha_2 = 0.5°$, $l_1 = l_2 = 50$ mm, $y_p = 3$ mm, $d = 10$ mm and $2\varphi = 78°$.

Here we have restricted ourselves to bar shaped specimens. For specimens having a form other than a rectangular bar, equations 2.13 and 2.14 will have to be replaced by similar ones, describing the beam path length in those specimens.

2.4.2 Integration over the sample volume

When the diagonal length is not small compared to the flight path, the correction factors must be calculated from an integration over the sampling volume. For this purpose, the equations for the lines that form the boundaries of the rhombus must be calculated. Subsequently, the integration over the rhombus can be performed. The integration over the vertical co-ordinate (z) is not necessary as nothing changes in that direction during a 2φ-scan. The function to be integrated is equation 2.12, in which D is replaced by one of the equations 2.13 or 2.14. So

$$f(2\varphi) = \frac{\iint_{\text{rhombus}} e^{\mu D(y,2\varphi)} I_p(x,y,2\varphi) I_d(x,y,2\varphi)\,dx dy}{\iint_{\text{rhombus}} e^{\mu D(y,2\theta)} I_p(x,y,2\theta) I_d(x,y,2\theta)\,dx dy} \tag{2.16}$$

The functions $I_p(x,y)$ and $I_d(x,y)$ in equation 2.16 are intensity weight functions for the primary and secondary beam respectively. They depend on the parameters that determine the beam geometry. As is shown in figure 2.13 there exist regions of different intensity in the rhombus, their locations depending on how the geometrical parameters are chosen. The derivation of the intensity weight function can be based on a trapezoid shaped intensity function of both the primary and the secondary beams. The exact beam intensity pattern is governed by the beam divergence α_1; the counter divergence α_2, the distance of the beam apertures to the sample region: l_1 and l_2 and the width of both apertures w_1 and w_2. The calculation of the intensity weight function is straightforward although it involves a lot of awareness of the factors contributing to the geometry.

By far the most important parameter for the attenuation effect is the orientation angle ψ. As an example, in figure 2.14 the effect of the specimen orientation angle ψ on the peak position shift due to the attenuation effect is shown. The calculations leading to the plot are performed using a computer program that takes care of the above described geometry. The conclusion of the simulations that led to figure 2.14 is that the absorption correction should not be omitted whenever the effect is different for the peaks that have to be measured in order to determine a stress state.

REFERENCES

2.1 W.H. Press; B.P. Flannery; S.A. Teukolsky and W.T. Vetterling, *Numerical Recipes*, Cambridge University Press, 203ff (1986).

2.2 G.E. Bacon, *Neutron Diffraction*, Oxford University Press, 130ff (1975).

2.3 P.R. Bevington, *Data Reduction and Error Analysis for the Physical Sciences*, McGraw-Hill, 36ff, (1969).

2.4 W.H. Press; B.P. Flannery; S.A. Teukolsky and W.T. Vetterling, *Numerical Recipes*, Cambridge University Press, 509ff (1986).

2.5 B. van Laar and W.B. Yelon, *J. Appl. Cryst.*, **17**, 47 (1984).

2.6 J.M. Cowly, *Diffraction Physics*, North Holland, 25ff (1975).

2.7 W.H. Press; B.P. Flannery; S.A. Teukolsky and W.T. Vetterling, *Numerical Recipes*, Cambridge University Press, 121ff (1986).

3
Theory of Elasticity for Stress Measurements

3.1 INTRODUCTION

When a force is applied to a material, the material is said to be in stressed condition. Stress is defined as the amount of applied force per unit area.

Stress is a quantity used by constructors, in order to qualify the strength of a material or to indicate how far from the ultimate strength a material in a piece of work is loaded in a specific construction.

Usually, a material is subject to two classes of stress.

1. Applied stress, which is a result of using the construction for what it has been designed.
2. Residual stress, which is a result of fabrication processes (rolling, welding, forging *etc.*) and/or wear processes during use.

The actual loading of the material is due to the sum of both the applied and residual stresses.

Stress is a quantity that cannot be measured. There are, however, numerous possibilities to measure one of the direct consequences of stress. To mention a few: elongation (*i.e.* strain), change in electrical conductivity, change of the velocity for the propagation of ultrasound *etc*. The stress measurement method that is the subject of the present studies – neutron diffraction – uses the crystallographic lattice spacing of a stack of lattice planes as an internal strain gauge. Diffraction stress measurement methods do not differentiate between applied stress and residual stress. As the applied stress can usually be accounted for, this does not pose a serious problem to our measurement technique. Both

classes of stresses can always be separated. (The opposite is encountered when the stress is measured by resistance strain gauges. They only reveal the applied stress level and not the residual stress that was present before gluing the strain gauge to the surface of the material).

In order to determine the stress state from measured strain data, one needs a relationship between stress and strain. Only then the *engineering quantity* stress can be calculated from the *physical quantity* strain. Unfortunately, even strains cannot be measured by means of diffraction. What can be measured by means of diffraction, are lattice plane distances. Consequently, in order to perform stress measurements by means of neutron diffraction, a relationship between the lattice plane distance and the strain has to be established. Having solved for the strain one way or another, this can subsequently be translated into stress.

It will be shown that both stress and strain are represented by tensors. The strain in an arbitrary direction of a point in space can be expressed in the elements of a tensor that is defined in an arbitrary co-ordinate system. The strain tensor in any other co-ordinate system can be derived from the present one by an adequate co-ordinate system transformation.

In this chapter, the relationship between measurable quantities (*i.e.* lattice plane distances) and the elements of the strain tensor will be presented. This relationship contains the six elements of the strain tensor and the stress free lattice parameter. In principle all seven parameters are unknowns. It will be shown that the solution of all seven unknowns from a set of seven or more of these equations is impossible, unless some additional information about the stress state is known. This additional information will be obtained from so called 'constraint equations'. Constraint equations will be given for some specific experimental circumstances.

The mathematical representation of the process described above, will fill the major part of this chapter. Its development has led to a computer program that takes care of all the data reduction steps necessary for determining the stress state from measured diffraction data. In that program, the theoretical aspects of the form and position of diffraction peaks that were discussed in the previous chapter, are also involved.

3.2 THE STRAIN TENSOR

First the specimen co-ordinate system *Oxyz* is defined. With respect to this co-ordinate system the second order strain tensor ε_{ij} is defined. The diagonal elements of this tensor represent the strain in the axis directions; the off-diagonal elements represent the shear in planes containing two of the axes of the system. The strain tensor fully describes the strain state of a small volume element in a material. Fully written, the tensor has the following shape

$$\varepsilon_{ij} = \begin{pmatrix} \varepsilon_{11} & \varepsilon_{12} & \varepsilon_{13} \\ \varepsilon_{12} & \varepsilon_{22} & \varepsilon_{23} \\ \varepsilon_{13} & \varepsilon_{23} & \varepsilon_{33} \end{pmatrix} \tag{3.1}$$

The main advantage of writing the strain tensor this way is that the – numerically attractive – diagonalization of the matrix of equation 3.1 automatically yields the principal strain tensor. This in contrast to the so called Voigt notation, which we will come across later in this chapter. The diagonalization of equation 3.1 corresponds to a co-ordinate transformation to the so called principle co-ordinate system, which is the unique system in which the shear stresses (the off-diagonal elements of 3.1) vanish.

$$\varepsilon_i^D = \begin{pmatrix} \varepsilon_1^D & 0 & 0 \\ 0 & \varepsilon_2^D & 0 \\ 0 & 0 & \varepsilon_3^D \end{pmatrix} \tag{3.2}$$

The transformation of a strain tensor on the principal co-ordinate system is always possible because the strain tensor is symmetric, so that the matrix that describes the tensor has three undependent eigenvectors which are mutually perpendicular.

Transformation of tensors is generally described by the following equation

$$\varepsilon'_{ij} = c_{ik} c_{jl} \varepsilon_{kl} \tag{3.3}$$

In equation 3.3 c_{ij} symbolizes the cosine matrix that gives the relation between the co-ordinate systems before and after transformation. Of the many cosine matrices possible there is only one that transforms ε_{ij} such that ε'_{ij} is the principal strain tensor.

An alternative notation for the strain tensor is the Voigt notation [3.1]. The Voigt notation has the advantage that tensors of the fourth order, like the elastic bi-tensor which will be discussed in the next section, can appear as a matrix. The Voigt notation for the strain tensor is

$$\boldsymbol{\varepsilon} = \varepsilon_i = \begin{pmatrix} \varepsilon_{11} \\ \varepsilon_{22} \\ \varepsilon_{33} \\ 2\varepsilon_{12} \\ 2\varepsilon_{13} \\ 2\varepsilon_{23} \end{pmatrix} = \begin{pmatrix} \varepsilon_1 \\ \varepsilon_2 \\ \varepsilon_3 \\ 2\varepsilon_4 \\ 2\varepsilon_5 \\ 2\varepsilon_6 \end{pmatrix} \tag{3.4}$$

For the stress tensor σ_{ij} that will be encountered in the next section analogous rules apply as for the now presented strain tensor.

3.3 STIFFNESS AND COMPLIANCE

The relationship between the stress tensor and the strain tensor is given by Hooke's law [3.2]. The tensor that characterizes this relationship is called the elastic stiffness tensor. It is a fourth order symmetric tensor

$$\sigma_{ij} = C_{ijkl}\varepsilon_{kl} \tag{3.5}$$

Equation 3.5 represents 9 algebraic equations, each equation having 9 terms at the right hand side. As a consequence, the elastic behaviour of a material is described with 81 constants. As C_{ijkl} must be symmetrical due to the symmetry of σ_{ij} and ε_{kl}, only 36 different constants remain. It can be proved that also

$$C_{ijkl} = C_{klij} \tag{3.6}$$

This reduces the number of independent variables to 21. This amount of variables suffices to describe the elastic behaviour of a material that possesses the largest possible anisotropy. A material that obeys equation 3.5 is called linearly elastic. Some materials, especially textured materials (*i.e.* showing preferred orientation of crystallites) do, in principle, not behave according to linear elastic laws.

Depending on the symmetry of the crystal structure, the number of independent constants that appear in equation 3.5 can dramatically be reduced. The minimum required amount of variables, however, is limited to 2. In that case the material is called elastically isotropic. For isotropic materials equation 3.5 becomes

$$\sigma_{ij} = \frac{\nu E}{(1+\nu)(1-2\nu)}\,\delta_{ij}\varepsilon_{kk} + \frac{E}{(1+\nu)}\,\varepsilon_{ij} \tag{3.7}$$

where

δ_{ij} : the Kronecker symbol ($\delta_{ij} = 1$ for $i = j$; $\delta_{ij} = 0$ for $i \neq j$);
ν : Poisons ratio;
E : Youngs modulus.

In Voigt notation equation 3.5 is written

$$\sigma_i = C_{ij}\varepsilon_j \tag{3.8}$$

The inverse of the stiffness tensor is called the compliance tensor S_{ijkl} so that in Voigt notation

$$C_{ij}S_{jk} = \delta_{ik} \tag{3.9}$$

3.4 MEASURED QUANTITIES

The strain tensor ε_{ij}, defined relative to the co-ordinate system *Oxyz* that is fixed in the sample may be determined from a number of measurements of the strain e in different directions. In the introduction it was pointed out that the strain value cannot be directly obtained in a diffraction experiment. For the next derivation, however, we will forget this for a while. In the course of the derivation it will become clear how

to express the elements of the strain tensor in quantities that can be measured: lattice plane distances.

The different directions are obtained by choosing different sample orientations with respect to the scattering vector $\boldsymbol{q}$. If for the i^{th} strain measurement, the direction of $\boldsymbol{e}$ is defined by the direction cosines $(k_i l_i m_i)$ then

$$e(k_i l_i m_i) = k_i^2 \varepsilon_{11} + l_i^2 \varepsilon_{22} + m_i^2 \varepsilon_{33} + \\ + 2k_i l_i \varepsilon_{12} + 2k_i m_i \varepsilon_{13} + 2l_i m_i \varepsilon_{23} \tag{3.10}$$

The derivation of equation 3.10 is based on the elongation of a unit vector $\boldsymbol{k} = (k_i l_i m_i)$ placed in a strain field represented by ε_{ij}. During this derivation, quadratic terms in the elongation expressions are systematically ignored. It is a cumbersome piece of work that is given in most textbooks on mathematical elasticity [3.3].

The left hand member of equation 3.10 can be written as

$$e(k_i l_i m_i) = \frac{d(k_i l_i m_i) - d_0}{d_0} \tag{3.11}$$

In equation 3.11, $d(k_i l_i m_i)$ is the lattice spacing for lattice planes oriented according to $\boldsymbol{k}$, d_0 is the lattice spacing when no stress is present. In 3.11, the numerator is typically 10^3 smaller than the denominator. Therefore d_0 in the denominator can without noticeable error be replaced by $\langle d(k_i l_i m_i) \rangle$, the average value of the d-values that have been measured and thus take part in the stress determination. In fact d_0 could be replaced by any d-value as long as the thereby introduced relative systematic error in d can be neglected compared to the measurement error in $d(k_i l_i m_i)$ relative to $d(k_i l_i m_i) - d_0$. An analogous substitution takes place in the derivation of the so called $\sin^2\psi$-method, the two dimensional analogue of this method [3.4].
Consequently

$$\frac{d(k_i l_i m_i) - d_0}{d_0} \approx \frac{d(k_i l_i m_i) - d_0}{\langle d(k_i l_i m_i) \rangle} \tag{3.12}$$

For convenience we will write: $\langle d(k_i l_i m_i) \rangle = d$ and consequently, using equation 3.12, equation 3.10 can be rewritten as

$$\frac{d(k_i l_i m_i)}{d} = d_0/d + k_i^2 \varepsilon_{11} + l_i^2 \varepsilon_{22} + m_i^2 \varepsilon_{33} + \\ + 2k_i l_i \varepsilon_{12} + 2k_i m_i \varepsilon_{13} + 2l_i m_i \varepsilon_{23} \tag{3.13}$$

Suppose that at one co-ordinate in the sample n diffraction peaks were measured. This results in n equations of the type of equation 3.13. Together they form a system of equations of the form

$$\frac{1}{d}\begin{pmatrix} d(k_1 l_1 m_1) \\ d(k_2 l_2 m_2) \\ d(k_3 l_3 m_3) \\ \cdot \\ \cdot \\ \cdot \\ d(k_n l_n m_n) \end{pmatrix} = \begin{pmatrix} 1 & k_1^2 & l_1^2 & m_1^2 & k_1 l_1 & k_1 m_1 & l_1 m_1 \\ 1 & k_2^2 & l_2^2 & m_2^2 & k_2 l_2 & k_2 m_2 & l_2 m_2 \\ 1 & k_3^2 & l_3^2 & m_3^2 & k_3 l_3 & k_3 m_3 & l_3 m_3 \\ \cdot & \cdot & \cdot & \cdot & \cdot & \cdot & \cdot \\ \cdot & \cdot & \cdot & \cdot & \cdot & \cdot & \cdot \\ \cdot & \cdot & \cdot & \cdot & \cdot & \cdot & \cdot \\ 1 & k_n^2 & l_n^2 & m_n^2 & k_n l_n & k_n m_n & l_n m_n \end{pmatrix} \begin{pmatrix} d_0/d \\ \varepsilon_{11} \\ \varepsilon_{22} \\ \varepsilon_{33} \\ 2\varepsilon_{12} \\ 2\varepsilon_{13} \\ 2\varepsilon_{23} \end{pmatrix} \tag{3.14}$$

The solution of equation 3.14 should give us the elements of the strain tensor and the stress free lattice parameter. In the following section it will shown how to conduct this solution process.

3.5 STRAIN CONSTRAINTS AND SOLUTION

Equation 3.14 represents a system of n equations with a maximum of 7 unknowns which we would like to solve for. Equation 3.14 can be written as a matrix equation

$$\boldsymbol{K\varepsilon} = \boldsymbol{d} \tag{3.15}$$

In equation 3.14, $(k_i l_i m_i)$ represents a direction in the specimen co-ordinate system. Because it is a unit vector its elements should obey the following relationship

$$k_i^2 + l_i^2 + m_i^2 = 1 \tag{3.16}$$

Equation 3.16 makes it impossible to solve equation 3.14 when d_0/d, ε_{11}, ε_{22}, ε_{33} are unknown at the same time. This can be understood as follows. The design matrix $\boldsymbol{K}$ of equation 3.15 can always be shuffled such that one column becomes the null vector. (*i.e.* by subtracting the sum of columns 2, 3 and 4 from column 1, see also equation 3.14). This phenomenon, known by the term 'column degeneracy' prohibits the solution of the related system of linear equations. This is the mathematical formulation of the impossibility to detect a hydrostatic component p_{ij}

$$p_{ij} = \begin{pmatrix} p & 0 & 0 \\ & p & 0 \\ & & p \end{pmatrix} \tag{3.17}$$

One can never differentiate between the presence of a hydrostatic component in the stress state and a lower or higher value for d_0.
A solution to the problem of solving equation 3.14 is, that in addition to this system, constraint equations have to be given. The most trivial constraint evidently is: knowing d_0/d. In that case, equation 3.14 reduces to n equations with 6 unknowns, which has a unique solution for $n \geq 6$ (when $n > 6$ this means a solution in a least squares sense).

Another type of constraints concerns relations between the strain tensor components *e.g.*

plane strain : $\varepsilon_{33} = 0$
uniaxial stress : $\varepsilon_{22} = -\nu\varepsilon_{11}$; $\varepsilon_{33} = -\nu\varepsilon_{11}$

A residual stress measurement should be planned such that the number of equations plus the number of constraints is larger than the number of unknowns (here: always 7). Only then it is possible to solve the system in a least squares sense, provided that no column degeneracies are introduced by the form of $\boldsymbol{K}$ which is after all related to the way the experiments are planned.

The constraint equations could be simply added to the system of equations defined by equation 3.14. When this completed system is solved

in least squares sense, the constraints will not exactly be obeyed, because a constraint gets the same weight as a measurement equation. A solution to this numerical problem is to give the constraint equations a weight many times larger than the measurement equations. This method has an important disadvantage: an error analysis procedure is no longer possible after solving the completed equation 3.14. A more elegant way of incorporating the constraints is to write them in a matrix form

$$\boldsymbol{\varepsilon} = \boldsymbol{A}\boldsymbol{\varepsilon} + \boldsymbol{\varepsilon}_0 \tag{3.18}$$

$\boldsymbol{A}$ is a square (7 × 7) matrix that is usually singular. We will call $\boldsymbol{A}$ the strain constraints matrix. $\boldsymbol{\varepsilon}_0$ is called the strain constraints vector. In case of a uniaxial stress, equation 3.18 becomes

$$\begin{pmatrix} d_0/d \\ \varepsilon_{11} \\ \varepsilon_{22} \\ \varepsilon_{33} \\ 2\varepsilon_{12} \\ 2\varepsilon_{13} \\ 2\varepsilon_{23} \end{pmatrix} = \begin{pmatrix} 1 & 0 & 0 & 0 & 0 & 0 & 0 \\ 0 & 1 & 0 & 0 & 0 & 0 & 0 \\ 0 & -\nu & 0 & 0 & 0 & 0 & 0 \\ 0 & -\nu & 0 & 0 & 0 & 0 & 0 \\ 0 & 0 & 0 & 0 & 0 & 0 & 0 \\ 0 & 0 & 0 & 0 & 0 & 0 & 0 \\ 0 & 0 & 0 & 0 & 0 & 0 & 0 \end{pmatrix} \begin{pmatrix} d_0/d \\ \varepsilon_{11} \\ \varepsilon_{22} \\ \varepsilon_{33} \\ 2\varepsilon_{12} \\ 2\varepsilon_{13} \\ 2\varepsilon_{23} \end{pmatrix} + \begin{pmatrix} 0 \\ 0 \\ 0 \\ 0 \\ 0 \\ 0 \\ 0 \end{pmatrix} \tag{3.19}$$

Another example is that d_0 is known in the sense that $d_0/d = \kappa$

$$\begin{pmatrix} d_0/d \\ \varepsilon_{11} \\ \varepsilon_{22} \\ \varepsilon_{33} \\ 2\varepsilon_{12} \\ 2\varepsilon_{13} \\ 2\varepsilon_{23} \end{pmatrix} = \begin{pmatrix} 0 & 0 & 0 & 0 & 0 & 0 & 0 \\ 0 & 1 & 0 & 0 & 0 & 0 & 0 \\ 0 & 0 & 1 & 0 & 0 & 0 & 0 \\ 0 & 0 & 0 & 1 & 0 & 0 & 0 \\ 0 & 0 & 0 & 0 & 1 & 0 & 0 \\ 0 & 0 & 0 & 0 & 0 & 1 & 0 \\ 0 & 0 & 0 & 0 & 0 & 0 & 1 \end{pmatrix} \begin{pmatrix} d_0/d \\ \varepsilon_{11} \\ \varepsilon_{22} \\ \varepsilon_{33} \\ 2\varepsilon_{12} \\ 2\varepsilon_{13} \\ 2\varepsilon_{23} \end{pmatrix} + \begin{pmatrix} \kappa \\ 0 \\ 0 \\ 0 \\ 0 \\ 0 \\ 0 \end{pmatrix} \tag{3.20}$$

Now let equation 3.18 represent m independent constraints, then A is a (7×7) matrix of rank $(7 - \mathrm{m})$. A is thus singular for $m > 0$.

Now, equation 3.18 can be substituted in equation 3.15

$$\boldsymbol{K}(\boldsymbol{A\varepsilon} + \boldsymbol{\varepsilon}_0) = \boldsymbol{d} \tag{3.21}$$

which can be rewritten as

$$\boldsymbol{KA\varepsilon} = \boldsymbol{d} - \boldsymbol{K\varepsilon}_0 \tag{3.22}$$

Each constraint corresponds to a null vector column in A, so equation 3.22 is in fact the representation of n equations with $7 - m$ unknowns.

Equation 3.22 can be solved using a numerical method called Singular Value Decomposition (SVD) [3.5][3.6]. SVD solves equation 3.22 for any value of n as long as $n \geq 7 - m$. The method is also useful to investigate the equation as SVD can detect column degeneracies in $\boldsymbol{KA}$, the design matrix of the system. This may be of help when planning experiments on a material that contains a stress state for which the constraints are not very transparent from a mathematical point of view. Equation 3.22 has an exact solution for $n = 7 - m$. For $n > 7 - m$, SVD solves in a least squares sense. Altogether, equation 3.22 has a unique solution provided the matrix $\boldsymbol{KA}$ has no column degeneracies.

From the solution of equation 3.22 the complete strain tensor in Voigt notation is obtained using equation 3.18. When the strain tensor is written in the form of equation 3.1, it can be diagonalized. This process yields the principal strain tensor according to equation 3.2 and a cosine matrix that gives the orientation of the principal strain tensor with respect to the sample co-ordinate system. Mathematically, the diagonalization can be regarded as an eigenvalue problem. The elements of the diagonalized matrix are the eigenvalues, while the eigenvectors give the principal co-ordinate system. An adequate numerical method for this problem is the Jacobi transformation method that is both fast and accurate [3.7].

When the strain tensor has been solved, the stress tensor σ_{ij} can be derived from it using Hooke's Law (equation 3.8).

3.6 STRESS CONSTRAINTS

In the previous section it is assumed that the strain constraints vector and matrix are known. Constructing them when the strain constraints are known is rather straightforward. In most practical cases, however, the mechanical constraints are known in terms of stress rather than in terms of strain. The subject of this section is to transform constraints known in terms of stress into terms of strain.
Consider

$$\boldsymbol{\sigma} = \boldsymbol{B\sigma} + \boldsymbol{\sigma}_0 \tag{3.23}$$

For obvious reasons, $\boldsymbol{B}$ and $\boldsymbol{\sigma}_0$ are called the stress constraints matrix and vector respectively. Because the relation between stress and strain is known, it is possible to express stress constraints in terms of strain constraints. In practice this means a translation of 3.23 in terms of equation 3.18, according to the following relationships

$$\boldsymbol{\varepsilon} = \boldsymbol{S\sigma} \tag{3.24}$$

and

$$\boldsymbol{\sigma} = \boldsymbol{C\varepsilon} \tag{3.25}$$

In equations 3.24 and 3.25, $\boldsymbol{S}$ and $\boldsymbol{C}$ are augmented by a 0^{th} row and column of zero's and a diagonal element equal to 1 in order to take care of the 7^{th} unknown, d_0/d. Combination of equations 3.23 to 3.25 yields

$$\boldsymbol{\varepsilon} = \boldsymbol{SBC\varepsilon} + \boldsymbol{S\sigma}_0 \tag{3.26}$$

Because equation 3.26 has to be valid for all $\boldsymbol{\sigma}$ and $\boldsymbol{\varepsilon}$ it is possible to identify

$$\boldsymbol{A} = \boldsymbol{SBC} \tag{3.27}$$

and

$$\boldsymbol{\varepsilon}_0 = \boldsymbol{S\sigma}_0 \tag{3.28}$$

The thus found $\boldsymbol{A}$ is not unique. Suppose $\boldsymbol{B}$ contains the following relationships

$$\begin{aligned} \sigma_1 &= \sigma_1 \\ \sigma_2 &= \sigma_1 \\ \sigma_3 &= \sigma_1 \end{aligned} \tag{3.29}$$

Equation 3.29 could also be written as

$$\begin{aligned} \sigma_1 &= \sigma_2 \\ \sigma_2 &= \sigma_2 \\ \sigma_3 &= \sigma_2 \end{aligned} \tag{3.30}$$

or as

$$\begin{aligned} \sigma_1 &= \tfrac{1}{2}(\sigma_1 + \sigma_2) \\ \sigma_2 &= \tfrac{1}{2}(\sigma_1 + \sigma_2) \\ \sigma_3 &= \tfrac{1}{2}(\sigma_1 + \sigma_2) \end{aligned} \tag{3.31}$$

Generally, equation 3.27 leads to a strain constraints matrix of a non trivial form. But, as the constraints may be expressed in infinitely many ways, one apparently has the right to shuffle $\boldsymbol{A}$ into any form without losing information about the constraints.

In order to prescribe a recipe for a shuffling process to be applied, first a desired final form of the strain constraints matrix should be defined. This will be the next step to undertake.

It is evident that each given stress constraint can be translated to one strain constraint. (The number of unknowns in terms of stress will be equal to the number of unknowns in terms of strain). From the stress constraints matrix $\boldsymbol{B}$ it can be seen which stress components are known (or otherwise: which stress components can be expressed as a linear combination of other stress components). The column in $\boldsymbol{B}$, corresponding to such a known component contains only zero's *i.e.* equals a null-vector. The shuffling process should be such that columns in $\boldsymbol{A}$, corresponding to null-vector columns in $\boldsymbol{B}$, are also made equal to null vectors.

Diagonal elements in $\boldsymbol{B}$ that correspond to unknown stress components (or stress components that cannot be expressed as a linear combination of other stress components) are – in $\boldsymbol{B}$ – equal to 1. The

shuffling procedure to be defined should be such that corresponding diagonal elements in $\boldsymbol{A}$ are also equal to 1.

The proposed shuffling process will be illustrated by the example of a rotation symmetrical plane stress

$$\begin{aligned} \sigma_{22} &= \sigma_{11} \\ \sigma_{33} &= 0 \\ \sigma_{12} &= \sigma_{13} = \sigma_{23} = 0 \end{aligned} \tag{3.32}$$

So the $\boldsymbol{B}$-matrix takes the following form

$$\boldsymbol{B} = \begin{pmatrix} 1 & 0 & 0 & 0 & 0 & 0 & 0 \\ 0 & 1 & 0 & 0 & 0 & 0 & 0 \\ 0 & 1 & 0 & 0 & 0 & 0 & 0 \\ 0 & 0 & 0 & 0 & 0 & 0 & 0 \\ 0 & 0 & 0 & 0 & 0 & 0 & 0 \\ 0 & 0 & 0 & 0 & 0 & 0 & 0 \\ 0 & 0 & 0 & 0 & 0 & 0 & 0 \end{pmatrix} \tag{3.33}$$

For this example we choose matrices $\boldsymbol{C}$ and $\boldsymbol{S}$ (from the equations 3.24 and 3.25) belonging to isotropic cubic materials. So the stiffness matrix becomes

$$\boldsymbol{C} = \begin{pmatrix} 1 & 0 & 0 & 0 & 0 & 0 & 0 \\ 0 & C_{11} & C_{12} & C_{12} & 0 & 0 & 0 \\ 0 & C_{12} & C_{11} & C_{12} & 0 & 0 & 0 \\ 0 & C_{12} & C_{12} & C_{11} & 0 & 0 & 0 \\ 0 & 0 & 0 & 0 & C_{44} & 0 & 0 \\ 0 & 0 & 0 & 0 & 0 & C_{44} & 0 \\ 0 & 0 & 0 & 0 & 0 & 0 & C_{44} \end{pmatrix} \tag{3.34}$$

where

$$C_{11} = \frac{E(1-\nu)}{(1+\nu)(1-2\nu)}$$
$$C_{12} = \frac{E\nu}{(1+\nu)(1-2\nu)} \qquad (3.35)$$
$$C_{44} = \frac{E}{2(1+\nu)}$$

and the compliance matrix becomes

$$\boldsymbol{S} = \begin{pmatrix} 1 & 0 & 0 & 0 & 0 & 0 & 0 \\ 0 & S_{11} & S_{12} & S_{12} & 0 & 0 & 0 \\ 0 & S_{12} & S_{11} & S_{12} & 0 & 0 & 0 \\ 0 & S_{12} & S_{12} & S_{11} & 0 & 0 & 0 \\ 0 & 0 & 0 & 0 & S_{44} & 0 & 0 \\ 0 & 0 & 0 & 0 & 0 & S_{44} & 0 \\ 0 & 0 & 0 & 0 & 0 & 0 & S_{44} \end{pmatrix} \qquad (3.36)$$

where

$$S_{11} = \frac{1}{E}$$
$$S_{12} = \frac{-\nu}{E} \qquad (3.37)$$
$$S_{44} = \frac{2(1+\nu)}{E}$$

From equation 3.33 to 3.37 is easily seen that

$$\boldsymbol{A} = \boldsymbol{SBC} =$$
$$= \frac{1}{(1+\nu)(1-2\nu)} \begin{pmatrix} 1 & 0 & 0 & 0 & 0 & 0 & 0 \\ 0 & 1-2\nu+\nu^2 & \nu(1-\nu) & \nu(1-\nu) & 0 & 0 & 0 \\ 0 & 1-2\nu+\nu^2 & \nu(1-\nu) & \nu(1-\nu) & 0 & 0 & 0 \\ 0 & -2\nu(1-\nu) & -2\nu^2 & -2\nu^2 & 0 & 0 & 0 \\ 0 & 0 & 0 & 0 & 0 & 0 & 0 \\ 0 & 0 & 0 & 0 & 0 & 0 & 0 \\ 0 & 0 & 0 & 0 & 0 & 0 & 0 \end{pmatrix} \qquad (3.38)$$

We now perform the following shuffling process. The 2nd column of $\boldsymbol{A}$ (equation 3.38) is divided by $\frac{1-\nu}{(1+\nu)(1-2\nu)}$ and both the 3rd and 4th columns are divided by $\frac{\nu}{(1+\nu)(1-2\nu)}$. The result is that column 2, 3 and 4 become equal. At this stage two of these three columns are replaced by the difference of any of the three, which is, as all three are currently equal: the null-vector. After these shuffling operations only one of the columns remains non-zero. So the operation finally results in

$$\boldsymbol{A} = \begin{pmatrix} 1 & 0 & 0 & 0 & 0 & 0 & 0 \\ 0 & 1 & 0 & 0 & 0 & 0 & 0 \\ 0 & 1 & 0 & 0 & 0 & 0 & 0 \\ 0 & \frac{-2\nu}{(1-\nu)} & 0 & 0 & 0 & 0 & 0 \\ 0 & 0 & 0 & 0 & 0 & 0 & 0 \\ 0 & 0 & 0 & 0 & 0 & 0 & 0 \\ 0 & 0 & 0 & 0 & 0 & 0 & 0 \end{pmatrix} \qquad (3.39)$$

which is the strain constraint matrix for the set of stress constraints belonging to this problem.

3.7 ERROR ANALYSIS

The experimentally determined d-values contain errors which can be characterized by standard deviations Δd. At this point we want to establish the effect of the standard deviations on the solution of

$$\boldsymbol{KA\varepsilon} = \boldsymbol{d} - \boldsymbol{K\varepsilon}_0 \tag{3.22}$$

which was derived in the foregoing sections. Depending on the form of equation 3.22 these errors will have an effect on the final solution vector $\boldsymbol{\varepsilon}$. In order to perform an error analysis that makes sense, the different equations of 3.22 should be weighted according to the individual standard deviations Δd_i. In this section we will show how this weighting process is incorporated in the theory presented so far.

In equation 3.22, $\boldsymbol{KA}$ is a $\{n \times (7 - m)\}$ matrix; $\boldsymbol{\varepsilon}$ has $(7 - m)$ elements; $\boldsymbol{d} - \boldsymbol{K\varepsilon}_0$ has n elements.

Mathematically, the weighting is performed by left-multiplying both sides of equation 3.22 by a weight matrix $\boldsymbol{G}$. This results in

$$\boldsymbol{GKA\varepsilon} = \boldsymbol{G}(\boldsymbol{d} - \boldsymbol{K\varepsilon}_0) \tag{3.40}$$

Assuming the individual errors Δd_i are mutually independent (which will be the case for errors based on counting statistics), the $\boldsymbol{G}$ matrix is a diagonal matrix with elements

$$g_{ii} = \frac{d}{\Delta d_i} \tag{3.41}$$

The proposed least squares method of SVD will now have to minimize

$$r^2 = \left\| \boldsymbol{G}(\boldsymbol{d} - \boldsymbol{K\varepsilon}_0) - \boldsymbol{GKA\varepsilon} \right\|^2 \tag{3.42}$$

instead of

$$r^2 = \left\| (\boldsymbol{d} - \boldsymbol{K\varepsilon}_0) - \boldsymbol{KA\varepsilon} \right\|^2 \tag{3.43}$$

Using the now defined matrix $\boldsymbol{G}$, consider the following matrix product

$$\boldsymbol{V} = \left\{ (\boldsymbol{GKA})^T \cdot \boldsymbol{GKA} \right\}^{-1} \tag{3.44}$$

Equation 3.44 is called the unscaled covariance matrix for the solution of equation 3.40. $\boldsymbol{V}$ is scaled with

$$\chi^2 = \frac{\left\| \boldsymbol{GKA\varepsilon} - \boldsymbol{G}(\boldsymbol{d} - \boldsymbol{K\varepsilon}_0) \right\|^2}{n - (7 - m)} \tag{3.45}$$

The elements of $\chi^2 \boldsymbol{V}$ have a statistic interpretation. The square roots of the diagonal elements are an estimate of the standard deviations $\Delta\varepsilon_i$ in the corresponding elements of the solution vector $\boldsymbol{\varepsilon}$.

The vector $\Delta\boldsymbol{\varepsilon}$ only represents the errors in the unknown strains. The uncertainty in the strain elements that were hidden by the strain constraints can be obtained by applying a standard error transfer procedure using the strain constraint matrix $\boldsymbol{A}$

$$\Delta\varepsilon_i = \sqrt{\sum_{j=1}^{7} (a_{ij}\Delta\varepsilon_j)^2} \tag{3.46}$$

In equation 3.46 a_{ij} are the elements of $\boldsymbol{A}$.

From equation 3.46 the uncertainty in the stress vector is derived by applying

$$\Delta\sigma_i = \sqrt{\sum_{j=1}^{7} (c_{ij}\Delta\varepsilon_j)^2} \tag{3.47}$$

where c_{ij} are the elements of $\boldsymbol{C}$, the stiffness tensor in Voigt matrix notation.

REFERENCES

3.1 J.F. Nye, *Physical Properties of Crystals*, Oxford University Press, 134ff (1979).

3.2 *Ibid.*, 131ff.

3.3 *Ibid.*, 82ff.

3.4 B.D. Cullity, *Elements of X-Ray Diffraction*, Addison-Wesley, 447ff (1978).

3.5 C.L. Lawson and R.J. Hanson, *Solving Least Squares Problems*, Prentice-Hall, 107 (1974).

3.6 W.H. Press; B.P. Flannery; S.A. Teukolsky and W.T. Vetterling, *Numerical Recipes*, Cambridge University Press, 52ff (1986).

3.7 *Ibid.*, 342ff.

4

Development of the Stress Measurement Set-up

4.1 INTRODUCTION

In the preceding chapters, the theory of stress measurements by means of neutron diffraction has been presented. Much attention has been paid to how stresses can be obtained from diffraction data. Until now, little has been said about the actual instrument that is used to perform these experiments.

The instrument that has been used for the present measurements is a temporarily reconstructed neutron powder diffractometer. To be more specific, the powder diffractometer situated at the horizontal beam port no.5 (HB5) of the High Flux Reactor (HFR) at Petten, the Netherlands. This instrument has been used for a long time to obtain powder diffraction patterns of various solid state materials. From these powder diagrams, the crystallographic structure of a material is determined using advanced refinement techniques [4.1].

The crystallographic structure of a material of which one likes to obtain the stress state will usually be known, so the main interest will be emphasized on the precise determination of lattice spacings at a well defined spot in a specimen under investigation.

The contents of this chapter are focused on the constructive parts that have to be connected to the powder diffractometer in order to transform the latter into a stress measurement facility. This is followed by the description of the way these parts should be aligned in the beam geometry of the original diffractometer. Experience has shown, that the alignment quality of the instrument is the major factor in successfully performing stress measurements. Besides practical information about the

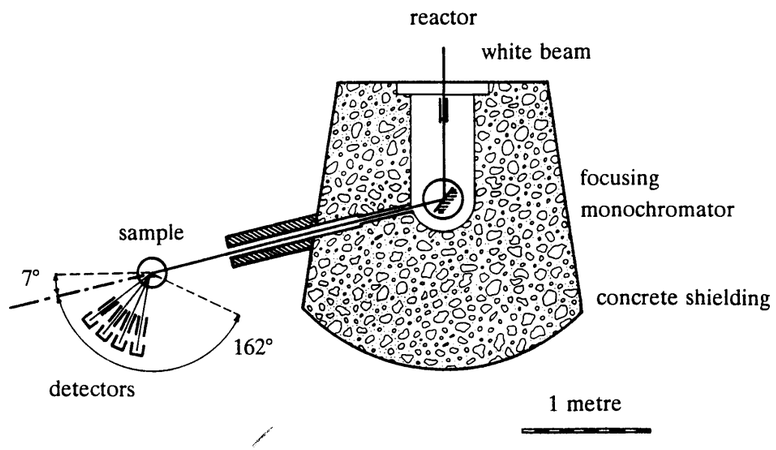

Fig. 4.1 Principle of the powder diffractometer at HB5 in the HFR at Petten.

alignment procedures, a mathematical background for the alignment procedures will also be presented.

4.2 THE POWDER DIFFRACTOMETER

Before going into the details of the alignment procedure, we will give a brief outline of the basic set-up, which is a horizontal neutron powder-diffractometer. An schematic overview of this instrument is given in figure 4.1.

4.2.1 Beam handling

A polychromatic (white) beam leaves the reactor core through a beam tube. The dimensions of the tube are chosen such that the divergence of the beam that leaves the tube is about 1°. The spectrum of the white beam is of a Maxwellian shape, which is determined by the operating temperature of the reactor [4.2]. The white beam passes a Soller collimator, built from a stack of neutron absorbing vertical lamellae. The

horizontal divergence of the beam after collimation is 0.5°. This Soller collimator can be replaced by a 0.17° collimator or by no collimator at all by a remote control collimator exchange installation. All our experiments have been performed using a 0.5° collimator. The influence of the application of different types of collimation on the resolution of a powder diffractometer is given in a standard work by Cagliotti *et.al.*[4.3].

The collimated white beam impinges on the (111)-planes of a set of copper single crystals, which is called the monochromator. The angle of incidence is 38° with respect to the monochromator surface. The take-off angle is again 38°. The wavelength of the obtained monochromatic beam can be obtained from Bragg's law

$$2d_{hkl}\sin\theta = n\lambda \tag{4.1}$$

where

d_{hkl}: lattice spacing of the reflecting planes (hkl);
θ: diffraction angle;
n: integer number, indicating the order of the reflection;
λ: wavelength of the diffracted radiation.

As the lattice distance for (111)-planes in Cu is $d_{111} = 0.2087$ nm, it is seen from equation 4.1, that the first order ($n = 1$) wavelength of the monochromatic radiation is $\lambda = 0.257$ nm.

The monochromator consists of a stack of 9 single crystal Cu-slabs. The slabs can be individually rotated around a horizontal axis lying in the crystal surface, which is parallel to the (111)-planes. Using this rotation possibility, the monochromator can be made to act as a curved mirror for neutrons that leave the reactor vessel. The radius of curvature, necessary for imaging the reactor vessel opening in the beam tube at the centre of the diffractometer, is calculated from the geometrical parameters that define the system. The equation that describes this radius of curvature is adopted from elementary optics. We will not derive it here but merely give it as

$$\frac{1}{s_0} + \frac{1}{s_1} = \frac{2\sin\theta_m}{R} \tag{4.2}$$

where

s_0: distance from the reactor vessel to the monochromator;
s_1: distance from the monochromator to the diffractometer centre;
θ_m: diffraction angle for the monochromator;
R: radius of curvature of the set of monochromator slabs.

The purpose of the focusing action of the monochromator is to increase the neutron intensity at the site of the specimen.

After monochromatization, the beam is aimed towards the centre of the diffractometer, where the sample is mounted. The sample holder is connected to a table with a single rotation possibility with characteristic angle ω. Around the sample a set of 4 neutron counters of the ^{3}He type can be rotated. The axis of rotation coincides with the ω-axis. The counter position is called 2φ. The use of 4 counters instead of one reduces the total time necessary for measuring a complete powder diagram.

On its way from the reactor vessel to the sample, the neutron beam encounters three pyrolytic graphite filters. Their purpose is to selectively absorb neutrons, that have a wavelength of anything shorter than 0.22 nm [4.4], thus suppressing the neutron beam diffraction components of higher order (n = 2, 3, *etc.* in equation 4.1).

4.2.2 Operation

The operation of the instrument is fully computerized. The scan parameters like scan range, step size and counting time are defined by the experimentalist and subsequently a dedicated computer performs the experiment.

An important feature of the set-up is the use of a neutron monitor counter situated in the primary beam. At the cost of a small fraction of primary neutrons, the measurement computer determines the integral amount of incoming neutrons. After the detection of a predetermined amount of neutrons in the monitor counter, the measurement continues at the next counting position. The advantage of this approach is that the power level of the neutron source – the reactor – does not influence the measurement results.

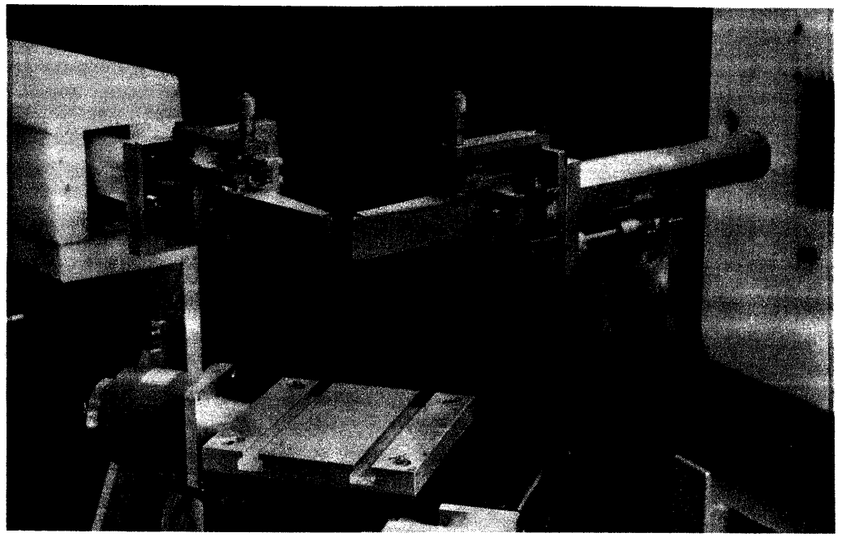

Fig. 4.2 Photograph showing the apertures that determine the size of the sampling volume in the specimen by limiting the size of the primary and diffracted beams. The size of the apertures can be adjusted by micrometre screws on top of the aperture assemblies.

4.3 ADAPTATIONS FOR STRESS MEASUREMENTS

The diffractometer described in the previous paragraph requires some reconstruction in order to serve as a stress measurement facility. The two major adaptations are the installation of sample volume defining apertures and a specimen co-ordinate table. Both will be treated in this section.

4.3.1 The beam apertures

In powder mode, the size of both the relevant part of the primary beam and the diffracted beam is determined by the size of the sample, which is fully bathed in the neutron beam. For stress measurements, the size of the inspected volume in a specimen – the sample- or gauge volume – has to be smaller than the overall specimen. The sample volume size determines the spatial resolution of a stress measurement. In order to obtain a reasonable spatial resolution, the sizes of the primary- and

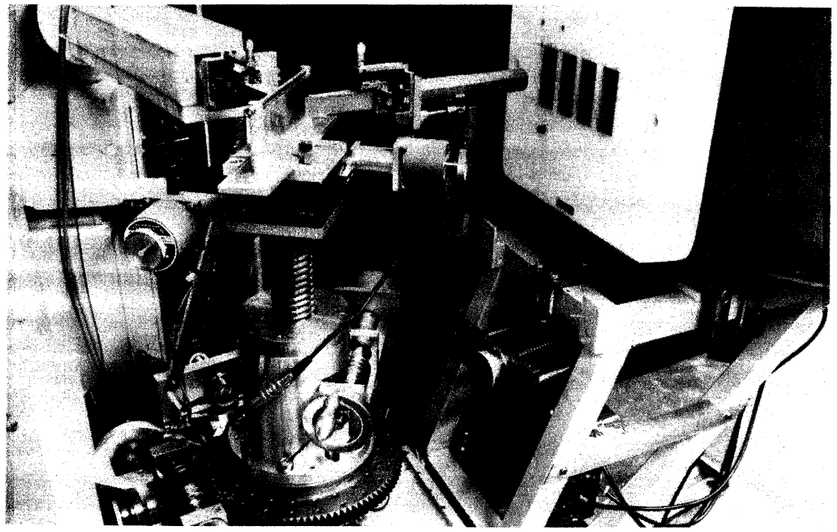

Fig. 4.3 Photograph showing an overview of the employed stress measurement set-up. Clearly visible are the *xyz* movement possibilities as well as the movable beam apertures.

diffracted beams are reduced. This is achieved by placing cadmium plated apertures in the primary and secondary beams. The apertures are shown in figure 4.2. In the present situation, the cross-section of these apertures can be adjusted between 0 mm × 5 mm and 4 mm × 25 mm. The apertures are connected to slide systems, that permit the adjustment of the aperture to specimen distance. This degree of freedom is necessary for the flexibility of the set-up, which means here, that specimens of various sizes and shapes can be investigated without major modifications of the set-up. Also the orientation of a specific specimen might influence the positions of the apertures.

The primary beam aperture moves between the monochromator and the diffractometer centre. Its slide system is connected to the base of the diffractometer frame. The secondary beam aperture is connected to the counter bracket and moves between the diffractometer centre and one of the 4 neutron detectors. The remaining 3 detectors are covered with neutron absorbing material. They are not used during stress measurements.

4.3.2 The co-ordinate table

The second major adaptation is a 3-axes specimen table. For this purpose a commercially available *xy*-translation table is connected to a vertical displacement unit. The latter is home made (see figure 4.3).

Stress measurements as a function of any of the co-ordinates *x*, *y* and *z* can now be performed by transport of the specimen, while the sample volume as defined by the intersection of the beam paths defined by the two apertures remains stationary.

4.3.3 Operation

The adaptations described above are all transporting mechanisms. All are stepper motor driven on command of the measurement computer. The second task of that computer is to read the neutron counting register.

The computer program that operates the instrument can be programmed to perform 16 different scans continuously one after another. For each of these scans, all variables can be set to any value while one of the variables – the scan parameter – is programmed to step between two extremes employing a certain step size. The scan variable can be chosen to be any motor position, except the positions of both the primary and secondary apertures. In Table 4.1 an overview is given of the movement

Table 4.1

The motor movement possibilities of the stress measurement facility situated at HB5 at the HFR in Petten. The figures given are those valid without the presence of a specimen. When a specimen is situated on the specimen table one ore more figures in the column 'range' could be erroneous.

movement	range	smallest step	encoder	scan possible
2θ	−2° - 140°	0.01°	yes	yes
ω	0° - 360°	0.01°	yes	yes
x	0 - 60 mm	0.005 mm	no	yes
y	0 - 60 mm	0.005 mm	no	yes
z	0 - 140 mm	0.0002 mm	no	yes
p	0 - 55 mm	0.04 mm	no	no
s	0 - 120 mm	0.04 mm	no	no

possibilities of the powder diffractometer in stress measurement mode. In Table 4.1 also the presence of an encoder is mentioned. An encoder is a piece of hardware that is capable of reading the position of a certain movement, independently of the command history of the movement. Using an encoder is advantageous, because the position of a motor becomes absolute rather than relative. This is useful when restarting the system after having switched off the mains supply as well as for automatic position checks during an experiment.

4.3.4 Pyrolytic graphite filters

The pyrolytic graphite filters that are used in the powder diffraction mode in order to suppress the intensity of higher order neutrons, are removed during stress measurements. The aim of this is to recollect some first order intensity and all of the higher order intensity that is otherwise removed from the beam. The higher order neutrons do not harm the experiment as they are diffracted at exactly the same scattering angle as the first order neutrons. The fact that higher order neutrons give rise to the appearance of extra peaks in the powder diagram does not harm in stress measurement mode, unless the diffraction peaks are very wide and overlap with each other. The effects of the presence of higher order wavelength components in the neutron beam on the appearance of a powder diagram is shown in figure 4.4. In this figure two powder diagrams of pure iron are given. One diagram is measured with all pyrolytic graphite filters present, while for the other one they are all absent. The intensity scale of both diagrams is scaled such that both curves correspond to the same measurement time. Consequently, the intensities are directly comparable. The major difference between the diagrams is the amount of diffraction peaks present. In the situation where no filters are employed, not only the first order reflection of $\lambda = 0.257$ nm is present, but also the second and third order reflections corresponding to wavelengths of $\lambda = 0.128$ nm and $\lambda = 0.086$ nm respectively, are present.

For crystal structures possessing a simplicity comparable to that of the b.c.c. structure of Fe, the advantage of applying no filters at all is obvious: the peak intensity of the (110) diffraction peak of Fe is improved by a factor of about 2.5 while the peak to background ratio is

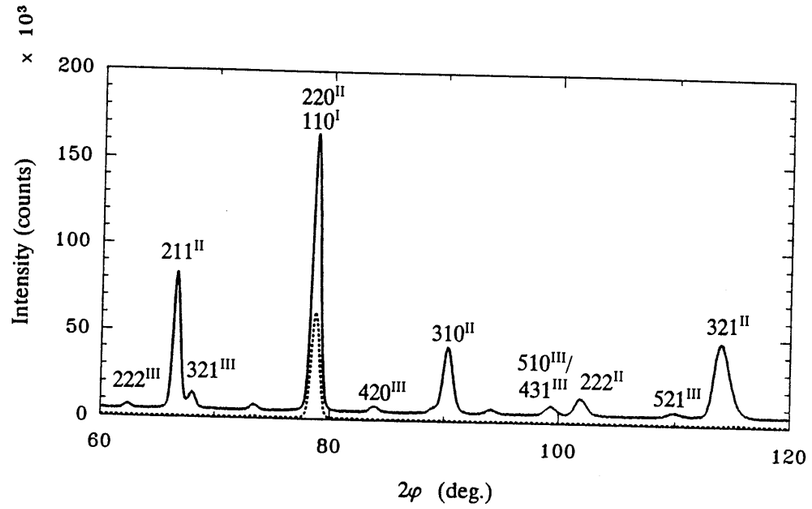

Fig. 4.4 Comparison of two powder diagrams. The solid curve has been obtained in a situation where no pyrolitic graphite filters were present in the primary beam path. The broken curve has been obtained in the situation where three graphite filters were present.

not dramatically altered (the relatively high background in the no-filter diagram of figure 4.4 is due to poor shielding; this has been improved).

4.4 ALIGNMENT OF THE DIFFRACTOMETER

The alignment requirements for the diffractometer and specimen during stress measurements are more strict than for powder measurements. The first reason for this is that the characteristic dimensions of the sample volume, defined in a specimen, are small compared to a specimen that is employed in powder diffraction. Secondly, in order to perform stress measurements as a function of any co-ordinate, the position and orientation of the sample region in the specimen geometry should be known. During the service of the stress measurement set-up, a sequence of procedures has been developed that has proved to yield an adequately aligned instrument. These procedures will be treated in this section. The alignment requirements are the following.

1. The centre line of the primary beam should point within 0.02 mm to the centre of the diffractometer. This should be the case regardless of the position of the primary beam aperture, which means that the primary beam aperture sliding system should have its sliding direction oriented parallel to the direction of the primary beam.
2. The centre line of the diffracted beam should contain the centre of the diffractometer within 0.02 mm and the sliding direction of the diffracted beam aperture should be along an angle 2φ with the primary beam (2φ is determined by the Soller slit that is situated directly in front of the detector).
3. The co-ordinates x and y at which the specimen surface coincides with the central axis of the diffractometer should be known within 0.02 mm.
4. The direction of the tangent to the (curved) specimen surface with respect to direction of the direct beam should be known. The reason is that the angle ψ, necessary for the definition of the scattering vector $\boldsymbol{q}$ in the sample axis system, should be known in order to solve for the stress tensor. The required precision is 0.01°.

In order to achieve adequate alignment, *i.e.* satisfying the above stated conditions, a series of test experiments has been developed. These procedures will be treated in order of appearance in the alignment procedure.

4.4.1 Levelling the diffractometer.

For the demanded accuracy in the alignment, a horizontal placement of the diffractometer is of importance. A very consistent horizontal reference plane is the plane given by a spirit level, which is used to level the diffractometer and all the instruments attached to it. The accuracy of the employed spirit level is 0.1 mm/m. Adjustment screws fixed to the frame of the diffractometer help to achieve this levelling.

4.4.2 The central axis of the diffractometer

The location of the central axis of the diffractometer plays an important role in the alignment. So after levelling, the second step in the alignment procedure is to find it. For this purpose a special tool has been manufactured: a precision cylinder, which can be mounted on the specimen table. The cylinder ($\varnothing$ = 20 mm) is made with such close tolerances that the axis of the cylinder is exactly perpendicular to the mounting plane. On top of the cylinder an exactly co-axial steel pin ($\varnothing$ = 1 mm) can be attached. Using the ω-motor, the cylinder and pin are rotated around the central axis. A dial gauge, connected to a fixed point somewhere on the diffractometer frame, is used to monitor the position of the circumference of the cylinder. By rotating ω and using both the x and y motors, the cylinder is translated such that the dial gauge indicator does not move more than 0.01 mm during one complete ω-revolution of the cylinder. The axis of the concentric pin placed on top of the cylinder will now be the physical central axis of the diffractometer.

Both the primary and secondary aperture can now be moved such that they point exactly towards the central axis. The establishment of electrical contact between the aperture sideplates and the steel pin is used as an aid to find the correct aperture location. In this way, one of the points that determine the directions of both aperture sliding systems is physically determined. The exact orientation of the slides (*i.e.* determining a second point along the correct sliding direction) will be obtained later in the alignment procedure. First, the direction of the primary neutron beam should be established.

4.4.3 The direct beam position.

In the not yet aligned condition, the position of the neutron detector is relative to the zero position of the encoder that reads out the position of the 2φ-motor. In order to make this position physically meaningful, the position of the 2φ-motor must be known relative to the position of the primary beam. The experiment to be performed is a very simple one: a scan of the direct beam. For this scan the primary beam aperture is opened to about 1 mm and the secondary beam aperture is opened to about 5 mm. In this configuration, a 2φ-scan is performed in the vicinity of the direct beam. This will yield a more or less Gaussian shaped intensity profile as a function of 2φ. An example of a direct beam scan is

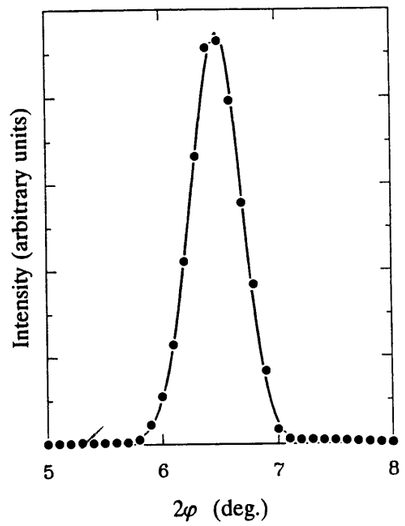

Fig. 4.5 An example of the scan around the direct beam. The solid line represents the result of a Gaussian fit to the measured data points. The direct beam has been attenuated in order to prevent an electronic overflow of the neutron counter. The attenuating material is a 3 mm thick piece of neutron absorbing material like PVC.

Table 4.2

Fit result for a Gaussian function on the data of a the direct beam scan. (*cf.* figure 4.5). For this fit $\chi^2 = 19.5$

fit parameter	value	error	unit
$2\varphi_0$	6.473	0.004	degr.
σ_{FWHM}	0.514	0.008	degr.
I_b	41.4	7.2	counts
I_0	9443	226	counts

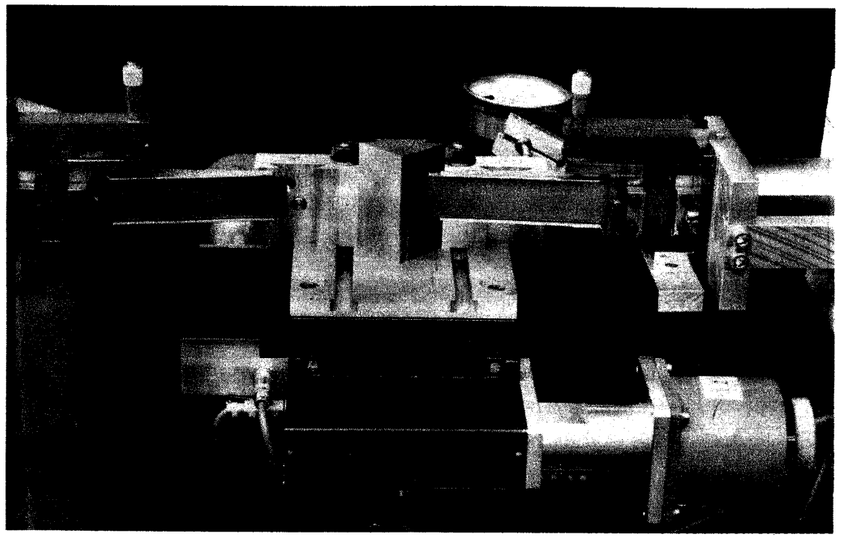

Fig. 4.6 Experimental configuration during a the single knife edge scan. The single knife assembly can be transformed into a double knife edge by placing a second cadmium wedge in the yet open sleeve on the left of the wedge shown here.

given in figure 4.5. The maximum intensity position $2\varphi_0$ is obtained by fitting a Gaussian (see Chapter 2) to the direct beam scan data. The thus found $2\varphi_0$ is the offset value for the detector angle. The Full Width at Half Maximum σ_{FWHM} of the fitted Gaussian is interpreted as the divergence of the primary beam. Typical fit results are given in Table 4.2. The $2\varphi_0$ position is needed for two reasons.

1. It makes the to be measured diffraction peaks as an absolute measure, which is needed for the precise determination of lattice plane distances.
2. The single knife edge scan and the double knife edge scan being the next alignment steps, have to be performed while the counter is situated at $2\varphi_0$.

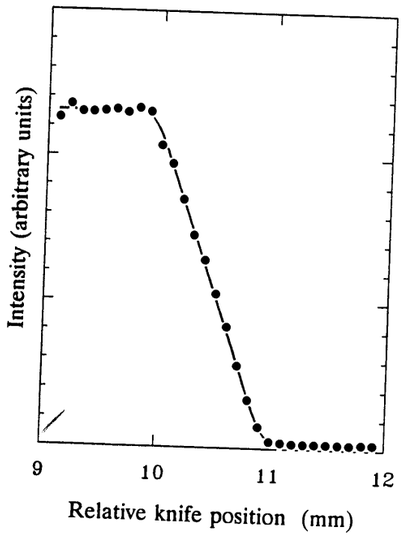

Fig. 4.7 Result of the single knife edge scan. The solid line is the final result of a Levenberg-Marquardt fitting procedure using the single knife edge function described in Appendix 1.

Table 4.3

Fit result for the function described in Appendix 1 on the data of a single knife edge scan (*cf.* figure 4.7). The distance from the primary beam aperture to the diffractometer centre d has been fixed to 30 mm. For this fit $\chi^2 = 2.2$

fit parameter	value	error	unit
x_0	10.437	0.004	mm
w	0.998	0.014	mm
α	0.456	0.049	degr.
I_b	175.5	6.5	counts
I_0	11392	143	counts

4.4.4 The single knife edge scan

This part of the alignment is meant to obtain the first out of two points that define the direction of the neutron beam.

The counter is positioned at the direct beam position $2\varphi_0$. On the specimen table a device called the single knife edge is mounted. The single knife edge is a brass wedge covered with cadmium (a neutron absorbing material) which is connected to a holding piece as is shown in figure 4.6. The angle ω is chosen such that one of the motors x or y transports the knife more or less perpendicularly to the primary beam. In this configuration, the relative position of the knife (*e.g.* x) is used as a variable in a scan. This scan gives the direct beam intensity, as a function of the relative position of the knife edge while it is step by step covering the primary beam (see figure 4.7). The function that is given in Appendix 1 describes this process. When this function is used as the model function in a Levenberg-Marquardt fitting procedure [4.5], the position x_0 where the single knife edge coincides with the central line of the primary beam is obtained. A typical result of this fitting procedure is given in Table 4.3 which belongs to the data of figure 4.7.

Now one point of the line that defines the direction of the primary beam is obtained. At this position, the double knife edge scan which will give the second point of this line, will be performed.

4.4.5 The double knife edge scan

Next to the single knife edge, a second sleeve is present in the knife holder. In this sleeve a second – identical – knife can be mounted. The construction of the knives and the holder is such that the connection line between the two knife edges and the backside of the knife holder is parallel. The co-ordinate parallel to the beam direction will be chosen such that the point between the two knives will approximately coincide with the central axis. At this point a ω-scan is carried out, which starts in the situation that one of the knives is completely covering the primary beam. The scan ends where the other knife is fully covering the beam. An example is given in figure 4.8. The intensity maximum that exists between these two extremes can be found by using the fitting function that is described in Appendix 2 as the model in a Levenberg-Marquardt fitting process [4.5]. Typical results of this procedure are given in Table 4.4.

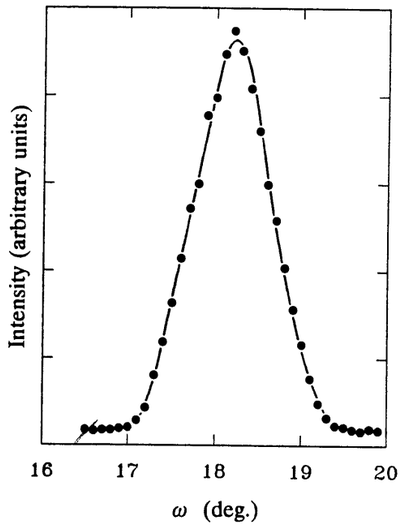

Fig. 4.8 Result of the double knife edge scan. The solid line is the result of the Levenberg Marquardt fitting procedure of the function that is described in Appendix 2.

Table 4.4

Fit result for the function given in Appendix 2 on the data of a the double knife edge scan. (*cf.* figure 4.8). The distance of the primary aperture to the centre of the diffractometer d is fixed to 35 mm, the distance between the knives l is fixed to 50 mm and the primary beam divergence α is fixed to 0.5 mm. For this fit $\chi^2 = 2.6$.

fit parameter	value	error	unit
ω_0	18.275	0.010	degr.
w	0.748	0.006	mm
Δl	-5.3	0.2	mm
I_b	178.7	6.1	counts
I_0	13836	264	counts

One of the results of the fitting procedure is ω_0, the ω-value that corresponds to the situation that the two knife edges are in line with the primary beam, so that the back plane of the knife holder is parallel to the direction of the primary beam. With the specimen table at ω_0, a steel ruler is connected to the back side of the knife holder. Using a dial gauge connected to one of the moving parts of the primary aperture, the ruler is used as a physical reference to the beam direction. Adjustment bolts on the primary aperture assembly serve to adjust the slide system in an orientation parallel to the primary beam.

In order to adjust the secondary aperture sliding system, the neutron counter is moved to the angle where it is most frequently used during stress measurements: $2\varphi = 90°$ and the specimen table is rotated towards $\omega_0 + 90°$. In this configuration the dial gauge is connected to one of the moving parts of the secondary aperture system, so that also this system can correctly be aligned with respect to the primary beam.

After all these steps, the instrument is in principle correctly aligned. All the alignment formulas, however, are derived assuming that the instrument is already well aligned. In practice, this is not the case, therefore we have to repeat the double knife edge scan and the following adjustments, until adjustments of the aperture orientations are no longer necessary. Usually this can be achieved by repeating the procedure twice.

4.4.6 Checking the alignment of the system

Having performed the actions described in the foregoing sections, the diffractometer should be well aligned. This should, however, be checked before starting any measurements.

Up to this stage of the alignment sequence, no diffraction has been used to perform any alignment action. In this section a method will be treated that uses diffraction as the main tool to determine the state of alignment of the diffractometer. For this purpose a special test specimen has been manufactured. It consists of a rectangular box made of thin (0.1 mm thick) vanadium foil. The dimensions of the box are 200 mm × 50 mm × 10 mm. The box is filled with iron powder *p.a.* and closed with epoxy resin in order to prevent oxidation. This test specimen is assumed to have no crystallographic texture, meaning that the diffracted intensity from any volume in the specimen is equal in all directions given a constant primary flux of neutrons.

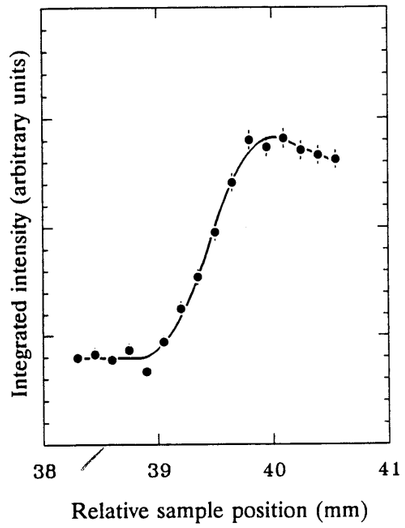

Fig. 4.9 Result for the entering curve at ψ=0°. The solid line belongs to a successful fit using the function derived in Appendix 3.

Table 4.5

Fit result for the entering curve function for ψ = 0° that was given in Appendix 3 on the data of such a scan. (*cf.* figure 4.9). The scattering angle has been set fixed to 79°. For this fit χ^2 = 1.2.

fit parameter	value	error	unit
x_0	39.46	0.03	mm
w	0.97	0.10	mm
μ	0.075	0.037	cm^{-1}
I_b	894	15	counts×degr.
I_0	927	139	counts×degr.

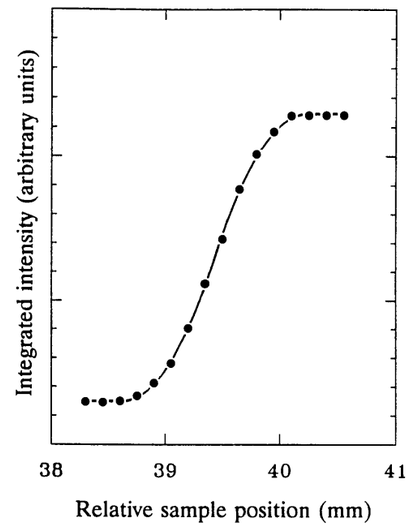

Fig. 4.10 Entering curve for ψ=90°. The solid line belongs to the fit result using the equation derived in Appendix 3.

Table 4.6

Fit result for the entering curve function for ψ = 90° that was given in Appendix 3 on the data of such a scan. (*cf.* figure 4.10). The scattering angle has been set fixed to 79°. For this fit χ^2 = 1.2.

fit parameter	value	error	unit
x_{90}	39.43	0.01	mm
w	1.03	0.02	mm
I_b	1491	22	counts×degr.
I_0	7629	219	counts×degr.

The test specimen is used in the following way. The aligned diffractometer is arranged such that the primary and diffracted beam apertures are both 1 mm open and the test specimen is situated such that the surface normal vector is parallel to the scattering vector $\boldsymbol{q}$. Using the currently available wavelength of $\lambda = 0.257$ nm, the (110)-reflection of iron can be found at $2\theta \approx 79°$. The sample volume defined by the aperture geometry is a rhombic prism with a smallest angle of 79° having a height equal to the height of the apertures. In this configuration successive 2φ-scans are performed. After each scan, the specimen is moved a small distance in the direction of its surface normal. This process proceeds from the situation where the sample volume is located completely outside the specimen to the situation where the sample volume is located completely inside the specimen. The measurement results are presented as the integrated intensity of diffraction peaks as a function of the relative specimen position. Qualitatively, the result is an s-curve starting at a background value in order to arrive at a maximum where the rhombus is completely embraced by the specimen. Beyond the maximum, the intensity drops due to the increasing total flight path through the specimen. This s-curve is called the entering curve at $\psi = 0°$.

For a complete alignment check, a second entering curve has to be measured, during which the normal to the specimen surface is perpendicular to $\boldsymbol{q}$. This results in the entering curve at $\psi = 90°$, which differs slightly from the one at $\psi = 0°$. The difference is that the intensity does not drop after the maximum level has been reached, because in this geometry the flight path through the specimen is not a function of the relative position of the sample volume in the specimen. The geometrical functions describing the entering curves at $\psi = 0°$ and $\psi = 90°$ are presented in Appendix 3. These functions are used in a Levenberg-Marquardt parameter adjustment procedure [4.5]. This yields two different results for the relative co-ordinate table position when the rhombic prism is half way in the specimen: x_0 and x_{90}. The results for both ψ-values should be within their respective experimental error limits which are calculated by the parameter adjustment procedure. If for some reason this result is not obtained, the alignment procedure has to be repeated. Examples of the ψ=0° and the ψ=90° entering curves are given in figures 4.9 and 4.10 respectively. Examples of their respective fit results are given in Tables 4.5 and 4.6.

In case the alignment check gives satisfactory results, the presence of an electrically conducting physical surface, in the form of the specimen surface, offers a possibility to make the relative scale of the specimen movement as an absolute one. For this purpose, the primary beam aperture is withdrawn and an electrically isolated needle is connected to the aperture assembly. The specimen position is set to x_0 and ω is chosen such that the specimen surface is perpendicular to the primary beam direction. When electrical contact between the needle and the test specimen surface is established by moving the needle towards the test specimen, an independent point is found which can be referred to when the test specimen is replaced by a real one. All one has to do is to remember the primary beam aperture position at which the electrical contact occurred. This procedure has proved to be accurate within 0.005 mm.

REFERENCES

4.1 G.E. Bacon, *Neutron Diffraction,* Oxford University Press, 111ff (1975).

4.2 G.E. Bacon and D.W. Thewlis, *Proc. R. Soc.*, **A196**, 50 (1949).

4.3 G. Cagliotti; A. Paoletti and F.P. Ricci, *Nucl. Instrum.*, **3**, 223 (1958).

4.4 B.O. Loopstra, *Nucl. Instr. and Meth.*, **44**, 181 (1966).

4.5 W.H. Press; B.P. Flannery; S.A. Teukolsky and W.T. Vetterling, *Numerical Recipes*, Cambridge University Press, 509ff (1986).

5
Proof of the Principle

5.1 INTRODUCTION

In the previous chapters, the theory for stress determination by means of neutron diffraction, as well as the employed instrument have been discussed. In this chapter, the instrument and the calculation methods will be used for measurements on a specimen that possesses a predictable stress state. The aim is to prove that neutron diffraction can be used to measure stresses.

As a specimen we will use a steel bar subjected to four point bending, the arrangement of which is given in figure 5.1. For our purpose, four point bending has the following advantages

1. When the applied force on the bending jig is known, the stress state in the bar can be calculated, provided that no residual stresses are present in the bar.
2. The stress state in the bar is a function of the depth below the surface, so that the use of neutrons to measure stresses in the interior of a material can be clearly demonstrated.
3. The device for stressing a bar of appreciable cross-section has dimensions that hardly exceed those of the bar itself, so little difficulties are encountered when placing the assembly on the specimen table of the neutron diffractometer.

In order to calculate the stress state from lattice plane distances, according to Chapter 3, one needs the so called Diffraction Elastic Constants (DEC's). These can be obtained from literature or from another experiment (*e.g.* x-ray diffraction stress measurements).

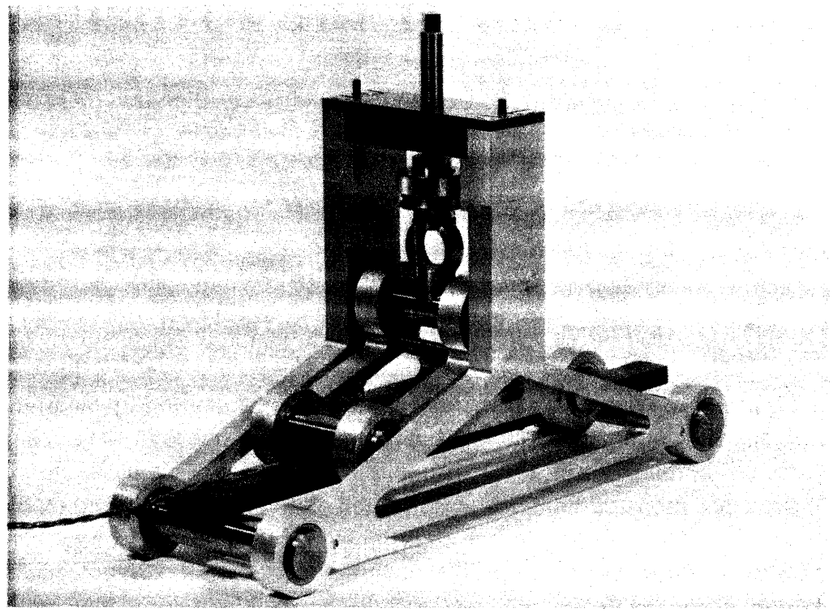

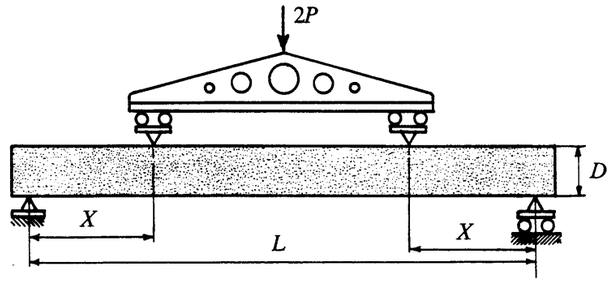

Fig. 5.1 Principle of four point bending and a photograph showing the bending device used in the present experiments. The height H of the bar is oriented perpendicular to the plane of drawing.

Using externally obtained DEC-values, the stress measurements on a four point bent bar are used as a validation experiment for the neutron method, as the measured stress should be equal to the stress predicted by calculation.

An alternative way to perform the proof of the principle is to calculate the DEC-values from neutron strain measurements and

compare them to DEC-values obtained from literature or from other experiments. The proof of the principle can be considered successful if the different techniques yield about the same values. In this chapter, measurements by means of x-ray and neutron diffraction on a steel bar subjected to pure bending will be compared. It will be shown that DEC-values obtained by any of the two methods are equal within their respective experimental error limits [5.1].

5.2 DETERMINATION OF DIFFRACTION ELASTIC CONSTANTS

In this section, first the stress state in a bar subjected to four point bending will be calculated. In the second part an equation will be derived that gives the position of a measured diffraction peak as a function of the stress in the sample volume. This function will be used for the determination of the DEC-values from neutron diffraction data as a function of the depth in a bar subjected to four point bending.

5.2.1 Four point bending

A bar subjected to four point elastic bending contains a uniaxial stress state which is a function of the depth below the surface in the direction of the applied force. This co-ordinate will be called x. The uniaxial stress is given by

$$\sigma = \frac{D - 2x}{D}\sigma_0 \tag{5.1}$$

where

D: thickness of the bar;
σ_0: uniaxial stress at the surface of the bar (*i.e* at $x = 0$).

The surface stress σ_0, is a function of the applied force $2P$ and the dimensions of the bar

$$\sigma_0 = \frac{3X}{BD^2}\,2P \tag{5.2}$$

where

B: breadth of the bar (perpendicular to the plane of drawing in figure 5.1);
X: lever length of the bending device.

The applied force $2P$ can be obtained from a calibrated load cell which is a part of the bending device which will be discussed later.

5.2.2 The working equation for DEC determination

The strain ε_ψ in a direction defined by ψ can be expressed in the orientation of the strain and the local stress, using the $\sin^2\psi$ equation for uniaxial stress. This equation can be derived from the theory presented in Chapter 3, using $\sigma_2 = \sigma_3 = 0$ and $\sigma_1 = \sigma$. Here we present the result of that derivation

$$\varepsilon_\psi = \frac{\Delta d}{d_0} = \frac{d_\psi - d_0}{d_0} \approx \frac{d_\psi - d_0}{d_\psi} = S_1\sigma + \frac{S_2}{2}\sigma\sin^2\psi \qquad (5.3)$$

where

S_1 and $S_2/2$: diffraction elastic constants;
ψ: angle between the specimen surface normal and the scattering vector $\boldsymbol{q}$ ($\boldsymbol{q}$ has the same direction as the bisector of the angle between the primary and the diffracted beams);
d_0: lattice spacing in the unstressed situation;
d_ψ: lattice spacing in the stressed situation for planes oriented according to ψ.

Using Bragg's law

$$2d\sin\theta = n\lambda \qquad (5.4)$$

where

θ: diffraction angle;
λ: wavelength of the radiation used;
n: integer that indicates the order of the reflection,

the next working equation can be derived as

$$2\theta_\psi = \frac{-360}{\pi}\frac{S_1}{\cot\theta}\sigma - \frac{360}{\pi}\frac{S_2}{2}\frac{\sin^2\psi}{\cot\theta}\sigma + 2\theta_0 \qquad (5.5)$$

In equation 5.5, $2\theta_0$ and $2\theta_\psi$ refer to diffraction angles for the specimen in unstressed and stressed conditions respectively. Differentiation of equation 5.5 with respect to σ at a constant ψ gives

$$\frac{\partial(2\theta_\psi)}{\partial\sigma} = \frac{-360}{\pi}\frac{S_1}{\cot\theta} - \frac{360}{\pi}\frac{S_2}{2}\frac{\sin^2\psi}{\cot\theta} \qquad (5.6)$$

The left side member of equation 5.6 is obtained from a least squares fit of a straight line to a $2\theta_\psi$ *vs.* σ plot (all 2θ-values in such a plot should belong to the same ψ-value). The thus obtained slopes are plotted as a function of $\sin^2\psi$. From a least squares straight line fit procedure the DEC values can be obtained (according to equation 5.6, S_1 is proportional to the 2θ-intercept and $S_2/2$ is given by the slope of the straight line).

In this approach, the determination of the diffraction elastic constants is achieved as a result of two differentiation steps, first to σ and then to $\sin^2\psi$. Mathematically speaking it does not matter which of the two differentiation steps is made first. From the measurement point of view, however, it does matter. Suppose that the systematic error in 2θ depends on the value of ψ. In Chapter 2 we have shown that, due to the combined attenuation and umbrella effects, this could very well be the case. When the first differentiation step is towards ψ, the systematic error due to the umbrella effect will be filtered out no matter how much is its magnitude (assuming it to be constant with ψ, which is the case when the aperture positions are not changed between the different applied stress levels).

5.3 SPECIMEN MATERIAL

The material to be used for the four point bending test, defines the feasibility of the proof of the principle experiment. For neutron radiation, the scattering cross-section as well as the absorption coefficient vary randomly through the periodic system of the elements.

The combined effect of diffraction and absorption (attenuation), causes a neutron beam to lose its intensity as it proceeds through the material (*cf.* Chapter 2).

Iron, the main component of low carbon steel, which we have chosen for the validation experiment combines a reasonably low attenuation with a good scattering power. Steel is still by far the most used construction material. Many residual stress problems worth investigating appear in this material. So it is a pleasant coincidence that steel has the above mentioned properties.

The beam attenuation in steel is such that when a neutron beam proceeds through it, the intensity of the beam reduces by a factor of 2 for every 7 mm. Consequently, flight paths of about 30 mm are tolerable in steel specimens. As a result, the depth to which stress measurements can be performed is limited to about 15 mm. By using a bending bar of 300 mm length, 20 mm breadth and 10 mm thickness we could measure the strains acting throughout the thickness of the bar.

5.4 BENDING DEVICE

Theoretically, pure bending is a simple deformation mode. This mode can be achieved by bending a rectangular bar in a four-point bending device. Pure bending only exists in a bar that is broad, compared to its thickness. In practice, a bar that is twice as broad as it is thick (*i.e.* $B/D \geq 2$ in terms of figure 5.1) has ideal dimensions for serving as a specimen in a pure elastic bending experiment.

In the design of the bending device of figure 5.1 we have paid special attention to the problem of friction force transfer in the length direction of the bar. In order to avoid these friction forces, the four supports of the bending device are cylindrical and mounted in needle bearings. The total rolling friction of the four bearings is such that the bar can be manually moved in its length direction even when the force on the bending jig is in the order of 1000 N.

The force that is exerted on the bending jig can be monitored by a calibrated load cell that is built in the device. The maximum load is limited to about 2000 N. This load is sufficient to bend a steel bar with cross section 10 mm × 20 mm to a surface stress level equal to the yield stress of the steel used, which is about 300 MPa.

5.5 MEASURING METHODS

The measuring methods used for both the neutron and x-ray measurements are essentially the same. The only difference is the way in which the applied stress σ is varied. For x-ray measurements, the (surface-) stress is altered by applying different loads using the bending device; for neutron measurements σ is varied by measuring at different depths, keeping the loading force on the bar constant. The applied stress can be derived from equation 5.1.

5.5.1 Neutron measurements

A measuring sample volume of 1 mm × 1 mm × 20 mm, with its centre of gravity coinciding with the diffractometer axis was defined by the cadmium plated apertures of the double slit system that was treated in Chapter 4. The Fe (110)-peaks ($2\theta \approx 79°$) from this sample volume were scanned at 19 different x-positions, ranging from $x = 1$ to $x = 9$ mm in steps of 0.5 mm in the steel bar. The surface stress σ_0 from equation 5.1 was set to 250 MPa, so that the stresses in the bar vary from −250 MPa to 250 MPa across the thickness. Using equation 5.2, the surface stress σ_0 is monitored by means of a calibrated load cell, being an integral part of the bending device.

At each location, diffraction peaks were scanned at 6 different ψ-values, corresponding to $\sin^2\psi = 0$, 0.1, 0.2, 0.8, 0.9 and 1.0. The data were corrected for the umbrella and attenuation effects as described in Chapter 2. The result of these measurements after data reduction comprises of 6 sets of 19 2θ-values.

5.5.2 X-ray measurements

The same bending device that was used for the neutron measurements described above, was mounted on the specimen table of a Siemens ω-diffractometer. The x-ray measurement site on the specimen surface, which was located in the constant bending moment region was electrochemically polished and covered with a layer of silicon powder whose lattice constant is accurately known. The (220)-reflection of the silicon powder served to determine the specimen displacement with respect to

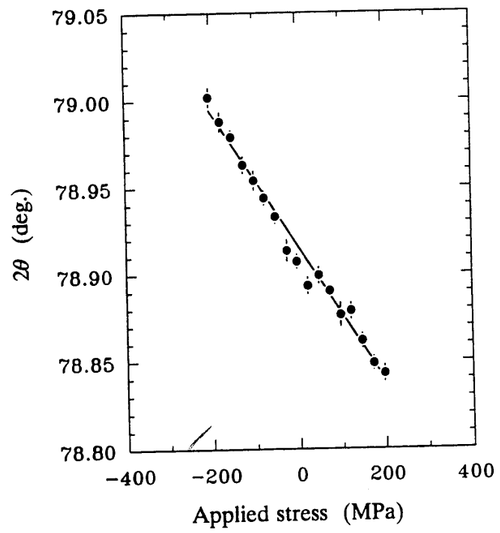

Fig. 5.2 The neutron diffraction peak position 2θ as a function of the applied stress σ at $\sin^2\psi = 1.0$. The solid line belongs to a least squares fit of a straight line to the measured data.

the diffractometer axis. The bending set-up could be moved in the direction normal to the specimen surface by means of a micrometer screw in order to correct for the specimen displacement found by the silicon experiment.

For 13 different applied surface stress levels, ranging from 20 to 260 MPa, scans of the Fe (220) peak were made. This was done at 7 different ψ-values (corresponding to $\sin^2\psi = 0$ to 0.6) using Fe-Kα radiation ($2\theta \approx 145.5°$). After each reloading a specimen displacement correction procedure was performed using the silicon reflection, as described above. The counting time was chosen such that the peak intensity was at least 10,000 counts. After background- and LPA-corrections a parabola is fit to the top 85 % of the measured intensity data, which yields the peak position.

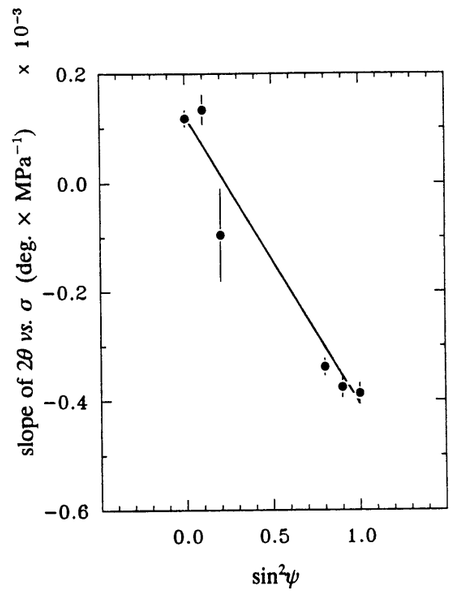

Fig. 5.3 The slopes of 6 lines like the one obtained in figure 5.2 as a function of $\sin^2\psi$. From these data points S_1 and $S_2/2$ are obtained employing a linear least squares fit (solid line).

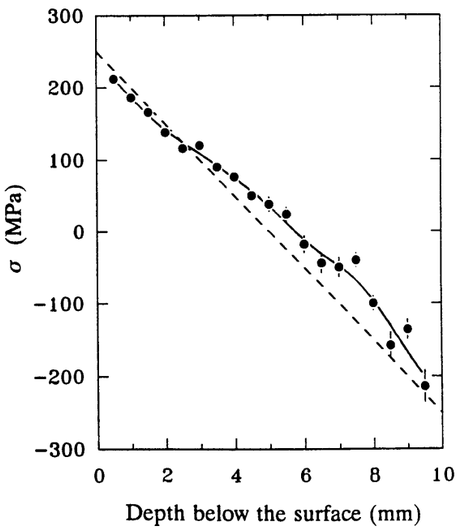

Fig. 5.4 Measured stress *vs.* applied stress, using the diffraction elastic constants obtained in the neutron calibration experiment. The broken line gives the expected results according to equation 5.1, while the solid line serves as a guide to the eye for the measured data.

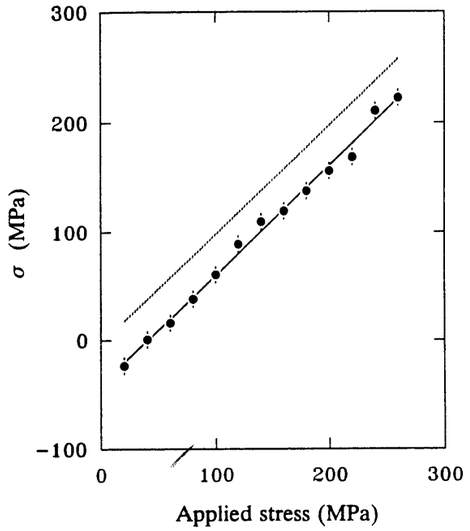

Fig. 5.5 Measured stress *vs.* applied stress using x-rays. The solid line is the result of a linear least squares fit to the measured data. The broken line shows the theoretical curve where the applied stress is equal to the measured stress.

5.6 RESULTS

In this section the results of the measurement of the diffraction elastic constants of steel, using x-ray and neutron diffraction will be presented.

5.6.1 Neutron measurements

In figure 5.2 an example of a $2\theta_\psi$ *vs.* σ plot is shown. As measurements were made at 6 different ψ-values, 6 plots like in figure 5.2 are obtained. The slope values of these 6 plots are plotted against corresponding $\sin^2\psi$ values in figure 5.3. From this figure the values for S_1 and $S_2/2$ were obtained by a least squares fit of a straight line, yielding

$$\begin{aligned} S_1 &= (-1.34 \pm 0.13) \times 10^{-6}\ \text{MPa}^{-1} \\ S_2/2 &= (\ 5.59 \pm 0.16) \times 10^{-6}\ \text{MPa}^{-1} \end{aligned}$$

Subsequently, the obtained $S_2/2$ was used to calculate the stress from $\sin^2\psi$-curves according to equation 5.5. The results are presented in figure 5.4.

5.6.2 X-ray measurements

Treatment of the x-ray data using a similar procedure as above resulted in

$$\begin{aligned} S_1 &= (-1.24 \pm 0.05) \times 10^{-6}\ \text{MPa}^{-1} \\ S_2/2 &= (\ 5.25 \pm 0.14) \times 10^{-6}\ \text{MPa}^{-1} \end{aligned}$$

Figure 5.5 shows the measured stresses that were obtained by using the determined $S_2/2$ value.

5.7 DISCUSSION

Theoretical calculations according to the Reuss approximation give the following values for the diffraction elastic constants for a ferritic steel [5.2][5.3]

$$\begin{aligned} S_1 &= -1.25 \times 10^{-6}\ \text{MPa}^{-1} \\ S_2/2 &= 5.81 \times 10^{-6}\ \text{MPa}^{-1} \end{aligned}$$

The presented results show that there is no significant difference between the determined neutron and x-ray elastic constants. Also, the values calculated according to the Reuss approximation are in reasonable agreement with the measurements.

From figure 5.5 it can be seen that the determined stress values deviate systematically from the applied ones. This is due to the presence of a compressive stress in the surface of the test specimen. Further confirmation of this was obtained by measurements on the (211) reflection using filtered Cr-radiation and a Rigaku stress analyzer employing a parallel beam geometry. It is important to note that this zero offset has no effect on the results for the x-ray diffraction elastic constants, because this systematic deviation is eliminated during the differentiation process, that has been described earlier.

A somewhat different situation is noticed in case of the neutron measurement results (figure 5.4). Measurement results from near surface regions of the bar are in good agreement with the predicted values. In the central part of the specimen, however, the measured stresses are systematically slightly higher than the applied ones. This can be partly explained from the compressive residual stress that is present on the surface, which should be balanced by the presence of residual tensile stresses in the interior, in order to maintain a force equilibrium over the cross section of the bar.

A second explanation can be found in the application of the correction procedure for the attenuation effect. This procedure has been applied, using a constant attenuation coefficient throughout the specimen. This coefficient has been obtained from an entering curve fit using the functions given in Appendix 3. When there exists a position dependent texture in the bar (*i.e.* a preferred orientation of the crystallites), the attenuation coefficient is no longer constant, but an unknown function of ψ and x. Consequently, for each ψ and x, a different effective attenuation coefficient should be applied. This would definitely change the results if texture is present.

When the lattice spacing is determined at a fixed scattering angle of 90° and by using the wavelength of the neutron beam as the scan parameter, we automatically get rid of both the attenuation effect and the umbrella effect. How this can be carried out will be discussed in Chapter 7.

5.8 CONCLUSION

The question whether it is possible to measure stresses by means of neutron diffraction, using the facilities and methods present in the laboratory in Petten has been answered positively through these experiments. However, the results presented in this chapter make it clear that a number of improvements have still to be implemented, in order to avoid the two main sources of systematic errors, *viz.* the umbrella effect and the attenuation effect.

REFERENCES

5.1 P.C. Brand; R.B. Helmholdt; B. Pathiraj and B.H. Kolster, *Proceedings of the 2nd International Conference on Residual on Residual Stresses ICRS 2*, Elsevier Applied Science, 216 (1989).

5.2 A.J. Allen; M.T. Hutchings; C.G. Windsor and C.Andreani, *Adv. Phys.*, **34**, 445 (1985).

5.3 A. Reuss, *Z. Angew. Math. Mech.*, **9**, 49 (1929).

6
Application on Engineering Cases

6.1 INTRODUCTION

In the preceding chapters it has been shown how stress measurements by means of neutron diffraction can be performed. It has been shown that the method gives correct results in case of a uniaxial stress state present in a bar subjected to pure elastic bending.

In this chapter an attempt to apply to more complex residual stress measurement problems is made. The following three different cases were chosen.

1. Determination of the diffraction elastic constants of a ceramic material: high density alumina (Al_2O_3).
2. Measurement of the triaxial residual stress state in quenched cylinders made of pure iron and martensitic steel as a function of the depth below the surface.
3. Measurement of the biaxial stress state in a cold rolled iron plate as a function of the depth below the surface.

The measurements on the ceramic material were carried out in order to show that neutron diffraction measurements are not limited to metals, but can be applied to any crystalline material. The measurements are closely related to the proof of the principle experiment performed, using an elastically bent bar, which has been discussed in Chapter 5. The choice of the ceramic is related to a research program at the Petten establishment concerning the creep behaviour of ceramics.

As a first approximation, neither the ceramic bar nor the quenched cylinders will possess a texture as a result of the way they are manufac-

tured. However, the rolled iron plate is expected to possess a depth dependent texture, which is characteristic for rolled iron.

Finite element calculations have been carried out on the quenching and rolling processes. In order to check these calculations as well as the neutron stress measurements, x-ray stress measurements have been performed on the quenched cylinders and on the rolled plate. The x-ray stress measurements as a function of depth were carried out using a successive layer removal technique, based on electrochemical polishing.

6.2 DIFFRACTION ELASTIC CONSTANTS OF ALUMINA

Alumina is an inorganic compound that shows a high elastic anisotropy. Consequently, the elastic behaviour of a specific crystallographic lattice plane (*hkl*) differs from the macroscopic elastic behaviour. As we have shown in Chapter 5, the different elastic behaviour for different lattice planes can be described by defining (*hkl*)-dependent elastic constants, which are called diffraction elastic constants (DEC's). In this investigation, we have determined the DEC-values for the (202)-reflection of alumina. This alumina reflection is attractive for our measurements for two reasons

1. It is the strongest reflection from the alumina structure.
2. The peak position angle for the wavelength ($\lambda = 0.257$ nm), that is employed in our diffractometer is $2\theta \approx 76°$, which is reasonably close to the ideal angle of 90°.

6.2.1 Background of the problem

The use of ceramic components at high temperatures is limited by the tendency of these materials to creep. Creep might eventually lead to failure of the component by creep rupture. Knowledge of the creep behaviour of ceramic materials is therefore of importance in determining the lifetime at high temperatures.

Creep tests on ceramics are often performed using four point bending tests at elevated temperatures. Compared to tensile tests there are major advantages in this testing procedure which is, however, carried out at the expense of a more complicated analytical evaluation. By

measuring the deflection of the bending bar during creep tests, the parameters of appropriate creep laws can be determined [6.1][6.2]. The stress distribution and the residual stresses after unloading can be calculated using a method developed by Fett *et.al.* [6.1]. In the future, one may like to determine this residual stress distribution by means of neutron diffraction in order to check the stress prediction method which is related to the choice of the creep laws to be applied. Therefore, as a trial experiment, the DEC-values of alumina have been determined using neutron diffraction on a four point bending bar that is large compared to a creep test specimen. The experiment serves two major purposes.

1. The neutron scattering- and attenuation behaviour of alumina can be studied using a fairly large sample, so that a prediction can be made on how long measurements on very small creep test specimens will take.
2. When future stress measurements will be carried out on creep test specimens, the determined DEC-values can be directly applied.

6.2.2 Specific theory

The calibration experiment was carried out on an alumina bar subjected to four point bending. Four point bending leads to a depth dependent uniaxial stress profile as was explained in Chapter 5 (equation 5.1). In Chapter 5, also the relationship between the strain in a direction ψ and the applied stress was given for a uniaxial stress situation.

In the experiment described here, the stress at the measurement location is altered by applying different loads using the bending jig (*cf.* figure 5.1), which is contrary to the situation for the steel bar described in Chapter 5, where the applied stress level was chosen by performing measurements at different depths. The advantage of measuring at a fixed depth, (not too far) below the surface is that the average beam path through the specimen (and therefore the attenuation) is kept as low as possible, thus reducing the total measuring time needed for the experiment.

6.2.3 Specimen preparation

A dense alumina bar was manufactured by cold isostatic pressing at 200 MPa, using Martins Werke C5400 MS Powder (99,7% Al_2O_3). This was carried out at the National Ceramics Workshop in Petten under the supervision of P. Bach. A bar of 35 mm × 35 mm × 450 mm was pre-sintered and subsequently sectioned into two bars of 30 mm × 15 mm × 400 mm size. After sintering at 1600°C for 1 hour the bars were machined to their final dimensions of 10 mm × 12 mm × 320 mm. The residual stresses due to the machining process are expected to be confined in a near surface region of less than 20 μm, so that they will not influence the neutron stress measurements. The relative density of the final specimen was 98%.

6.2.4 Experimental details

The powder diffractometer at HB5 at the High Flux Reactor in Petten was modified according to the methods described in Chapter 4. The modifications involved a reduction of the sample volume to about 1 mm × 1 mm × 12 mm by means of the developed double slit system. On the specimen translation table the bending device that was treated in Chapter 5 was mounted. The force $2P$ applied on the ceramic bar was monitored by means of a force transducer. In the course of the experiment, $2P$ was varied from 100 N to 700 N in 7 steps. Taking into account the dimensions of the bar and the bending device and the fact that the centre of gravity of the sample volume is situated 1.0 mm below the bar surface, it can be calculated from equations 5.1 and 5.2 that the corresponding stress changes are from 15 MPa to 105 MPa.

The positioning of the specimen before the first measurement is carried out using the entering curve method described in Chapter 4. The position where the specimen surface is exactly covering the diffractometer axis is transferred to the position of a needle that is attached to the primary slit assembly. For this purpose an electrical contact was established between the needle and a reference electrode, which is rigidly connected to the bent specimen.

After each loading, the specimen table position at which the electrical contact just touches the reference electrode is the home position for the set of measurements at that particular load. The position

is found by means of an ohmmeter. This procedure proves to be accurate within 0.02 mm.

Using this set-up, alumina (202)-diffraction peaks were registered at 4 different values of ψ (0°, 20°, 65°, and 90°). The adjustable slit system defines the sample volume to about 1 mm × 1 mm × 12 mm, such that for all ψ-values the sample volume lies entirely inside the specimen.

6.2.5 Results

The entering curve that served as the basis for the specimen positioning and the determination of the attenuation coefficient is given in figure 6.1. The fit results for the entering curve function of Appendix 3, are summarized in Table 6.1. All the specimen positioning procedures were based on this entering curve, so the uncertainty in the specimen position (*viz.* 0.05 mm being the square root of the quadratic sum of the statistical error from the fit and the electrical contact positioning error) is the same for all applied stress values.

The diffraction peak positions were obtained from a Gaussian fit to the measured intensity profiles. Subsequently, the slopes of the peak position *vs.* applied stress plots (not given here) were calculated using a least squares straight line fit procedure. Just like in the previous chapter this fit should also be linear. This result is presented in figure 6.2.

From the slope and vertical axis intercept of figure 6.2, the elastic constants S_1 and $S_2/2$ can be derived using equation 5.6. The determined values of S_1 and $S_2/2$ are given in Table 6.2. From the values of S_1 and $S_2/2$ so determined, the apparent values of Youngs modulus and Poisons ratio can be calculated using the relationships

$$S_1 = -\frac{\nu}{E} \qquad \text{and} \qquad \frac{S_2}{2} = \frac{1+\nu}{E} \tag{6.1}$$

The results of this calculation are also given in Table 6.2.

6.2.6 Discussion

In Table 6.2 the macroscopic isotropic values for E and ν of alumina are given. From Table 6.2 it is evident that alumina is strongly anisotropic in its elastic behaviour. Especially the difference between the macroscopic

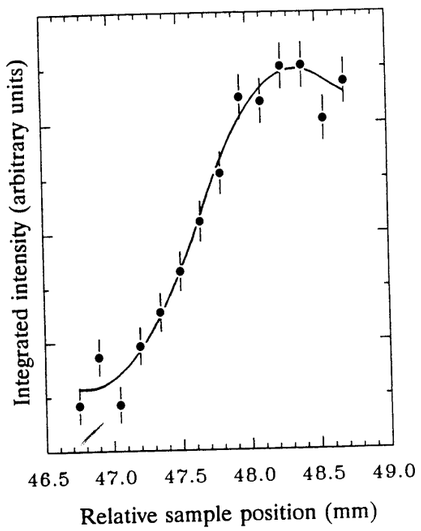

Fig. 6.1 The entering curve for the measurements on the alumina bar. The solid curve is the result of a fitting procedure using the functions described in Appendix 3 (*cf.* Table 6.1).

elastic constant ν and the measured value for ν is striking. This illustrates the need for calibrated constants when performing stress measurements on such materials.

The ultimate purpose for which the present measurements serve as a trial experiment, was to see whether it is possible to measure the residual stress state as a function of depth in a bar as small as 60 mm × 5 mm × 5 mm, which is the size of the specimen used in the above

Table 6.1

Relevant parameters of the entering curve fit according to the equations given in Appendix 3.

parameter	value	error	unit
Relative surface position	47.64	0.04	mm
Slit openings	1.15	0.10	mm
Attenuation coefficient	0.02	0.03	mm^{-1}

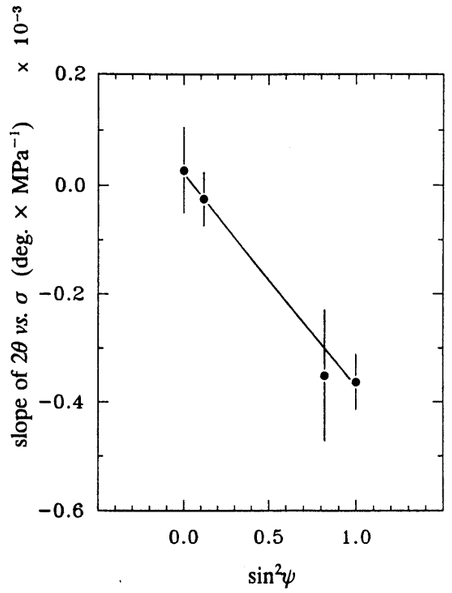

Fig. 6.2 The final plot for the calculation of the diffraction elastic constants of alumina. The data points represent the slopes of the plots of the peak position 2θ *vs.* the applied stress value in the sample volume. The solid line is the result of a least squares fit of a straight line to the data points. From the slope and the intercept values of this line the DEC-values are calculated.

Table 6.2

Final result for the diffraction elastic constants of alumina

elastic constant	value	error	unit
this work			
S_1	$-0.24\ 10^{-6}$	$0.11\ 10^{-6}$	MPa^{-1}
$S_2/2$	$4.38\ 10^{-6}$	$0.17\ 10^{-6}$	MPa^{-1}
ν	0.06	0.03	-
E	241.4	7.1	GPa
isotropic values			
ν	0.25	-	-
E	360	-	GPa

mentioned creep tests. In a specimen that small, the sample volume must be of the order of 0.5 mm × 0.5 mm × 5 mm for a longitudinal stress measurement (up to 0.5 mm × 0.5 mm × 20 mm for a transverse stress measurement) in order to obtain a spatial resolution that makes sense in comparison with the outer dimensions of the specimen. The present sample volume is about 10 times larger for longitudinal measurements. Hence for measurements on creep specimens, the measurement duration should be roughly 10 times longer for the longitudinal direction in order to obtain the same counting statistics (*i.e.* provided that the background level can be kept low enough as was explained in Chapter 2). In the present experiments, the measurement time was 6 hours per peak, so for measurements on a creep sample in longitudinal direction, roughly 60 hours per peak would be necessary. This large measurement time could be reduced by employing a vertical stack of – say five – creep specimens with their edges placed adjacent to each other (with overall size 60 mm × 25 mm × 5 mm). This would enable a five times higher sample volume for longitudinal measurements. In such a case each unit in the stack must have been subjected to the same creep test conditions, which is feasible. Using this type of stacked samples could reduce the measurement time by a factor which is equal to the number of samples employed.

6.3 FINITE ELEMENT CALCULATIONS

Before continuing with the presentation of the measurements on the quenched cylinders and the cold rolled plate, a few remarks on the method by which the stress state in those specimens can be predicted will be given.

The quenching and rolling process are simulated by means of a calculation method that is called the finite element method. This method can be characterized as a numerical way to solve a (complex) set of (partial) differential equations. These equations result from physical conservation laws (conservation of mass, momentum, energy *etc.*). In addition to these general laws, a mathematical description of the material – the constitutional equations – are required. The description of the materials used in the present study is based on a continuum theory for large elastic-plastic deformations. Thermal effects like expansion and phase transformations are also included.

A detailed description of the method is beyond the scope of this thesis, however, it can be found in [6.3]. The used simulation program is called DIEKA. It has been developed at Twente University. The simulations on the quenched cylinders were carried out at Twente University [6.4], while the simulations on the cold rolled plate were performed at Hoogovens, IJmuiden [6.5].

6.4 QUENCHED IRON AND STEEL CYLINDERS

When a hot material in the form of a cylinder is quenched in oil or water, a tri-axial residual stress state develops in the material as a consequence of non-uniform plastic deformation [6.6]. The developed stress state is a function of the radius of the cylinder. The exact form will depend on the temperature, the cooling rate and the flow properties of the material of the cylinder. The development of the residual stress state is due to the non-uniform cooling of the specimen from surface to interior, which induces non-uniform plastic deformation.

A second cause for the development of residual stress is due to a phase transformation at relatively lower temperatures *e.g.* the forming of martensite during quenching of high carbon steel.

6.4.1 Choice of specimens and heat treatments

In order to obtain a reasonable spatial resolution compared to the diameter of the cylinder we chose cylinders with a diameter of 15 mm. The length was chosen to be 100 mm which is in practice infinitely long compared to the diameter.

Table 6.3

Chemical composition of the U.L.C. steel and the high carbon steel that was used in the present experiments.

Material	C	Si	Mn	Cr	V	Al
U.L.C.	0.002	0.012	0.195	0.016	-	0.058
90MnV8	0.9	0.25	2.0	0.35	0.10	-

Two materials have been used: Ultra Low Carbon (U.L.C.) steel, supplied by Hoogovens and an oil hardening carbon steel (90MnV8) which was obtained with the help of the Foundation for Advanced Metals Science in Enschede. In Table 6.3 the chemical compositions of both steels are given.

Two different heat treatments were given to both steels, with the purpose to create a distinct residual stress state. The first heat treatment involves holding for 30 minutes at 820°C and then quenching in oil. The second heat treatment employed a holding time of 30 minutes at 820°C followed by a quenching in water. However, only the U.L.C. specimen could be water quenched successfully, as the 90MnV8 specimen showed cracks after quenching in water due to the high severity of quench.

A third specimen, made of U.L.C. was given a stress relief treatment for 4 hours at 640°C followed by a slow cooling in the oven, in order to serve as a specimen for the determination of the stress free lattice parameter of U.L.C.

6.4.2 Neutron stress measurements

In order to solve the complete tri-axial stress state in the interior of a cylinder, an assumption will be made that the principal axes of the stress tensor are parallel to the main axes of the cylinder. As during the quenching process the heat flow field is uniform and symmetrical, this is a reasonable assumption.

As was already pointed out in Chapter 3, it is impossible to solve for the three unknown principal stresses σ_r, σ_θ and σ_z, without knowing the stress free lattice distance d_0 for the (110)-planes. For the U.L.C. specimens d_0 was obtained from the measurements on the stress relieved specimen. In the martensitic specimen, however, d_0 was not found to be a constant as a function of the radius. This perhaps is related to a possible inhomogeneity in the microstructure. Due to differences in cooling rates between surface and interior, the amount of transformed martensite can vary from 100 % at the surface to lower percentages at the interior. This phenomenon will be illustrated by using the x-ray measurements that have been performed on the martensitic specimen.

In x-ray measurements using a successive layer removal technique, a knowledge of d_0 is not necessary. This is due to the fact that x-ray

measurements are confined to the surfaces where the stress state is always bi-axial (*cf.* Chapter 3).

A solution for the stress free lattice constant problem in martensitic steel can thus never be found without destroying the entire specimen and performing x-ray measurements as a function of depth. These x-ray results must be brought to the same absolute scale as the neutron measurements, which poses an enormous experimental problem. For this reason, as far as the neutron depth stress measurements are concerned, we have restricted ourselves to the U.L.C. specimens.

The grain size of the U.L.C. specimens was in the order of 0.1 mm. In order to obtain a better crystal diffraction statistics (*i.e.* to have more grains in the diffracting position during a measurement), the specimens were centrally mounted on a rotation device. The combined rotation device and specimen was mounted on the diffractometer specimen table. The alignment of the cylinders in the diffraction geometry was achieved using the entering curves obtained with the standard powder specimen and the electrical contact method described in Chapter 4. The radius co-ordinates at which the stress measurements were performed are r = 0, 2, 4, 6 mm.

In order to solve the complete stress state, two sets of measurements were performed in two diffraction measurement configurations.

1. The cylinder was placed with its axis vertical. Neutron beam apertures limiting the beam cross sections to 1 mm × 20 mm for both the primary and secondary beams were placed. In this way the total sample volume is about 20 mm^3. In this configuration, the scattering vector $\boldsymbol{q}$ is always perpendicular to the cylinder axis. In this arrangement, 4 different ψ-values (*i.e.* 0°, 35.67°, 54.33° and 90°) were employed per measurement in tangential direction.
2. The cylinder axis was placed horizontally, employing neutron beam apertures limiting the beam size to 2 mm × 2 mm. The sample volume is now about 8 mm^3. In this configuration, the scattering vector is always perpendicular to the tangential direction of the cylinder. In this arrangement, 3 different ψ-values (*i.e.* 18.43°, 71.57° and 90°) were employed per measurement in longitudinal direction.

The solution of the stress state has been according to the theory of Chapter 3. If we use the following relations for the principle stresses

$$\begin{aligned} \sigma_{11} &= \sigma_r \\ \sigma_{22} &= \sigma_\theta \\ \sigma_{33} &= \sigma_z \end{aligned} \tag{6.2}$$

the orientation matrix $\boldsymbol{K}$ takes the following shape

$$\boldsymbol{K} = \begin{pmatrix} 1 & 1 & 0 & 0 & 0 & 0 & 0 \\ 1 & 0.666 & 0.333 & 0 & 0.471 & 0 & 0 \\ 1 & 0.333 & 0.666 & 0 & 0.471 & 0 & 0 \\ 1 & 0 & 1 & 0 & 0 & 0 & 0 \\ 1 & 0.9 & 0 & 0.1 & 0 & 0.3 & 0 \\ 1 & 0.1 & 0 & 0.9 & 0 & 0.3 & 0 \\ 1 & 0 & 0 & 1 & 0 & 0 & 0 \end{pmatrix} \tag{6.3}$$

6.4.3 X-ray stress measurements

The x-ray measurements were performed using a Rigaku stress analyzer. The stress measurements consist of two series of $\sin^2\psi$-measurements, one in the longitudinal direction of the cylinder and the second in the tangential direction. In order to obtain the stress values as a function of the radius (depth), a successive layer removal technique based on electrochemical polishing was applied. Due to the removal of stressed layers, the stress state of the cylinder alters. Therefore a correction procedure as proposed by Moore and Evans [6.7] has been applied.

As the x-ray measurement of stresses is confined to the surface, the stress field under investigation is a bi-axial one. This offers the possibility to deduce the stress free lattice parameter d_0, from a set of perpendicular $\sin^2\psi$-measurements. In terms of the theory described in Chapter 3, this corresponds to a stress constraint of the form: σ_{33} $(= \sigma_z)$ $= 0$, which affords us to have one extra unknown in the set of equations to be solved, which is d_0.

6.4.4 Final results

The obtained neutron diffraction profiles were treated according to the methods outlined in Chapter 2. This means that both the umbrella effect and the attenuation effect have been taken into account. This reduces the information contained in one diffraction profile to one single d-value. All d-values measured at a certain radius are treated according to the procedure described in Chapter 3, yielding the values for σ_θ, σ_z and σ_r.

The x-ray diffraction profiles are treated according to the standard procedure offered by the Rigaku instrument which involves background substraction, LPA correction and fitting of a parabola to the top 85 % of the diffraction intensity profile. The stress calculation that follows is performed using the theory explained in Chapter 3 so that in one calculation σ_θ, σ_z, and d_0 are obtained. The diffraction elastic constants used in these calculations are from the experiments presented in Chapter 5.

In the figures 6.3, 6.4 and 6.5 the combined neutron, x-ray and finite element analysis results for both U.L.C. specimens are presented. In figure 6.6 the results of the determination of the strain free lattice distance are presented for all the specimens including the martensitic one.

6.4.5 Discussion

The results of stress determination by different techniques for the U.L.C. specimens shown in figures 6.3, 6.4 and 6.5 indicate large differences. It is difficult to offer a straightforward explanation as to why the differences are so large. One of the reasons may be related to the difference in spatial resolution in radial direction for both applied measurement techniques *viz.* x-ray and neutron diffraction. For neutron diffraction, the depth over which the averaging takes place is in the order of 1 to 2 millimetres, while in the x-ray case this averaging depth is in the order of about 10 μm. This may explain numerical differences in the measurement results. However, it should not vastly influence the trends indicated by both techniques.

A second explanation may be due to the fact that the U.L.C. steel tested was a very coarse grained material. Normally this phenomenon is known to give an enormous scatter in $\sin^2\psi$-curves, because only very few grains contribute to the diffracted intensity. We have tried to compensate for this by rotating the specimen about its own axis, thus bringing several crystallites into diffracting conditions. This apparently has not been

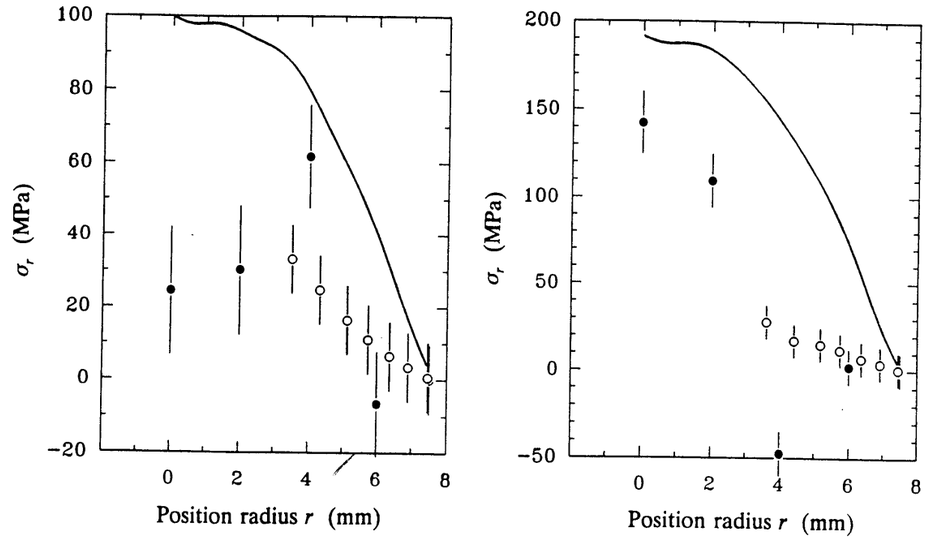

Fig. 6.3 Radial residual stresses σ_r distribution determined in U.L.C. steel cylindrical specimens. The left graph refers to the oil quenched specimen and the right graph to the water quenched specimen. The open and dark circles represent the x-ray- and neutron measurement results respectively. The drawn lines are the result of the finite element calculations.

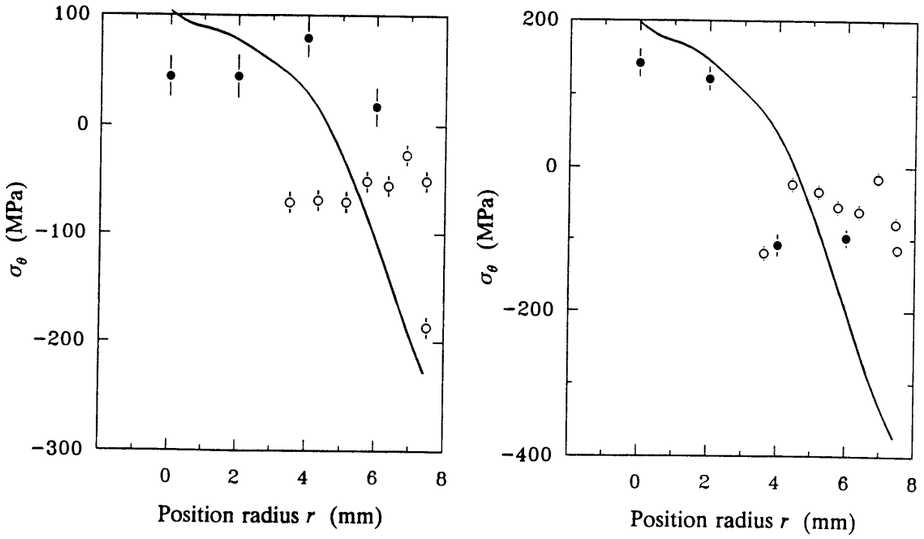

Fig. 6.4 Circumferential residual stresses σ_θ distribution determined in U.L.C. steel cylindrical specimens. Other details are similar as those given in figure 6.3.

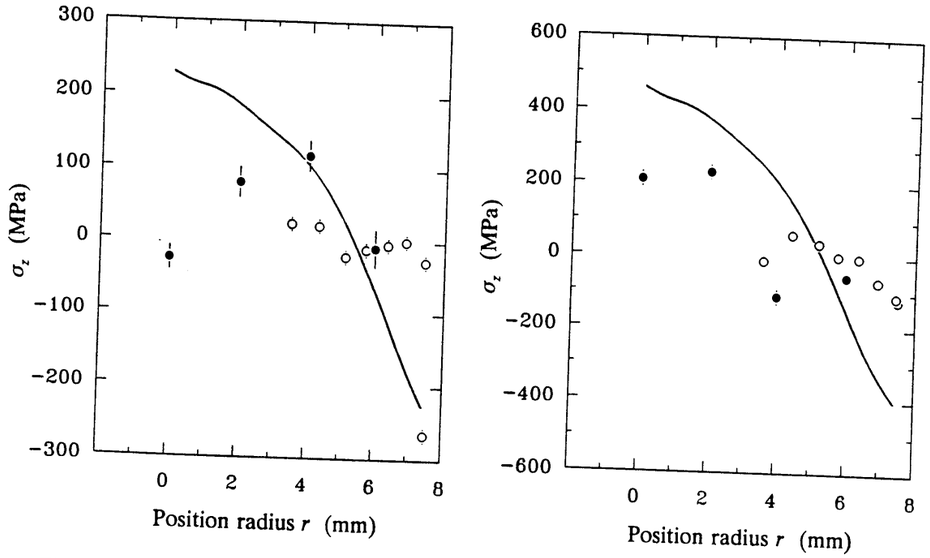

Fig. 6.5 Axial residual stresses σ_z distribution determined in U.L.C. steel. Other details are similar as those given in figure 6.3.

adequate. We must remark, however, that this has not in the least induced any scatter in the stress free lattice parameter d_0 as presented in the two bottom curves of figure 6.6 which may be understood from the fact that these d_0-values are results from many lattice parameter determinations, so that a better average has been obtained.

The finite element predictions for the stress state in the quenched cylinders indicate gradual changes. Unfortunately this could not be verified due to a poor agreement with both the x-ray and the neutron measurements.

In spite of the deviations, one can still see some agreements to physical expectations. The oil quenched cylinders should contain residual stresses of lower magnitude as compared to the water quenched cylinders, since the severity of quench and the consequent plastic deformation are higher with water quenching. The results agree with this. (compare left sides of figures 6.3, 6.4 and 6.5 to the corresponding right sides). It is also worth mentioning that with neutron measurement at a radius of 4 mm many of the measurement results show a consistent but significant deviation as compared to results obtained at other radii. Though such

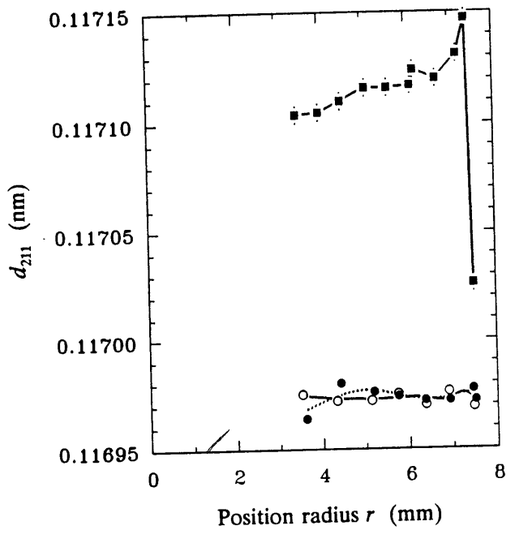

Fig. 6.6 The stress free lattice distance determined by means of x-ray diffraction in quenched material. The top curve are the values for 90MnV8. The curves below are the values for U.L.C. (open symbols: oil quenched, closed symbols: water quenched). The drawn curves serve as a guide to the eye.

deviations are not evident from the x-ray results, it is difficult to make any qualifying statements as the x-ray measurements were not continued to greater depth. Also, the interval at which the neutron measurements were performed is somewhat large (2 mm) which makes the analysis difficult. The incomplete x-ray measurements and the neutron measurements at large intervals were due to experimental difficulties and the large grain size of the material (and the consequent need to rotate the specimen).

From figure 6.6 it is clear that the martensitic steel in the 'as quenched' state cannot be characterized by one stress free lattice parameter, due to the inhomogeneity in the microstructure. The as calculated value for d_0 gradually changes with the radius of the measurement site, resulting from a decrease in martensite percentage with depth from the surface. An interesting observation, however, is the sudden decrease for the stress free lattice parameter at the surface of the cylinder (*i.e.* at $r = 7.5$ mm). This may be resulting from a depletion of carbon in the near surface region, due to oxidation which can take place during

the heat treatment (this was indeed confirmed by a much lower value for the full width at half maximum of the x-ray profiles at the surface as compared to the interior). A lower carbon content will lead to a smaller d_0, because of the interstitial occupancy of the solute atom *viz.* carbon. From figure 6.6 it can be seen that the d_0-value at the surface of the hardened specimen lies between the values at some depth (martensite) and the value for U.L.C steel (ferrite) that hardly contains any carbon. From this we may conclude that only a partial decarburization has taken place at the surface, in this discussion we neglect the influence of the other alloying elements of the steel like chromium, manganese and nickel, as they occupy substitutional positions in the crystal lattice.

As was pointed out before, the martensite percentage of the 90MnV8 cylinder is expected to decrease with depth, because of the lower cooling rates at the interior which experiences a less severe quench. Due to this, the diffraction from the sample is not only due to the martensite but also due to the ferrite and bainite. The resulting diffraction profiles will all overlap as the difference in lattice spacings are small and the structure is almost the same (b.c.c. or b.c.t). Diffraction from all these structures will contribute to the breadth of the measured profile. The result of this is an apparent decrease in d_0 which has to be accounted for in tri-axial stress analysis. Results of figure 6.6 support this. Some influence of retained austenite can also be expected, which will not be elaborated here.

After these measurements on the martensitic specimen we concluded that it had no use analyzing the neutron results that had been obtained from the martensitic specimen unless it was subjected to the layer removal procedure and surface measurements are done by means of neutrons (which is hardly possible with neutrons).

Stress free lattice parameter determination may be a good means to establish, whether or not the individual stress measurements have been performed correctly. In a homogeneous material d_0 should be the same throughout a specimen. Obtaining this result is necessary, but need not necessarily mean that the stress measurements can be successful. As can be seen from figure 6.6, this stress free lattice parameter condition has been fulfilled for the U.L.C. specimens. However, the stress results are not conclusive.

6.5 COLD ROLLED U.L.C. PLATE

The cold rolling process is characterized by complex and non-uniform plastic deformation. Consequently, residual stresses develop in the material due to cold rolling [6.8][6.9]. Both the elastic and plastic behaviour of iron are to some extent anisotropic. Therefore, besides a residual stress state, a cold rolled piece of iron will also posses a certain texture. Texture is defined as the existence of preferred orientations in a polycrystalline material. During rolling, the plastic deformation starts at the surface and proceeds inward. The plastic deformation is caused by what is called as slip or glide of dislocations in certain crystallographic directions. Due to the constraints imposed by the rolls the material has to flow in a particular direction, where there is a freedom of flow (rolling direction). This leads to the development of texture.

As the elastic behaviour of iron is anisotropic, the presence of texture imposes difficulties on stress measurements by means of diffraction techniques. The macroscopic behaviour of a textured material will be somewhere between a perfectly anisotropic single crystal and a perfectly isotropic randomly oriented polycrystalline material. Theoreticians of various background have been working on this phenomenon since a long time now [6.10][6.11] and it is not on this place that we would pretend to add something new to this enormous problem. It can be seen, however, that for materials, which are interesting from a neutron diffraction stress measurement point of view, the texture will always play a minor role. To that end it should be realised that a strong texture usually develops after a cold forming process inducing several hundreds of percentage of plastic deformation. This holds *e.g.* for cold rolling thin sheet and wire drawing to small sizes. Cold rolling of materials, to a final thickness in the order of a centimetre is only applicable for moderate reductions and consequently lead to a not very strong texture. In fact those materials worth investigating with neutrons have to have certain minimum dimensions. The resulting not too strong texture may not have any influence at all on the stress measurements.

The formation of dislocations and their glide mechanisms are both responsible for the development of texture as well as residual stresses. The formation of dislocations, however, also has a separate effect which is the strengthening of the cold worked product, caused by the earlier formed dislocations obstructing the movement of newly formed ones. So

during the cold rolling process, as a first approximation, we expect a work hardening proportional to the amount of plastic deformation.

Work hardening is known to continuously disappear during the hot working of materials. The processes involved are dynamic recovery and recrystallisation which takes place at higher temperatures as compared to the dynamic recovery. The temperatures at which both dynamic recovery and recrystallisation may take place, decrease with increasing amounts of plastic deformation and dislocation density. During cold working (rolling, wire drawing *etc.*), an appreciable amount of heat is dissipated due to the internal friction within the material. This causes the temperature to rise as the heat can not be extracted from the material immediately. It was shown by Aernoudt [6.12] and Denis *et.al* [6.13] that during wire drawing at room temperature, the combined effect of high dislocation density and temperature elevation can cause both dynamic recovery and recrystallisation in the drawn material. In our case, the dimensions of the plate are such that the ratio of heat production and heat conduction to the rolls is high, so a substantial raise of the temperature during rolling may be expected.

During the cold rolling, the dislocation density at the surface region is higher than at the interior of the plate. But the surface temperature will be somewhat lower than that at some depth below, due to the fast cooling at the surface. So if dynamic recovery and/or recrystallisation take place, their effect will be maximum at a region near the surface where the temperature effect as well as the deformation effect are the highest. If dynamic recovery or recrystallisation takes place, they can have a distinct effect on the measured stress state as well as on the breadth of diffraction peaks obtained as a function of the depth below the surface.

The influence on the texture of rolled material will be different for either dynamic recovery and recrystallisation. While the dynamic recovery gives rise to a polygonalisation in the individual crystallites only, the recrystallisation will actually form completely new crystallites due to a nucleation and growth process. The new crystallites formed by recrystallisation may possess a texture that is different from the non-recrystallised material.

In this section, measurements of the residual stress state of a cold rolled iron plate (U.L.C.) by means of x-ray and neutron diffraction will be presented along with texture measurements as a function of the depth. The measurements will be compared to finite element calculations that

have been performed at Hoogovens [6.5]. It will be shown from the results, that dynamic recovery as well as recrystallisation do play a role.

6.5.1 Specimen preparation

The cold rolled specimen was produced at Hoogovens with the help of F. van Eck. The starting material was a U.L.C. steel cube of 100 mm (volume 1 dm^3), possessing a chemical composition according to Table 6.3. The steel was hot rolled at approximately 640°C to a final thickness of 20 mm. After cooling and surface cleaning, the remaining piece was cold rolled to a final thickness of 10 mm. The reduction scheme is presented in Table 6.4. It has to be mentioned here that the time between successive rolling passes was short (several seconds) compared

Table 6.4

Sequence for the cold rolling process on U.L.C. steel. The diameter of the applied rolls was 228.6 mm.

Pass number	Thickness after pass (mm)
0	19.8
1	19.5
2	18.9
3	18.4
4	17.9
5	17.1
6	16.5
7	16.0
8	15.3
9	14.7
10	13.8
11	13.1
12	12.3
13	11.6
14	11.0
15	10.3
16	9.9

to the time needed for a complete cooling down to room temperature, which would be in the order of 20 to 30 minutes.

The final plate, having a length of about 1 metre was used to produce several specimens. A piece of 250 mm length and breadth 110 mm served as the stress measurement specimen. The remaining part has been used for making the samples for the texture measurements.

The preparation of samples for texture measurements is very time consuming. It was carried out in several steps using spark erosion. From the plate, 1 mm thick slices were cut in planes parallel to the rolling plane. In this way slices were obtained from different depths below the surface. (*viz.* 0-1 mm; 1-2 mm *etc.*). These slices, with dimensions of about 100 mm × 20 mm× 1 mm were subsequently cut to strips of 100 mm × 9 mm × 1 mm, which were subsequently cut to squares of 9 mm × 9 mm × 1 mm. During the spark erosion process steps, care was taken to indicate the rolling direction and depth origin of every slice. Finally, the little squares belonging to the same depth below the surface of the original specimen were stacked together forming small cubes making sure that their individual rolling direction orientations were maintained parallel. In this way 10 specimens were prepared, so the texture as a function of the depth below the surface can be measured with a depth resolution of 1 mm.

6.5.2 Neutron stress measurements

If we assume the orientation of the principal axis system to be parallel to the rolling axis system of rolled plate, the stress state can be proved to be a biaxial one. This can be understood from the fundamental laws of mechanics in the following way. As the shear stresses are all equal to zero in the specimen axis system (*i.e.* the principal axis system), there is no shear stress gradient available in the direction perpendicular to the plate. The stress perpendicular to the plate, σ_z, is proportional to the shear stress gradient, so without a gradient σ_z can never reach any value other than zero, as at the free surface $\sigma_z = 0$. This reasoning applies for any flat plate for which one can be sure that the principal axes follow the main dimensions of the plate (when the principal axis system rotates as a function of depth, this reasoning will not apply).

Determining the biaxial stress state was performed through two series of mutually perpendicular $\sin^2\psi$ measurements. During the first set, the

rolling direction is kept parallel to the diffractometer axis, while during the other, the rolling direction is kept perpendicular to the diffractometer axis such that the diffractometer axis is parallel to the plane surface of the plate. The positioning of the specimen in the diffractometer geometry is according to the standard procedure described in Chapter 4.

As the thickness of the rolled plate is 10 mm and the rolling process must be expected to produce a symmetrical residual stress pattern, we have only performed measurements up to half the thickness of the plate. The depths at which measurements were performed range from 0.5 to 5 mm in steps of 0.5 mm. The ψ-values at which the diffraction peaks were scanned are in both cases: 0°, 30°, 60° and 90°. The scan results were used as input for the data reduction procedures described in the Chapters 2 and 3, resulting in the solution of the longitudinal stress σ_l, the stress transverse to the rolling direction σ_t and the stress free lattice parameter d_0. If the following relations are chosen with respect to the theory described in Chapter 3

$$\begin{aligned} \sigma_{11} &= \sigma_l \\ \sigma_{22} &= \sigma_t \\ \sigma_{33} &= 0 \end{aligned} \tag{6.4}$$

the $\boldsymbol{K}$ matrix reduces to

$$\boldsymbol{K} = \begin{pmatrix} 1 & 0 & 0 & 1 & 0 & 0 & 0 \\ 1 & 0.25 & 0 & 0.75 & 0 & 0.433 & 0 \\ 1 & 0.75 & 0 & 0.25 & 0 & 0.433 & 0 \\ 1 & 1 & 0 & 0 & 0 & 0 & 0 \\ 1 & 0 & 0 & 1 & 0 & 0 & 0 \\ 1 & 0 & 0.25 & 0.75 & 0 & 0 & 0.433 \\ 1 & 0 & 0.75 & 0.25 & 0 & 0 & 0.433 \\ 1 & 0 & 1 & 0 & 0 & 0 & 0 \end{pmatrix} \tag{6.5}$$

6.5.3 Neutron texture measurements

At another beam port of the reactor at Petten, a single crystal diffractometer is located. This instrument can be operated as a texture goniometer as well.

The principle of a texture measurement is simple, the specimen is rotated around two axes in a stepwise manner. One axis is perpendicular to the surface of the specimen (the φ-axis), the other inclines the φ-axis from a fully vertical to a fully horizontal position in the diffraction geometry (the χ-axis). For each position in this two dimensional orientation space, the intensity of one of the available crystallographic reflections is measured by counting, during the time needed for a fixed number of neutrons to pass by.

The representation of the measurement results is in the form of pole figures, the principle of which can be found in any textbook on texture analysis [6.14]. For each sample, three pole figures have been measured (*viz.* the 110, 200, and 211 pole figures), in order to be able to obtain the orientation distribution function (ODF) according to the method of Bunge [6.14].

A more traditional way of determining texture pole figures is x-ray diffraction. The advantage of the use neutron diffraction for texture analysis over x-ray diffraction is twofold

1. The full φ-χ space can be scanned without the occurrence of a grazing angle geometry that is encountered in x-ray diffraction for $\chi > \approx 75°$. This is especially advantageous when calculating ODF's from measured pole figures, as no assumptions about the form of the pole figure in missing areas ($\approx 75° < \chi < 90°$) have to be made.
2. As the irradiated sample volume is larger during neutron measurements, a better volume average can be obtained than with x-ray diffraction. However, this is not an advantage in the case of the determination of the texture of a thin layer on a substrate.

6.5.4 X-ray stress measurements

Using the Rigaku system, standard $\sin^2\psi$ measurements have been performed as a function of the depth in the rolled plate. After successive

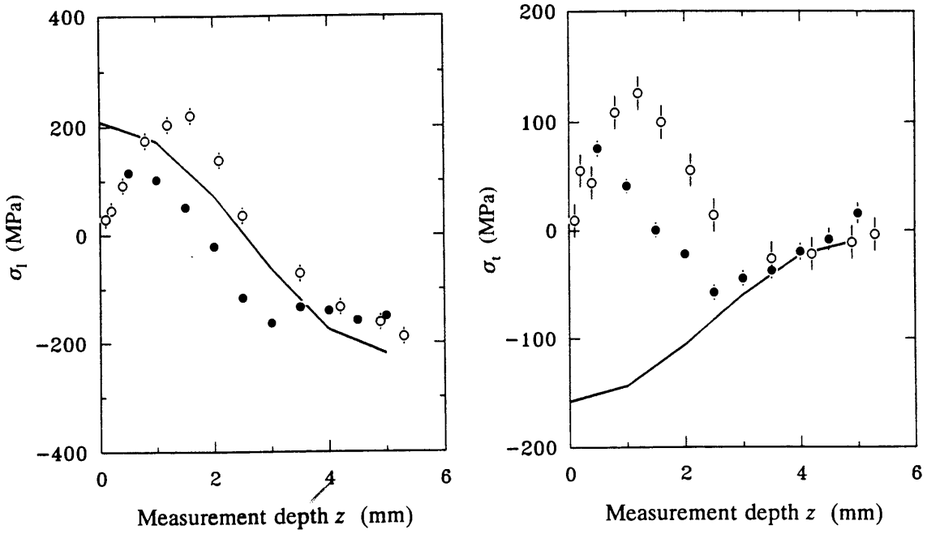

Fig. 6.7 Stress determination results for the stress in rolling direction σ_l (left graph) and the stress in transverse direction σ_t (right graph). The open symbols represent x-ray measurements, the closed symbols represent neutron measurements. The drawn lines are the result of finite element calculations.

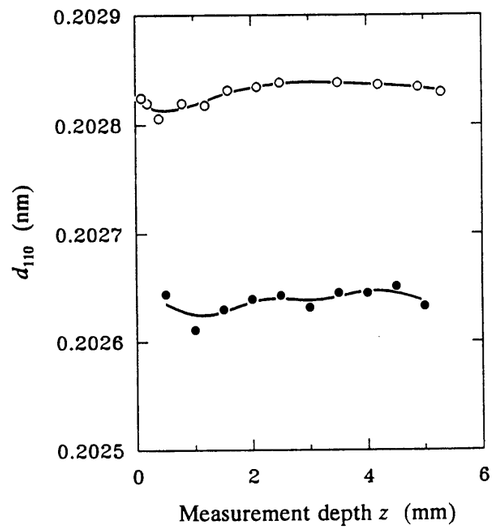

Fig. 6.8 Values for the stress free lattice parameter d_0 as found by neutron and x-ray measurements. The open symbols represent x-ray measurements, the closed symbols are neutron values. The x-ray results, which have been obtained using the (211)-reflection of iron have been scaled to (110)-values. The drawn lines serve as guides to the eye.

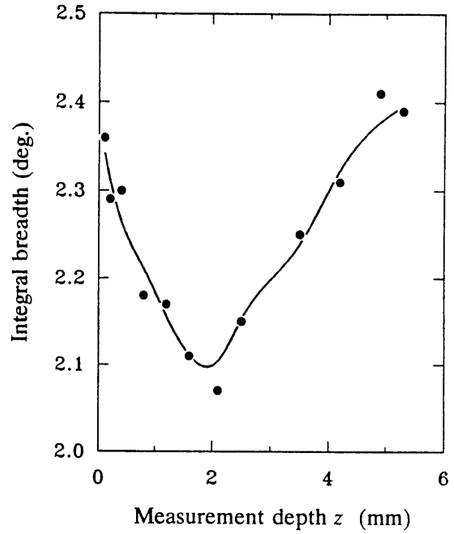

Fig. 6.9 The integral breadth of the x-ray diffraction peaks at $\psi = 0°$, obtained on a rolled U.L.C. cold rolled strip as a function of the depth below the surface. The solid curve serves as a guide to the eye.

removal of material by electrochemical polishing, the stress measurements were performed in two mutually perpendicular directions. On the surface at each stage in this way, the stresses σ_l and σ_t and the stress free lattice parameter d_0 as a function of depth were obtained. The stress results have been corrected for the relaxation due to the removal of material during electrochemical polishing, according to Moore and Evans [6.7].

6.5.5 Results

The data reduction methods for the diffraction results are similar to the ones described during the treatment of the quenched cylinders.

In figure 6.7 the results for the longitudinal stress σ_l and the transverse stress σ_t as a function of the depth of measurement are given. In figure 6.8, the x-ray and neutron results for the stress free lattice distance, which are based on an assumption of a bi-axial stress state are given ($\sigma_z = 0$). In figure 6.9 the integral breadths of the x-ray diffraction peaks at $\psi = 0°$ in the transverse measurements are given.

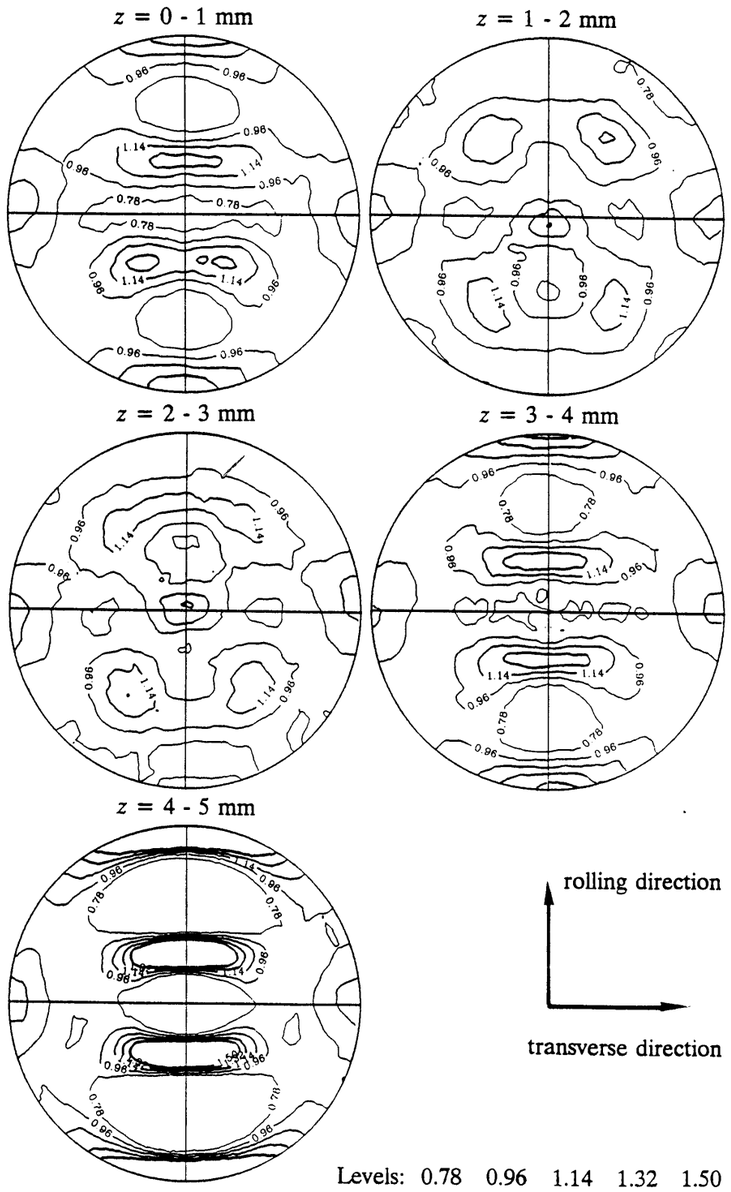

Fig. 6.10 (110)-Pole figures of the samples taken from the cold rolled U.L.C. strip at different depths below the surface (*cf.* figure 6.11).

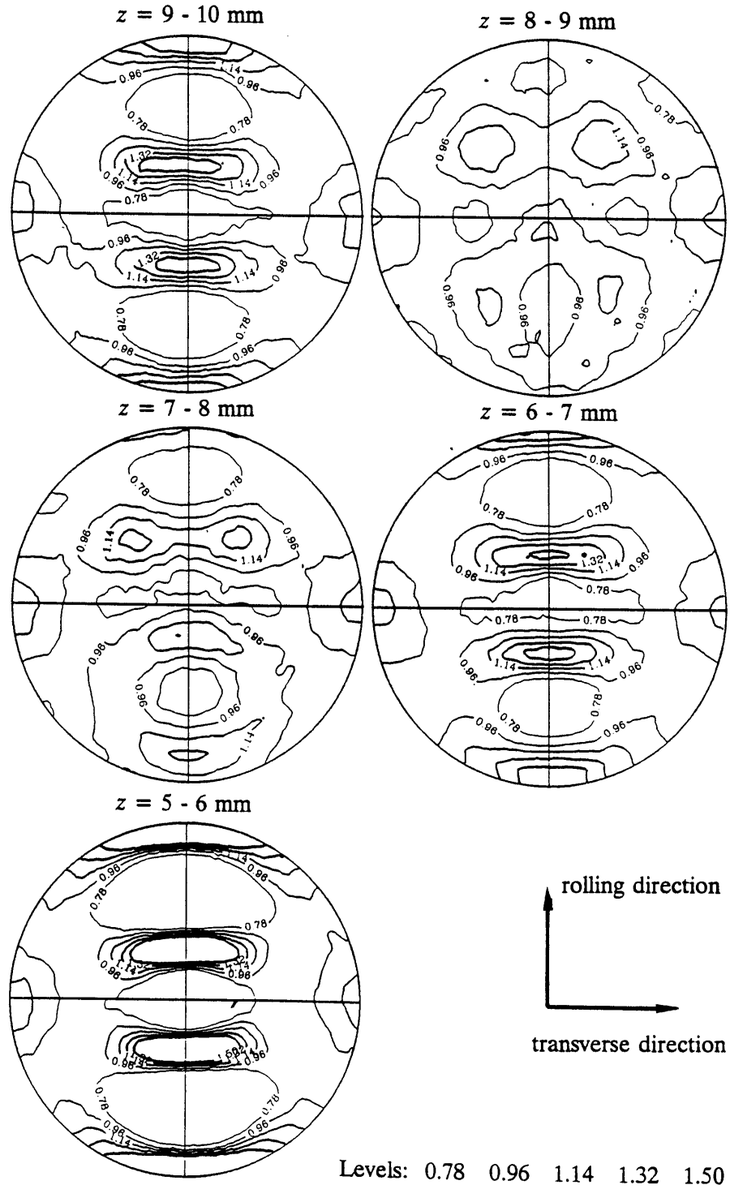

Fig. 6.11 (110)-pole figures of the samples taken from the cold rolled U.L.C. plate at different depth below the surface (*cf.* figure 6.10).

The results of the texture measurements are given in figure 6.10 and 6.11 in the form of ten (110)-pole diagrams each representing the texture at a specific depth interval. The figures indicate intensity contour lines, which represent different levels of diffracted intensity (or in other words the sharpness of the texture)

6.5.6 Discussion

From figure 6.8 it is clear that the obtained value of the stress free lattice parameter d_0 does not change significantly with the depth. For the x-ray measurement this can be expected because of the surface measurement character of this method. With the neutron measurements d_0 as obtained from an analysis of the measurement results on the basis of a bi-axial stress state, does not change with depth. This supports the correctness of the assumption that the stress state in the rolled plate is indeed bi-axial.

In order to be able to compare the d_0-values as obtained by x-rays and neutrons, the x-ray values in figure 6.8, which have been obtained from the (211) reflection of iron have been recalculated to the (110)-values. The difference between the mean d_0-value of both methods must be attributed to the use of different instruments for both methods and a possible zero error with the x-ray system. For stress measurements, the systematic error of the diffraction peak is of little importance as long as it is consistent for all the peaks involved in a stress measurement.

The stress measurement results presented in figure 6.7 show a reasonable agreement between the x-ray and neutron measurements. The results, however, suggest that perhaps some disturbance with the positioning of the sample in the neutron beam geometry might have occurred. When the neutron results curve is shifted by an amount corresponding to 1 mm, the neutron and x-ray result curves would almost coincide. According to all the checks made, a misplacement could not have been the case, however, it can not be totally excluded as it might have happened during operation.

A second reason for differences between the two techniques can be due to the attenuation effect that plays a role in the neutron method. As can be seen from the figures 6.10 and 6.11, the material possesses a depth dependent texture which is almost symmetrical with respect to the sample plane at 5 mm depth. Because of this texture, the attenuation coefficient, that has to be used for the correction method described in

Chapter 2 depends on the orientation of the neutron beam in the sample axis system and on the location of the sample volume. Consequently, it becomes uncertain what value for the attenuation coefficient should be used, in order to obtain an adequate correction on the 8 different peaks that were scanned in a bi-axial stress measurement.

As was mentioned earlier in this section, the presence of texture influences the determination of stress values from measured strain data, because the theory of elasticity involved in this is still not adequately solved. At this stage of the development of the neutron stress measurement technique, however, there are several problems to be solved which are related to the accurate determination of the lattice spacing itself. These problems should be solved before the elasticity related texture problem can be tackled.

In figure 6.7, besides measurements of the stress state, finite element simulations based on the same rolling process are presented. For the case of σ_l there is a reasonable agreement for the bulk region, whereas in the case of σ_t there is no agreement at all. The finite element program called DIEKA that was used in these simulations has been developed for modelling the cold rolling of thin sheet. When thin sheet is rolled, the material transport in transverse direction is very limited due to a larger friction in the direction of the roll axes. In the present case, there has been about 10% net plastic strain in the transverse direction. This has not been accounted for in the simulations which must be the reason for the observed discrepancies between measurement and simulation for σ_t. The agreement for σ_l is good except for the near surface region where some discrepancies between measurement and calculations exist. There may be three reasons for this.

1. The finite element mesh used for the calculations consists of only 5 elements representing the depth direction. This can not provide sufficient resolution for the very near surface region.
2. The residual stress state at the surface depends on the friction that exists between the rolls and the material during rolling. Therefore it depends strongly on the way this friction behaviour is modeled.
3. Dynamic recovery and recrystallisation have taken place and the finite element calculations have not taken that into account.

When we compare the stress situation across the plate thickness (figure 6.7) and the corresponding profile-breadth changes (figure 6.9), obtained with x-rays, we notice that up to a depth of about 2 mm from the surface the residual stresses (both σ_l and σ_t) increase and then start decreasing in magnitude. On the other hand, the profile-breadth variations show an opposite trend. The fact that these trends show a maximum and a minimum for stress and profile-breadth respectively, at a depth of 2 mm suggest that both variables are related to each other and the causes for the changes can be the same.

If we assume the plastic deformation to be uniform and ignore a possible dynamic recovery and recrystallisation for the time being, then the profile breadth should be nearly constant over the cross section. On the other hand, if we assume the deformation to be the highest at the plate surfaces, and decreasing with depth, the breadth variations would show a minimum at the centre. The results of figure 6.9 do not support either of these assumptions. The presence of a minimum indicates a sharpening of the diffraction profile, which can only happen if there was dynamic recovery and/or recrystallisation resulting in a reduction in microstrain and/or an increase in domain size. As mentioned before, the extent of the recovery and recrystallisation will directly depend on the amount of deformation and the temperature raise. Since the breadth of a diffraction profile is sensitive to microstructural changes (and not influenced by macrostresses), from the results of figure 6.9, we may thus conclude that the deformation and the temperature give the highest effect with regard to dynamic recovery and recrystallisation at a depth of about 2 mm from the surface.

The texture results of figures 6.10 and 6.11 strongly support the occurrence of localized recrystallisation in the rolled plate. In the region around 2 mm below the surface (*i.e.* where the integral breadth from figure 6.9 reaches a minimum), the texture is completely different from the texture at both the surface and the centre of the plate. Texture changes on this scale can not be due to dynamic recovery only, but must be the result of partial or total recrystallisation. The fact that the macrostresses (*i.e.* both longitudinal and transversal, see figure 6.7) reach a maximum value at 2 mm below the surface can be well understood if recrystallisation has indeed taken place. Due to the recrystallisation, the density of the material decreases, so during the recrystallisation the material likes to shrink. However, the material that has recrystallised is

under a constraint of both the central part and the surface of the plate, which have not recrystallised because of the local dislocation density and temperature respectively as was discussed above. The result of these constraints is the formation of tensile stresses in the recrystallised material in both the longitudinal and the transverse directions. This might eventually explain the differences between measurements and finite element calculations.

REFERENCES

6.1 T. Fett; K. Keller and O. Munz, *J. Mater. Sci.*, **23**, 467 (1988).

6.2 P.W. Bach; L.A. Correia, The effect of the microstructure on the creep properties of dense alumina, *11th Risø Int. Symposium on Metallurgy and Materials Science*, September 1990.

6.3 H. Huétink, *On the simulation of thermo-mechanical forming processes*, PhD-thesis, Twente University (1986).

6.4 H. Geijselaers, *private communications*

6.5 J. van der Lugt, *private communications.*

6.6 L. Pintschovius; B. Scholtes and R. Schröder, *Proceedings of the 5th Risø International Symposium on Metallurgy and Materials Science.*, Risø Natl. Lab., Roskilde, Denmark, 419 (1984).

6.7 M.G. Moore and W.P. Evans, *SAE Trans.*, **66**, 340 (1958).

6.8 L. Pintschovius, V. Hauk and W.K. Krug, *Mater. Sci. Eng.*, **92**, 1 (1987).

6.9 K. Feja; V. Hauk; W.K. Krug and L. Pintschovius, *Mater. Sci. Eng.*, **92**, 13 (1987).

6.10 C.M. Brakman, *On the interpretation of diffraction line-shift measurements on textured cubic materials*, PhD-thesis, Delft (1988).

6.11 K. Wierzbanowski, *Some results of theoretical study of plastic deformation and texture formation in polycrystals*, PhD-thesis, Kraków, Poland (1987).

6.12 E.Aernoudt, *Conference proceedings WAI-BISPA joint conference*, Stratford upon Avon, England, sept 26-27 (1988), p 5-35.

6.13 S. Denis, E. Gauthier, S. Sjoftrom and A. Simon, *Acta Met.* **35**, 1621 (1987).

6.14 H.J. Bunge, *Mathematische Methoden der Texturanalyse*, Akademie-Verlag, Berlin, 20ff (1969).

7
Evaluation

7.1 INTRODUCTION

The development of an instrumental technique for stress measurements by means of neutron diffraction was the aim of this work and the subject of discussion in the earlier chapters. Most problems encountered with the developed prototype instrument which is at Petten have been thoroughly treated although not all attempts have led to satisfactory solutions. Also the data treatment has had its fair share of attention. On the basis of what has been accomplished so far, a decision was taken to develop a new instrument which will be completely dedicated for performing stress measurements. The experience gained from the experiments carried out so far has been used in the development of this newly built instrument. In this chapter we will discuss the shortcomings of the prototype diffractometer and the possible improvements. Most of these improvements are incorporated in the new instrument.

7.2 A NEW INSTRUMENT

The prototype instrument that has been described in the previous chapters showed a number of shortcomings. These are described below.

1. The old instrument is a temporarily reconstructed powder diffractometer. As normal powder measurements still have to be performed every now and then, the instrument is not 100% of the time available for stress measurements. Due to this reason, a lot of time is lost in reconstructing the set-up after a series of

powder measurements. As will be clear from the previous chapters, the modification and alignment is a time consuming task (time consumption for reconstruction and realignment is estimated to be about 7 to 10 days). The reactor shut down periods can not be effectively used for this purpose, as most steps in the alignment sequence actually need neutrons.

2. The mechanical parts of the powder diffractometer are not designed for operations with the precision that is required for the alignment of the beam apertures and the sample positioning required for stress measurements. All the time a lot of improvisation is needed to obtain the desired precision. Backlash problems and mechanical instability are the main causes for this.
3. All the translation movements are controlled by software operations. There is no independent hardware to check the positions of the translation movements. If one of the translations is mechanically disturbed, the position of the specimen relative to the sample volume is lost. In the course of the work described here this has occurred several times.
4. The powder diffractometer operates with a fixed wavelength. This means that the diffraction angle for a material to be investigated, cannot be varied. This leads to the situation that there is no possibility to change the wavelength such that the diffraction from the chosen reflection takes place at a scattering angle of 90°, which is the ideal diffraction angle from the umbrella effect problem and spatial resolution points of view. Since no wavelength scan can be performed, the attenuation problem that was discussed in Chapter 2 will remain.
5. The dimensions of a sample used in powder diffraction are much larger than the sample volume required for stress measurements. This means that the beam tubes and the monochromator space used for the powder instrument do not provide as much background shielding as one would desire for stress measurements.

In order to deal with these shortcomings, a completely new set-up has been designed and manufactured. The specific features of this instrument involve

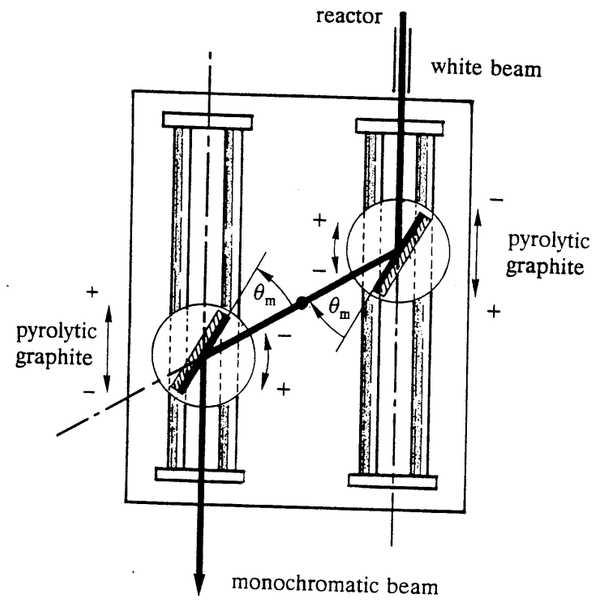

Fig. 7.1 The principle of a double monochromator. The wavelength can be changed by changing the position of both monochromator crystals. During this, the crystals are turned around their axes, vertical to the plane of the drawing, in order to maintain the reflection condition imposed by Bragg's Law.

1. The application of a double monochromator instead of the single monochromator that is currently used in the powder diffractometer. In figure 7.1 an overview of the principle of a double monochromator is given. The advantage of this monochromator is clear. The wavelength of the primary beam is variable within a broad range (*viz.* from 0.15 to 0.65 nm). While scanning in this wavelength range, both the orientation and the position of the primary beam are not changed, meaning that the diffractometer can be fixed to one position. It is important to note that this can never be accomplished by a single monochromator. The material chosen for both reflecting crystals is pyrolytic graphite rather than single crystal copper which is in use in the powder diffractometer monochromator. As such, this new instrument is capable of performing wavelength (λ) scans rather than scattering angle (2φ) scans. This eliminates all the problems that evolve from the attenuation effect. The freedom

of choice on the wavelength, gives the opportunity to choose a scattering angle of 90°, thus eliminating the umbrella effect.

2. As the new instrument is a dedicated one, no time will be lost in rebuilding the set-up and repeating the alignment procedures. For the same reason the shielding of the neutron beam can be tuned to the required primary beam dimensions.
3. The instrument is manufactured with the most modern types of automated machining techniques, thus enabling a better dimensional accuracy than the prototype one. All parts, such as the co-ordinate table and both aperture systems are designed to cope with substantial destabilizing forces before showing any deviation from their stationary positions.
4. The amount of safety circuits has been increased. An automatic switch off of the motors has now been designed such that when a motor is forced to stop at a position where a limit switch has been hit, the measurement computer will remember the position of the interrupted movement. Also a secondary safety circuit has been installed in the form of home switches. Home switches are used to automatically check any drift in the motor positions during the course of the measurements.
5. The maximum permitted load on the specimen table has been increased to 100 kg (it was about 50 kg with the prototype). Even when a full load is applied, the dimensional stability and the tolerances are maintained. In this way, heavier specimens can be investigated.

This section is meant as an evaluation of the steps taken so far, towards the design of what we think will be an ideal instrument to fit our purposes. Regretfully, there are not yet enough results available from this instrument for a preliminary evaluation of its performance.

7.3 POSSIBILITIES AND LIMITATIONS

As was already mentioned in chapter 1 the possibilities for stress measurements by means of neutron diffraction are numerous. Many industrial problems like fatigue, fracture, wear, stress corrosion and welding deformations, can be traced back to residual stresses. Having the

possibility to tackle these problems by means of neutron diffraction stress measurements, may bring about a solution or at least a better understanding of these problems.

Perhaps the most interesting field of research is the verification of finite element calculations, which can be applied on almost every case in which residual stresses play a role. As far as this thesis is concerned, a number of examples of this possibility have already been shown.

While selecting problems to be investigated, one has to realize the intrinsic limitations of the method, which are:

1. A better spatial resolution better than that corresponds to a sample volume of 10 mm^3 is unlikely to be obtained. Therefore, specimens to be investigated should not have very sharp stress gradients in the measurement directions. This limitation is coupled to the time consumption problem. The neutron measurements presented in this research work have taken between 20 and 40 hours of neutron beam time per stress assessment. The time consumption is influenced by the material under investigation and by the precision one likes to obtain for the stress determination.
2. In order to determine tri-axial stress states, the value of the strain free lattice parameter should be known. This causes problems for specimens made of material for which stress free samples are unattainable.

Appendices

APPENDIX 1
THE SINGLE KNIFE EDGE

A1.1 INTRODUCTION

One of the steps in the alignment procedure for the neutron diffractometer in stress measurement mode is the determination of the direction of the primary beam in the co-ordinate system of the specimen table.

A direction is defined by two points. The determination of the position of the centre line of the primary neutron beam, which is one of the two points needed, is the purpose of the single knife edge experiment. Knowing this position, subsequent steps can be taken in order to determine the direction of the beam (*i.e.* the double knife edge experiment, see Appendix 2).

The principle of the single knife edge scan is very simple. The neutron beam that is spread out by primary beam aperture is covered by a neutron absorbing wedge (the single knife). The coverage is removed in a stepwise manner, while between the steps the intensity of the part of the beam that passes the wedge is measured. This process continues until the beam is completely open. Qualitatively, the measured intensity as a function of the wedge position yields a monotonically rising curve with a constant minimum at the beginning and a constant maximum at the end. From this curve we want to obtain the wedge position at which half of the beam is covered.

A1.2 THE SINGLE KNIFE EDGE

The construction of the single knife edge is given in figure A1.1. In this figure also the beam geometry is shown. The single knife edge is built of an aluminium knife holder in which the knife, a cadmium plated brass wedge, is held. The assembly is placed on the specimen table of the diffractometer and rigidly connected to it. The relative position of the

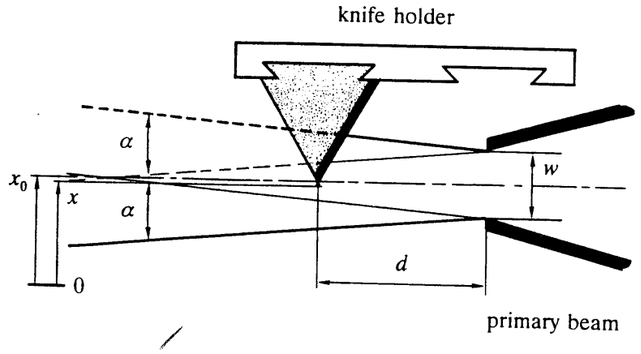

Fig. A1.1 The single knife edge assembly in the primary beam geometry.

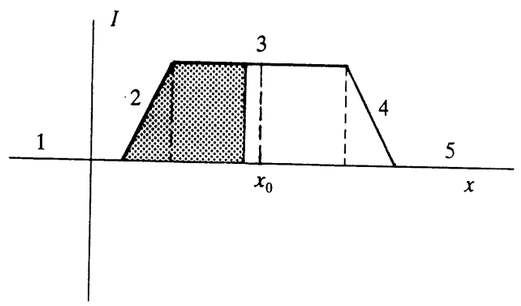

Fig. A1.2 The intensity profile seen at a distance d from the primary beam aperture as a function of the co-ordinate perpendicular to the beam direction. The numbers in the figure refer to the functions derived in the text. The shaded area symbolizes the intensity that is currently 'seen' by the detector (*cf.* figure A1.1).

knife edge perpendicular to the primary beam direction is called x. The position of the centre line of the primary neutron beam is denoted as x_0. The form of the beam cross-section at the site of the single knife edge is characterized by the beam divergence α, the aperture width w and the aperture distance from the knife edge d. The parameter we are looking for is x_0, the knife position at which half of the primary beam is covered.

A1.3 THE SINGLE KNIFE EDGE SCAN FUNCTION

The single knife edge scan consist of intensity measurements as a function of the position x of the knife edge. In order to be able to give an indication of the accuracy of the determination of the beam position x_0, a theoretical model should exist which can be fitted to the single knife edge scan data. A standard fitting procedure, based on the algorithm of Levenberg-Marquardt [A1.1], will yield estimates of the errors in the free parameters of the theoretical model.

The scan starts with the single knife fully covering the primary neutron beam. The neutron detector, situated at the direct beam position, will now only detect background radiation I_b. The detected intensity I as the knife assembly is moved towards the positive x direction (*i.e.* uncovering the beam) can be deduced from the intensity profile shown in figure A1.2. The total measured intensity at some x is equal to:

$$I(x) = \int_{x_0 - \frac{1}{2}w - \frac{1}{2}\alpha d}^{x} dI \qquad \text{(A1.1)}$$

The value of this function is equal to the hatched surface of figure A1.2. It can be represented in a mathematical form when divided in 5 x-regions. The parameter I_0 that appears in the next equations is a proportionality constant.

1. $x < x_0 - \frac{1}{2}w - \frac{1}{2}\alpha d$

$$I = I_b \qquad \text{(A1.2)}$$

2. $x_0 - \frac{1}{2}w - \frac{1}{2}\alpha d \leq x < x_0 - \frac{1}{2}w + \frac{1}{2}\alpha d$

$$I = \frac{(x - x_0 + \tfrac{1}{2}w + \tfrac{1}{2}\alpha d)^2}{2\alpha d} I_0 + I_b \qquad \text{(A1.3)}$$

3. $x_0 - \tfrac{1}{2}w + \tfrac{1}{2}\alpha d \leq x < x_0 + \tfrac{1}{2}w - \tfrac{1}{2}\alpha d$

$$I = (x - x_0 + \tfrac{1}{2}w)I_0 + I_b \qquad \text{(A1.4)}$$

4. $x_0 + \tfrac{1}{2}w - \tfrac{1}{2}\alpha d \leq x < x_0 + \tfrac{1}{2}w + \tfrac{1}{2}\alpha d$

$$I = I_0 - \frac{(x_0 - x + \tfrac{1}{2}w + \tfrac{1}{2}\alpha d)^2}{2\alpha d} I_0 + I_b \qquad \text{(A1.5)}$$

5. $x \geq x_0 + \tfrac{1}{2}w + \tfrac{1}{2}\alpha d$

$$I = I_0 + I_b \qquad \text{(A1.6)}$$

In order to obtain the value of x_0 from the equations A1.2 to A1.6 they have to serve as the model function in a Levenberg-Marquardt fitting procedure. Input to this fitting procedure are a number of intensity measurements as a function of the knife position. As the intensity values have errors based on counting statistics, their square root values are given as the internal errors. The free parameters in the fitting process are: x_0, I_0, I_b, w, and the product αd. In practice, the function has proved very helpfull in establishing correct values for the parameters mentioned. An example of the use of this function is given in Chapter 4.

REFERENCES

A1.1 W.H. Press; B.P. Flannery; S.A. Teukolsky and W.T. Vetterling, *Numerical Recipes*, Cambridge University Press, 509ff (1986).

APPENDIX 2
THE DOUBLE KNIFE EDGE

A2.1 INTRODUCTION

During the alignment procedure for the neutron diffractometer, we want to obtain a physical reference for the primary beam direction. This reference is used for aligning the primary and secondary beam apertures by means of a dial gauge. The single knife experiment, which was treated in Appendix 1, yields a specimen table position at which a cadmium knife is half way closing the primary beam. This position is called x_0 (See Appendix 1). At the stage that x_0 is known, another type of experiment must lead to the determination of the relative direction of the centre line of the beam which will be called ψ_0. The experiment that delivers this parameter is called the double knife edge scan.

The principle of this scan is as simple as the principle of the single knife edge scan. Now, however, two knives instead of one are used and the scan parameter is not a translation perpendicular to the beam direction, but a rotation around the centre of the diffractometer. The stepwise rotation begins at the situation that one knife covers the beam completely and continues until the other knife covers the beam. Between these two extremes, a maximum corresponding to the situation that the two knife edges are in line with the beam exists. The purpose of the single knife edge has thus been reduced to finding out at which knife position, the double knife edge scan should be performed.

As the accuracy in direction of the beam must be estimated, a mathematical treatment of the function that describes the double knife edge scan will be given. Using this function in a parameter adjustment procedure will yield the uncertainties in the determined parameters.

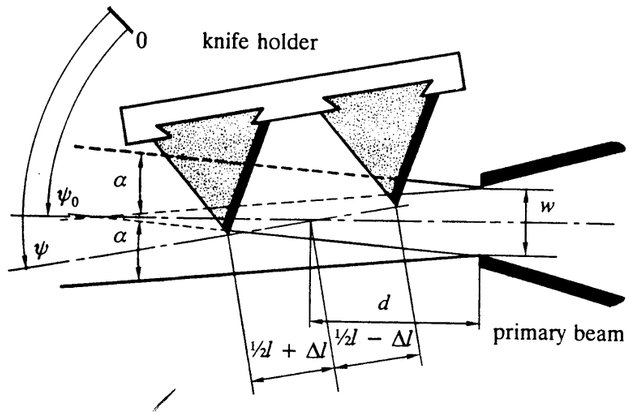

Fig. A2.1 Construction and beam geometry of the double knife edge.

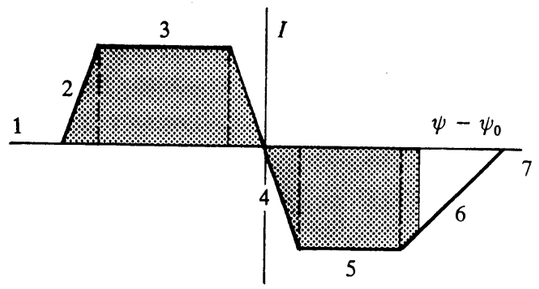

Fig. A2.2 Two profiles of the intensity as a function of the co-ordinate perpendicular to the beam direction which has been transformed into terms of $\psi - \psi_0$. These profiles are active during the double knife edge scan. The intensity that is currently 'seen' by the detector is represented by the shaded area (note that the shaded area in the right side profile has a negative contribution). The numbers in the figure correspond to the functions that are derived in the text (case I).

A2.2 THE DOUBLE KNIFE EDGE

The construction of the double knife edge is given in figure A2.1. In the same figure also the beam geometry is shown. The double knife edge is obtained by putting an extra knife into the empty place of figure A1.1. The advantage of this construction is that the necessity to dismount the knife holder from the specimen table is omitted, thus mechanically conserving the result of the single knife edge scan. The different parts of the assembly are manufactured such that the connection line between the two knives is parallel to the back plane of the knife holder within 0.005°.

Both knife edges should be positioned symmetrically with respect to the centre of rotation of the diffractometer. This is not very critical as there will be a free parameter: Δl in the model that takes care of an unexpected misplacement. In practice, however, the misplacement should not exceed a few millimetres. In order to arrange the knife assembly this way, the co-ordinate table (*i.e.* the y-movement which is along the beam direction) is used to transport the assembly $\frac{1}{2}l$ from the primary beam aperture with respect to the single knife edge scan situation, l being the distance between the knives.

The scan variable of the double knife edge scan is ψ, so the purpose of the scan is to determine the ψ-value at which the line connecting the two knives is parallel to the primary beam centre line. This ψ-value will be called ψ_0.

Usually, there exists a slight misplacement of the double knife edge assembly with respect to the result of the single knife edge scan: x_0. This is due to an incorrect ψ during the single knife edge scan (after all ψ_0 was not yet known during the single knife edge scan). As a result, the fitting procedure on the double knife edge scan, may yield a different value for the aperture opening w than the fitting procedure on the single knife edge scan. When both values for w are too far apart (*e.g.* more than say 10 % of w) it is advisable to repeat the single knife edge scan at the value of ψ that is the result of the then declared 'preliminary' double knife edge scan. In that case, the double knife edge scan must be repeated at the newly determined x_0.

The beam geometry is defined by the same parameters as in the single knife edge scan: α and d and w. Between the scans neither of these should be changed. In practice this means, that the position and opening

of the primary beam aperture must be maintained the same during both scans.

A2.3 THE DOUBLE KNIFE EDGE SCAN FUNCTION

In the following it is assumed that the scan starts at the situation that the knife closest to the aperture defining the primary beam, is covering the beam completely so that only the background radiation I_b is detected by the neutron counter. The direction of ψ is chosen to be counterclockwise.

In figure A2.2 the intensity profile of the beam at the counter side of the double knife edge is given. The ordinate of figure A2.2 is $\psi - \psi_0$, so the integration parameter for the integration of dI will be ψ. In figure A2.2 the detected intensity $I(\psi - \psi_0)$ is seen to be proportional to the hatched surface under the curve. It should be noted that the surface under the right hand part of the curve has a negative contribution. The proportionality constant will be set equal to I_0.

There exist two distinct geometrical modes for the double knife edge scan. The underlying reason is that the beam possesses a finite divergence α. This means that every obstacle that enters the primary beam gives rise to a trapezoid shaped intensity profile behind it. Unfortunately, not only the primary beam aperture can be regarded as an obstacle (two obstacles, to be exact), also the first knife encountered by the beam serves as a moving obstacle that influences the profile to be covered by the second knife as the scan proceeds. Because the knives are rigidly connected by means of the knife holder, the profile encountered by the second knife is influenced by the first one in a predictable way. For the derivation of the intensity function for the double knife edge scan we have to account for this phenomenon. The most important effect of the moving intensity pattern is that depending on the value of the geometrical variables, two different situations exist.

I. $$\tfrac{1}{2}\alpha < \frac{\tfrac{1}{2}w - \tfrac{1}{2}\alpha(d + \tfrac{1}{2}l - \Delta l)}{\tfrac{1}{2}l - \Delta l}$$

This corresponds to the situation that the divergence spread out by the first knife seen from the beam aperture (see figure A2.1) is covered by the second knife before it enters the lower divergence wedge of the

primary beam aperture. The intensity function is now divided into 7 regions:

1. $$\psi - \psi_0 < \frac{-\tfrac{1}{2}w - (d - \tfrac{1}{2}l - \Delta l)\tfrac{1}{2}\alpha}{\tfrac{1}{2}l + \Delta l}$$

$$I = I_b \tag{A2.1}$$

2. $$\frac{-\tfrac{1}{2}w - (d - \tfrac{1}{2}l - \Delta l)\tfrac{1}{2}\alpha}{\tfrac{1}{2}l + \Delta l} \le \psi - \psi_0 < \frac{-\tfrac{1}{2}w + (d - \tfrac{1}{2}l - \Delta l)\tfrac{1}{2}\alpha}{\tfrac{1}{2}l + \Delta l}$$

$$I = \frac{\left\{(\psi - \psi_0)(\tfrac{1}{2}l + \Delta l) + \tfrac{1}{2}w + (d - \tfrac{1}{2}l - \Delta l)\tfrac{1}{2}\alpha\right\}^2}{2(d - \tfrac{1}{2}l - \Delta l)\alpha} I_0 + I_b \tag{A2.2}$$

3. $$\frac{-\tfrac{1}{2}w + (d - \tfrac{1}{2}l - \Delta l)\tfrac{1}{2}\alpha}{\tfrac{1}{2}l + \Delta l} \le \psi - \psi_0 < -\tfrac{1}{2}\alpha$$

$$I = \left\{(\psi - \psi_0)(\tfrac{1}{2}l + \Delta l) + \tfrac{1}{2}w\right\} I_0 + I_b \tag{A2.3}$$

4. $$-\tfrac{1}{2}\alpha \le \psi - \psi_0 < \tfrac{1}{2}\alpha$$

$$I = \left\{\tfrac{1}{2}w + (\psi - \psi_0)(\tfrac{1}{2}l + \Delta l)\right\} I_0 - \frac{l\left\{(\psi - \psi_0) + \tfrac{1}{2}\alpha\right\}^2}{2\alpha} I_0 + I_b \tag{A2.4}$$

5. $$\tfrac{1}{2}\alpha \le \psi - \psi_0 < \frac{\tfrac{1}{2}w - (d + \tfrac{1}{2}l - \Delta l)\tfrac{1}{2}\alpha}{\tfrac{1}{2}l - \Delta l}$$

$$I = \left\{\tfrac{1}{2}w - (\psi - \psi_0)(\tfrac{1}{2}l - \Delta l)\right\} I_0 + I_b \tag{A2.5}$$

6. $$\frac{½w - (d + ½l - \Delta l)½\alpha}{½l - \Delta l} \leq \psi - \psi_0 <$$

$$< \frac{½w + (d + ½l - \Delta l)½\alpha}{½l - \Delta l}$$

$$I = \frac{\left\{½w + (d + ½l - \Delta l)½\alpha - (\psi - \psi_0)(½l - \Delta l)\right\}^2}{2(d + ½l - \Delta l)\alpha} I_0 +$$

$$+ I_b \qquad \text{(A2.6)}$$

7. $$\psi - \psi_0 \geq \frac{½w + (d + ½l - \Delta l)½\alpha}{½l - \Delta l}$$

$$I = I_b \qquad \text{(A2.7)}$$

The second geometrical possibility is the logical complement of the first one so:

II. $$½\alpha \geq \frac{½w - ½\alpha(d + ½l - \Delta l)}{½l - \Delta l}$$

This corresponds to the situation that the divergence spread out by the first knife (see figure A2.1.) is not yet covered by the second knife before it enters the lower divergence spread out by the aperture. The intensity function is again divided into 7 regions.

1. $$\psi - \psi_0 < \frac{-½w - (d - ½l - \Delta l)½\alpha}{½l + \Delta l}$$

$$I = I_b \qquad \text{(A2.8)}$$

2. $$\frac{-½w - (d - ½l - \Delta l)½\alpha}{½l + \Delta l} \leq \psi - \psi_0 <$$

$$< \frac{-½w + (d - ½l - \Delta l)½\alpha}{½l + \Delta l}$$

$$I = \frac{\left\{(\psi - \psi_0)(½l + \Delta l) + ½w + (d - ½l - \Delta l)½\alpha\right\}^2}{2(d - ½l - \Delta l)\alpha} I_0 +$$

$$+ I_b \qquad \text{(A2.9)}$$

3. $$\frac{-½w + (d - ½l - \Delta l)½\alpha}{½l + \Delta l} \leq \psi - \psi_0 < -½\alpha$$

$$I = \left\{(\psi - \psi_0)(½l + \Delta l) + ½w\right\} I_0 + I_b \qquad \text{(A2.10)}$$

4. $$-½\alpha \leq \psi - \psi_0 < \frac{½w - (d + ½l - \Delta l)½\alpha}{½l - \Delta l}$$

$$I = \left\{½w + (\psi - \psi_0)(½l + \Delta l)\right\} I_0 -$$

$$- \frac{l\left\{(\psi - \psi_0) + ½\alpha\right\}^2}{2\alpha} I_0 + I_b \qquad \text{(A2.11)}$$

5. $$\frac{½w - (d + ½l - \Delta l)½\alpha}{½l - \Delta l} \leq \psi - \psi_0 < ½\alpha$$

$$I = \left\{½w + (\psi - \psi_0)(½l + \Delta l)\right\} I_0 - \frac{l\left\{(\psi - \psi_0) + ½\alpha\right\}^2}{2\alpha} I_0 +$$

$$+ \frac{\left\{(\psi - \psi_0)(½l - \Delta l) - ½w + ½\alpha(d + ½l - \Delta l)\right\}^2}{2\alpha(d + ½l - \Delta l)} I_0 +$$

$$+ I_b \qquad \text{(A2.12)}$$

6. $$½\alpha \leq \psi - \psi_0 < \frac{½w + (d + ½l - \Delta l)½\alpha}{½l - \Delta l}$$

$$I = \frac{\left\{½w + (d + ½l - \Delta l)½\alpha - (\psi - \psi_0)(½l - \Delta l)\right\}^2}{2(d + ½l - \Delta l)\alpha} I_0 +$$

$$+ I_b \qquad \text{(A2.13)}$$

7. $$\psi - \psi_0 \geq \frac{½w + (d + ½l - \Delta l)½\alpha}{½l - \Delta l}$$

$$I = I_b \qquad \text{(A2.14)}$$

In order to use one of the set of equations defined above (either A2.1 to A2.7 or A2.8 to A2.14) to obtain ψ_0 from the data of a double knife edge scan, the equations serve as the model in a Levenberg-Marquardt fitting procedure [A2.1]. The free parameters are Δl, w, I_0, I_b, α, and ψ_0. The decision between case I and case II is left to the fitting algorithm in order to avoid a non logical outcome of the calculation. The model has proved to be very successful in calculating the parameters and their error estimates. An example of the use of the model is given in Chapter 4.

REFERENCES

A2.1 W.H. Press; B.P. Flannery; S.A. Teukolsky and W.T. Vetterling, *Numerical Recipes*, Cambridge University Press, 509ff (1986).

APPENDIX 3
ENTERING CURVES

A3.1 INTRODUCTION

After having gone through the sequence of alignment procedures involving the single- and double knife edge scans, the neutron diffractometer including its beam aperture systems can be expected to be well aligned. At this stage two actions have to be taken in order to start a measurement.

1. The quality of the alignment should be checked.
2. The location of the specimen axis system in the beam geometry should be established.

In order to achieve both goals at the same time, the ability of a specimen to diffract neutrons will be used.

The aperture systems that are connected to the diffractometer define a rhombic prism in space: the sample volume. The axis of the prism is expected to coincide with the diffractometer axis. When the specimen is moved towards the diffractometer centre, the specimen material will start to diffract neutrons as the sample volume becomes part of the specimen. The diffracted intensity of a certain peak is a function of the specimen position relative to diffractometer axis and of the parameters that define the shape and the size of the sample volume. Depending on the form and the orientation of the specimen, beam attenuation might play a role.

In the next sections two models – called entering curves – will be presented that give the integrated intensity as a function of the relative specimen position. There will be a treatment of two geometrical situations *i.e.* the diffraction vector $\boldsymbol{q}$ parallel and perpendicular to the specimen surface. The specimen we have chosen for the derivations is a bar shaped specimen that contains no texture. In practice, it is a

rectangular box filled with iron powder. The walls of the box are made of vanadium sheet having a thickness of 0.1 mm.

When the integrated intensity of a diffraction peak is measured as a function of the relative position of the specimen surface for the two orientations of q, the location of the centre of gravity of the sample volume can be found by means of a least squares fitting procedure using both models [A3.1]. The fit results belonging to each of the two models should give the same value for the relative surface position at which the diffractometer axis is situated exactly in the specimen surface. Comparing these results is a way to check the quality of the alignment quality achieved by the procedures that were treated in Chapter 4.

A3.2 ENTERING CURVE AT $\psi = 0°$

The primary and secondary beam apertures, both of width w define a rhombic prism in space. The rhombus is defined by w and 2θ (see figure A3.1). In the well aligned situation, the point of intersection of both diagonals of the rhombus coincides with the centre of rotation of the diffractometer. The to be derived function will be such that at x_0, the intersection the diagonals of the rhombus lies in the specimen surface.

From the thus defined region, a diffracted intensity I is expected which differs from the background value, when some part of the region contains specimen material. The measured integrated intensity from a partly occupied region (to be characterized by x) can be calculated by integrating over the occupied part of the surface region. One aspect of the $\psi = 0°$ case is that the intensity, obtained from a co-ordinate somewhere below the specimen surface, is attenuated due to absorption along the total travelling path for a neutron to and from that particular coordinate. This depth dependent attenuation, is described by an absorption factor, which includes the absorption coefficient μ.

In the left part of figure A3.1 the cross-section of the stationary rhombic prism is shown together with the moving specimen. The function that describes the integrated intensity as a function of the relative specimen position is divided into 4 x-regions. In the next equations I_0 is a proportionality constant, I_b is the background intensity and p_0 is half the rhombus diagonal which is oriented perpendicular to the specimen. It can be shown that

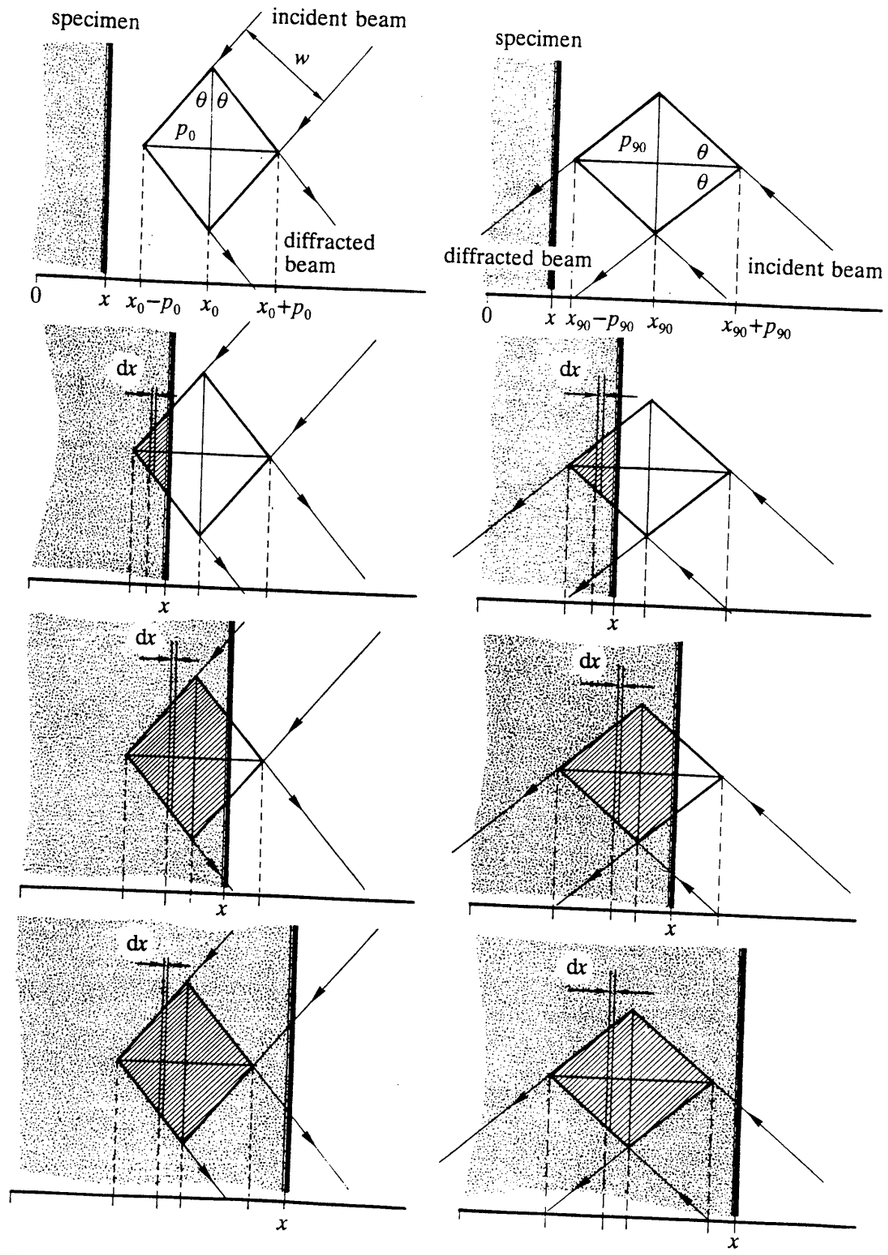

Fig. A3.1 The beam geometry during four distinct states of the entering curve scan at $\psi = 0°$ (left sequence) and at $\psi = 90°$ (right sequence).

$$p_0 = \frac{\sin\theta}{\sin 2\theta} w \tag{A3.1}$$

Using the now defined parameters, the model that gives the integrated intensity as a function of the relative position x will be:

1. $x < x_0 - p_0$

$$I = I_b \tag{A3.2}$$

2. $x_0 - p_0 \leq x < x_0$

$$I = I_0 \frac{x - x_0 + p_0}{\mu} - I_0 \frac{\sin\theta}{2\mu^2} \left\{ 1 - e^{\frac{-2\mu}{\sin\theta}(x - x_0 + p_0)} \right\} +$$

$$+ I_b \tag{A3.3}$$

3. $x_0 \leq x < x_0 + p_0$

$$I = I_0 \frac{\sin\theta}{2\mu^2} \left\{ e^{\frac{-2\mu}{\sin\theta}(x - x_0 + p_0)} - 2e^{\frac{-2\mu}{\sin\theta}(x - x_0)} + 1 \right\} +$$

$$+ I_0 \frac{x_0 + p_0 - x}{\mu} + I_b \tag{A3.4}$$

4. $x \geq x_0 + p_0$

$$I = I_0 \frac{\sin\theta}{2\mu^2} \left\{ e^{\frac{-2\mu}{\sin\theta}(x - x_0 + p_0)} - 2e^{\frac{-2\mu}{\sin\theta}(x - x_0)} + e^{\frac{-2\mu}{\sin\theta}(x - x_0 - p_0)} \right\} +$$

$$+ I_b \tag{A3.5}$$

Equations A3.2 to A3.5 give the expected integrated intensity as a function of x and a number of parameters. From the measurement of I at a series of x-values, the values of the unknown parameters can be

obtained by a Levenberg-Marquardt process. The free parameters that will enter this process *via* the function defined above are: x_0, w, I_0, I_b and μ.

A3.3 ENTERING CURVE AT $\psi = 90°$

For the situation where $\psi = 90°$, *i.e.* when the diffraction vector $\boldsymbol{q}$ is parallel to the specimen surface, the derivation of the integrated intensity as a function of the relative sample position is less complicated as the $\psi = 0°$ case. In this case, the total traveling path for neutrons in the specimen material (the sum of the path to and the path from a specific coordinate) is not dependent on the position in the specimen. This is due to the bar shaped form of the specimen. Therefore all absorption information will be hidden in the parameter I_0.

The geometry for this case is given in the right part of figure A3.1, where it is clearly visible that the beam leaves the specimen on the opposite side from which it has entered the specimen. The parameter that symbolizes the situation where the intersection point of the two rhombus diagonals meets the specimen surface is called x_{90}. The length of the diagonal that is now perpendicular to the specimen surface is called p_{90}, its value is

$$p_{90} = \frac{\cos\theta}{\cos 2\theta} w \tag{A3.6}$$

The model that gives the integrated intensity as a function of relative specimen position is divided into 4 x-regions:

1. $x < x_{90} - p_{90}$

$$I = I_b \tag{A3.7}$$

2. $x_{90} - p_{90} \leq x < x_{90}$

$$I = I_0 (x - x_{90} + p_{90})^2 + I_b \tag{A3.8}$$

3. $x_{90} \leq x < x_{90} + p_{90}$

$$I = I_0 \left\{2p_{90}^2 - (x_{90} + p_{90} - x)^2\right\} + I_b \qquad \text{(A3.9)}$$

4. $x \geq x_{90} + p_{90}$

$$I = 2I_0 p_{90}^2 + I_b \qquad \text{(A3.10)}$$

Equations A3.7 to A3.10 give the expected integrated intensity as a function of x and a number of parameters. From the measurement of I at a series of x-values, the values of the unknown parameters can be obtained by a Levenberg-Marquardt fitting process. The free parameters that will enter this process via the model defined above are: x_{90}, w, I_0, and I_b.

REFERENCES

A3.1 W.H. Press; B.P. Flannery; S.A. Teukolsky and W.T. Vetterling, *Numerical Recipes*, Cambridge University Press, 509ff (1986).

Summary

The residual stress state of a material is one of the characteristics that determine the mechanical properties of a material. Its origin stems from the manufacturing routes such as shaping, joining, heat treatments *etc.* It can be determined in various ways.

Most measurement techniques are limited to the surface of materials, however, also the residual stress state in the interior of materials is of importance for the behaviour of the material.

In this thesis the method of neutron diffraction, with which it is possible to measure the residual stress state in the interior of crystalline materials, is studied. This method is based on the precise determination of the distance between crystallographic lattice planes. In this work, besides the presentation of the necessary mathematical tools, an overview is given of the required experimental set-up. The solution of alignment problems and the use of the set-up for actual measurements comprise an important part of the work described.

The results obtained by means of neutron diffraction are compared to those obtained by using two other stress determination methods. In the first place this is the well established experimental technique of x-ray diffraction and secondly a theoretical technique, based on finite element calculations.

The presented measurements have been limited mainly to ultra low carbon steel. However, by measurements on a ceramic material it was shown that the technique can be used on any crystalline material.

As far as the steel type specimens are concerned, measurements have been carried out on several quenched cylinders and on a cold rolled plate. Both types of samples possess residual stresses that are characteristic for their production processes.

Based on the results, an evaluation is made about the requirements for instrumentation, that performs stress measurements by means of neutron diffraction with an optimum result in the shortest possible measurement time.